Transition radiation in an inhomogeneous and non-linear one-dimensional system

M.Sc. - Thesis

Delft, 2017

Andrei B. Faragau

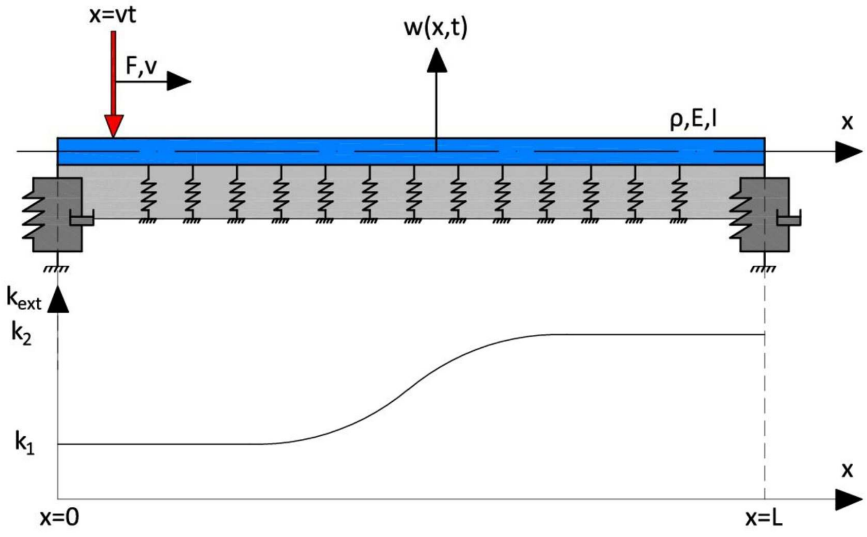

Transition radiation in an inhomogeneous and non-linear one-dimensional system

M.Sc. - Thesis

Delft, 2017

Graduation candidate:

Andrei B. Faragau (4519116) — Steel and Timber Structures

Graduation committee:

Prof. Dr. AV Metrikine (chairman) — Head of Offshore Engineering

Chair Dynamics of Solids and Structures

Dr. ir. K.N. van Dalen (daily supervisor) — Structural Mechanics

Drs. Wybo Gardien — Movares

Dr. Marko Pavlovic — Steel and Timber Structures

Contents

Abstract

When a source moves along a straight line with constant velocity and acts on an inhomogeneous medium, energy is radiated away from the source. This phenomenon is referred to as transition radiation. The energy radiation can also be generated by the change of velocity or path of the source (radiation in a non-uniform motion), as well as when it moves faster than waves can propagate through the medium (Vavilov-Cherenkov or Mach radiation).

Transition radiation is of high importance for both use railways and high-speed railways because the velocity of the trains may approach the wave velocity of the soil in the substructure. This leads to an amplified radiation of waves which cause plastic deformation in the railway track in the vicinity of the transition zone.

In the first part of this thesis, the solution for the system composed of an infinite beam resting on inhomogeneous Winkler foundation with a smooth transition in stiffness and subjected to a constant moving load is obtained. The proposed solution is computed for a finite system incorporating a set of non-reflective boundaries such that it mimics the behaviour of the infinite system. The response is obtained using a combination of a transform method (i.e. the Laplace transform) and a numerical method (i.e. the Finite Difference Method). With the obtained solution, the transition radiation and the influence of the length of the transition zone on it are analysed.

The response obtained for the system with smooth transition in stiffness exhibits a change in magnitude when compared to the response obtained for an abrupt transition. Increasing the length of the transition zone causes a decrease in the magnitude of the excited free waves at the transition. For a very long transition zone, the overall behaviour of the response changes, leading to a significantly shorter radiated pulse, implying that the excited free waves are more localized in space. In addition to the change in magnitude, also a phase shift is observed between the two responses.

In the second part of this thesis, the solution for the system composed of an infinite beam resting on inhomogeneous and non-linear Winkler foundation, and subjected to a constant moving load is obtained. The Winkler-stiffness behaviour is assumed to be piecewise linear, and consequently, the system behaves linearly between non-linear events. This enables the solution to be obtained using a mixed time-frequency approach combined with the Finite Difference Method for the spatial discretization. The computed response incorporates the non-reflective boundaries and the smooth transition in stiffness, obtained in the first part of the thesis. The solution is used to determine the possibility of plastic deformation introduced by the transition radiation, and the parameters influencing it.

The plastic deformation exhibited in the transition zone is observed to be a consequence of a constructive interference of the excited free waves and the approaching eigenfield. The influence of two parameters on the resulting plastic deformation is analysed, namely the length of the transition zone and the velocity of the load relative to the wave velocity in the system. Increasing the length of the transition zone reduces the magnitude of the excited free waves, therefore leads to a less pronounced constructive interference between the excited free waves and the eigenfield, and thus to a decrease in magnitude of the plastic deformations. Surprisingly, in the case of the load velocity close to the wave velocity in the system, enlarging the length of the transition zone does not lead to significant reduction in the plastic deformation exhibited.

The solution method presented in this thesis includes inhomogeneous foundation with a non-linear behaviour and the infinite extent of the model is correctly accounted for. Therefore, it could be used for the initial design of transition zones. Given the stiffness jump that has to be bridged between the two domains, the optimum length of the transition zone can be obtained such that minimum damage results in the railway track.

1. Introduction

In this chapter we first establish the background of the thesis project, namely the dynamics of transition zones in railway tracks, both in general terms and in the more specific situation with which this thesis is concerned. Next, the problem statement and the research motivation are emphasized. Afterwards, the solution to the problem statement is proposed and the main goal is divided into smaller and clearer objectives. Finally, an outline of the thesis is presented to serve the reader as a roadmap.

1.1. Background

When a source moves along a straight line with constant velocity and acts on an inhomogeneous medium, energy is radiated away from the source. This phenomenon is referred to as transition radiation and has been demonstrated theoretically as early as 1945 by Vitaly Ginsburg and Ilya Frank, in electromagnetics. The transition radiation phenomenon is universal from the physical point of view, thus it is encountered in many fields of science, such as electromagnetics, acoustics, mechanics, etc. The energy radiation can also be generated by the change of velocity or path of the source, but in those cases the phenomenon is referred to as radiation in a non-uniform motion.

Trains crossing an inhomogeneity in the track generate elastic waves in the supporting structure, representing transition radiation. The inhomogeneities either come from the track's configuration such as the discrete sleepers, a railroad switch, joints in the rail, etc., or from the subsoil such as non-uniform soil properties, settlements, bridge supports.

One specific case is when trains pass from low stiffness media, such as the soil, to relatively high stiffness elements, such as a bridge. In this case, the inhomogeneity results from the change in stiffness of the supporting structure. Nowadays, this situation becomes increasingly relevant. With the global demand of clean energy use, rail transport has the potential of becoming the main means of transport in the future, due to its capability of running on electricity. But, in order to compete with the airplane, trains must run faster. Consequently, the velocity of the trains already approaches the wave velocity in softer types of soil. This leads to an amplification of the transition radiation which in turn leads to higher and more rapid degradation of the track in the vicinity of the transition.

In some situations, the high-speed trains exceed the wave velocity in the soil of the substructure, in which case the uniform motion generates wave radiation without the need of inhomogeneities. This phenomenon is referred to as Vavilov-Cherenkov effect in electromagnetics, or radiation of Mach waves in acoustics. In this case, wave radiation behind the load is observed and no displacement field in front of the load, because waves in the subsoil do not travel as fast as the load does. The phenomenon can be visualized as a boat moving on the water surface. When the velocity of the boat is greater than the velocity of the free surface gravity waves, there are no waves in front of the boat while there is a significant displacement field behind the boat. Consequently, great efforts and investments are put into improving the subsoil to prevent this effect from occurring. This is one of the reasons why most of the high-speed railways are completely built on concrete slabs, e.g. HSL Zuid in the Netherlands.

1.2. Problem statement

Transition radiation is of high importance for both normal railways and high-speed railways because the velocity of the trains may approach the wave velocity of the soils in the substructure. This leads to an amplified radiation of waves which cause plastic deformation in the railway track in the vicinity of the transition. Typically for delta areas, such as the Netherlands, it is observed that the maintenance frequency of these zones is 4-8 times higher than for regular parts of the track. Moreover, sometimes due to the degradation, speed limits are imposed which can prove costly in terms of time and delays.

Although, the transition radiation in a one-dimensional elastic system has been thoroughly described by Wolfert [1] and the two-dimensional elastic half-space by Van Dalen [2,3,4], a one-dimensional infinite system with non-linear foundation that presents transition radiation cannot be found in the literature, to the best of the author's knowledge. Thus, this thesis aims on developing a one-dimensional model which incorporates non-linear soil behaviour. Such a model will allow to study the influence of non-linear subsoil behaviour on the transition radiation problem and different parameters that influence it. Finally, this will lead to clarification of the underlaying mechanisms causing this damage and to more accurate approximations of displacement and stresses which will lead to better designs in the future.

1.3. Scope and objectives

As stated in the previous section, the main goal of this thesis is to develop a one-dimensional model of a beam resting on inhomogeneous and non-linear foundation subjected to a uniformly moving constant load. The purpose of this model is to study and get a better insight into the phenomenon of transition radiation. In order to reach the final goal, it is broken down into intermediate goals. It must be noted that this thesis only tackles the subsonic load velocity regime.

In reality, the transition in stiffness between the soil medium and the bridge structure is not immediate, but has a certain length over which the transition in stiffness develops. This leads to the first objective of this thesis, namely:

1) Develop a model which incorporates a smoothly varying stiffness, in space, of the foundation.

This introduces the need of solving the system using numerical methods, thus having to solve a finite system. To correctly represent reality, the finite system should have exactly the same behaviour as the infinite system, because the railway can be considered infinite for engineering purposes. Consequently, non-reflective boundaries have to applied in the finite system.

Once this model is developed, we can proceed to the second and main objective, namely:

2) Upgrade the previously derived model to incorporate the non-linear, in time, foundation behaviour.

With the aid of the model, the eventual non-linear events caused by the transition radiation will be studied. The non-linearities are expected to come from the constructive interference between the load's quasi-static displacement field and the waves generated in the transition zone.

The derivations presented in this thesis are mainly analytical which help the reader get insight into the qualitative aspects of the phenomena. Of course, where numerical methods are required, the methodology is explained, as well as examples and results.

1.4. Perspective

This thesis is part of a larger project from TU Delft in collaboration with ProRail, Movares, Deltares and Tensar International, namely "Rapid degradation of railway tracks on soft soils explained and mitigated: multi-scale dynamics modelling, a novel approach". This project, as the title implies, aims at both understanding the underlying mechanisms behind transition radiation and at mitigating it. The modelling of this complex behaviour consists of two main components, namely the small-scale modelling and the multi-scale modelling.

The small-scale modelling describes the micro-mechanical phenomena at a granular level, such as sliding of ballast particles or loss of contact. Moreover, this model aims to represent the state-of-art short and long-term constitutive behaviour of the ballast including the deformation-dependent stiffness, compaction and cyclic effects in a lattice model.

The multi-scale modelling focuses on modelling the actual transition zone as embedded in the entire tack, and on modelling feedback effects from vehicle movement, hanging sleepers and differential settlements. One of the challenges in this model is to couple the computational domain to the compound beam/sleeper/ballast systems to its left and right, in such a way that the computational domain exhibits the same behaviour as an infinite system. Moreover, this model will also incorporate the effect of discrete sleepers. The coupled system will then be used in the framework of mixed time-frequency solver, allowing for non-linear behaviour (Hoving & Metrikine [5]). A second part of this multi-scale model is to incorporate feedback effects. As an example of this is the presence of a discrete sleeper unsupported by the ballast layer due to degradation. This will lead to an instantaneous amplification in the dynamic response in the transition zone.

The third component of this project is to validate the models with experimental data containing short-term and long-term responses of a transition zone in the Netherlands following a regular maintenance operation. Moreover, the project aims also at providing effective mitigation measures.

As it can be clearly seen, the problem statement of this thesis project represents a preliminary investigation of a few basic methods and the possibility and advantages or disadvantages of using them further in the project presented above. This must be considered when reading this thesis, which does not necessarily intend to present the best solutions for the one-dimensional system studied; the perspective is their possible applications for the further development of two or three dimensional models.

1.5. Outline

In Chapter 2 the behaviour of an infinite system is studied, namely an infinite beam resting on homogeneous elastic foundation. This is solved using two methods, a graphical one and a transform method. Firstly, the general system that will be studied in this thesis is thoroughly introduced. Next, the steady-state solution is derived using the two mentioned methods. Finally, the infinite system with a sudden jump in stiffness is analysed in the transient regime, resulting into transition radiation.

In Chapter 3 the behaviour of a finite system is studied. Firstly, the issue related to the load entering and exiting the finite domain, thus inducing artificial transient motion, will be addressed. Next, non-reflective boundary conditions are derived such that the finite system exhibits the exact same behaviour as the infinite system. Then, a finite system with smoothly varying inhomogeneous foundation stiffness

is analysed. In order to obtain its solution, numerical methods are used, namely Finite Difference Method. Finally, intermediate results are presented and discussed.

In Chapter 4 the non-linear behaviour of the Winkler foundation is addressed. The non-linear behaviour of the foundation is incorporated in the model and the solution is obtained by using the mixed time-frequency approach. The methodology related to the approach is presented first. Afterwards, the non-reflective boundary conditions are again derived for this specific case. Next, methods of improving the decay of the frequency spectrum at high frequencies are presented in order to effectively use this method. Lastly, graphical results and concluding remarks of the chapter are presented.

The main conclusions of the study in this thesis are presented in Chapter 5.

2. Infinite system

In reality, a railway track has a finite length, but for engineering purposes it can be considered infinite. Systems are considered infinite if the distance between their boundaries is large enough such that they do not affect the behaviour of the system in between. In order to analyse these systems, the analytical mathematics proves its advantages, being able to describe infinite systems and handle infinities in a very elegant way. In this chapter an introduction to the moving load problems for infinite systems is presented. Firstly, the general system considered in this chapter is described. Afterwards, the steady-state solution of the described system is derived. Two methods of deriving the solution are presented, namely the graphical method and the transform method. Both these solutions are derived based on Wolfert [1]. Finally, the transient solution for an infinite system with a sudden jump in stiffness is derived by means of the transform method, based on van Dalen [2]. Here, the transition radiation is observed and discussed for the first time in this thesis.

2.1. General system description

The system to be described can be visualized in Figure 2.1 and it is composed of three main components: the Euler-Bernoulli beam, the Winkler foundation and a constant moving load.

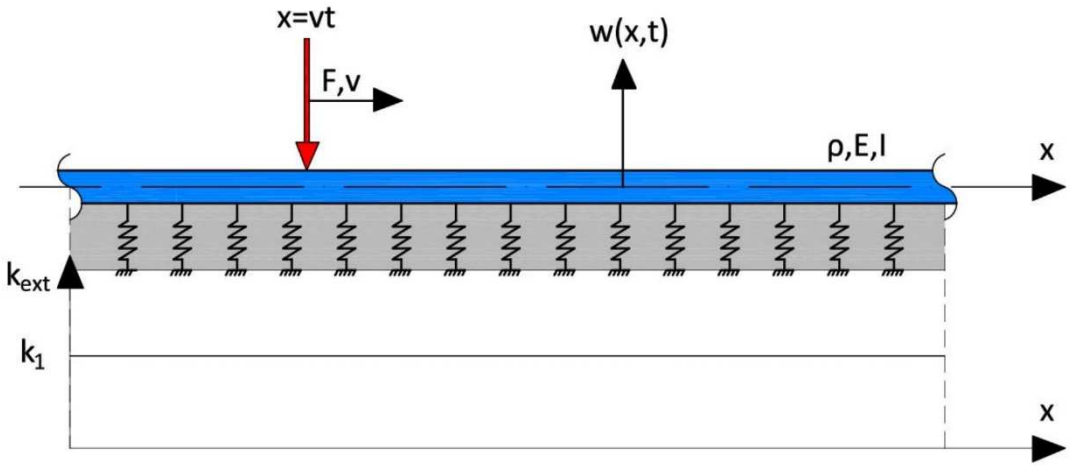

Figure 2.1 - Infinite beam resting on homogeneous Winkler foundation

The Euler-Bernoulli beam is a one-dimensional model describing a beam element. In deriving this model, several assumptions have been made, namely that the shear deformation and the rotational inertia of the beam element are neglected. One important consequence of neglecting the shear deformation is that the displacement throughout the height of the beam is assumed to be constant, therefore the beam can be visualized as a line element without height. The beam model incorporates the behaviour of the rail and the slippers. The extra bending stiffness conferred by the slippers is neglected in this model, but their weight is included in the beam's weight, being distributed along the whole length of the beam.

The second component, the Winkler foundation model consists of infinitely closely-spaced and continuously distributed springs. This one-dimensional foundation model incorporates the behaviour of the layer of ballast and the subsoil. The contact between the foundation and the beam is exactly at the *"x"* axis, as a consequence of using the Euler-Bernoulli beam model.

The thirds main component of the system is the moving load. The load is considered to have a constant velocity and because the system is assumed to be straight, inherently the load has a uniform path. The load is also considered to have constant amplitude and the contact between it and the beam is continuous. Once again, as in the case of the foundation, the contact point is exactly at the *"x"* axis.

The usual framework of solving a general dynamical problem starts with defining an appropriate co-ordinate system and with deriving the equation(s) of motion, which expresses the equilibrium of all the forces present in the system. The next step is to prescribed initial, boundary and, if necessary, interface conditions. Together, these equations compose the governing equations which describe the dynamic behaviour of the specific system considered. Once the governing equations are derived, the problem is mathematically well posed and the solution can be sought for.

The co-ordinate system chosen for most of the problems described in this thesis can be seen in Figure 2.1. It has a stationary reference frame. The *"x"* axis, as discussed previously, is the contact point between all the elements present in the system, the beam, the foundation and the moving load. The positive displacement, $w(x,t)$, is chosen as upwards. In some cases, a different co-ordinate system is advantageous, as seen in the next section, Figure 2.2. This has a moving reference frame compared to the first co-ordinate system. The origin of the moving reference frame is at the position of the load, namely $x = vt$. Both these co-ordinate systems have their advantages. The moving reference frame enables a very elegant derivation of the steady state solution for the infinite system, as it will be seen in the next section. The stationary reference frame enables a better framework of analyzing the transition radiation phenomenon. First, the governing equations are going to be derived for the static frame of reference and afterwards for the moving reference frame.

Once the co-ordinate system is clearly specified, one can proceed in deriving the equation(s) of motion. The equation of motion for the system previously described, considering the static reference frame co-ordinate system, is derived and discussed in Annex A, and reads:

$$\rho \frac{\partial^2 w(x,t)}{\partial t^2} + EI \frac{\partial^4 w(x,t)}{\partial x^4} + k_d w(x,t) = -F_0 \delta\left(x - vt\right)$$

where k_d represents the distributed stiffness of the Winkler foundation, ρ, EI represent the density and the bending stiffness of the E-B beam, respectively, F_0, v represent the amplitude and velocity of the moving load, respectively, and δ is the Dirac-delta function.

For conciseness, the time derivative is replaced by an over dot and the space derivative by a prime. Also, the variables of the functions, x and t are left out from the equations, but will be included for the functions, to show clearly the variables a function depends on. The equation of motion, then, becomes:

$$\rho \ddot{w} + EIw'''' + k_d w = -F_0 \delta\left(x - vt\right)$$

Dividing the whole expression by the bending stiffness, it is rewritten as follows:

$$w'''' + 4\gamma^2 \ddot{w} + 4\beta^4 w = -\frac{F_0}{EI}\delta\left(x - vt\right), \tag{2.1}$$

where $\gamma = \sqrt{\frac{\rho}{4EI}}$ and $\beta = \sqrt[4]{\frac{k_d}{4EI}}$. This last form of the equation of motion is going to be used throughout this thesis.

The initial conditions represent the state of the system at the beginning of computational time, $t = 0$. Three types of initial conditions are going to be used in this thesis. Firstly, for the steady state solution, the initial conditions do not play a role. Secondly, trivial initial conditions, representing the system at rest at $t = 0$, are going to be used in several analyses. Thirdly, initial conditions based on the steady state solution are going to be used, which is going to be described thoroughly in section 2.5.

The interface conditions are not applicable in this case, since the equation of motion describes the entire domain, except for the boundaries at infinity. Thus, the only conditions still left to prescribe are the boundary conditions. For the infinite system, rigorously speaking, boundary conditions cannot be applied since the infinite system does not have boundaries. Instead, certain restrictions to the behaviour of the system at infinity are imposed, namely:

$$\lim_{|x-vt|\to\infty} w\left(x,t\right) < \infty . \tag{2.2}$$

This condition imposes a decaying motion with increasing distance away from the load, thus imposing finite displacements at infinite distance. In the case of damped systems, zero displacements at infinite distances are imposed. Also, when radiating waves are generated, this condition restricts waves propagating backwards from infinity. This condition is called the radiation condition.

With the equation of motion, eq. (2.1), and the boundary condition at infinity, eq. (2.2), the governing equations have been formulated and, mathematically, the problem is properly determined. In the following, the governing equations for the moving reference frame case are derived.

In the moving reference frame case it is advantageous to divide the system into two domains: *domain 1* represents the system behind the load ($x < vt$) and *domain 2* in front of the load ($x > vt$). This can be visualized in Figure 2.2. The equations of motion for the two domains become:

$$\begin{aligned} &w_1'''' + 4\gamma^2 \ddot{w}_1 + 4\beta^4 w_1 = 0, && x < vt, \\ &w_2'''' + 4\gamma^2 \ddot{w}_2 + 4\beta^4 w_2 = 0, && x > vt. \end{aligned} \tag{2.3}$$

To derive the interface conditions, the following variable change is performed:

$$\xi = x - vt .$$

Considering the chain rule in derivation, by applying the above mentioned variable change in the equation of motion, it becomes:

$$w'''' + 4\gamma^2\left(\ddot{w} - 2v\dot{w}' + v^2 w''\right) + 4\beta^4 w = -\frac{F_0}{EI}\delta\left(\xi\right), \tag{2.4}$$

where the prime, now, symbolizes the derivative with respect to the new variable ξ. Considering steady-state behaviour, the two terms containing time derivatives become zero. The equation of motion, thus becomes:

$$w'''' + 4\gamma^2 v^2 w'' + 4\beta^4 w = -\frac{F_0}{EI}\delta(\xi) \ . \tag{2.5}$$

This division leads to the need of imposing interface conditions. The interface conditions represent the continuity in displacements and slope between the two domains as well as the equilibrium of moment and shear force, respectively. They read:

$$\begin{aligned} w_1 &= w_2, && \xi = 0, \\ w_1' &= w_2', && \xi = 0, \\ w_1'' &= w_2'', && \xi = 0, \\ EI\left(w_2''' - w_1'''\right) &= -F_0, && \xi = 0. \end{aligned} \tag{2.6}$$

The last condition in eq. (2.6) is derived by integrating the equation of motion over an infinitesimal spatial domain at $\xi = 0$, as follows:

$$\int_{\xi-0}^{\xi+0} \left[w'''' + 4\gamma^2 v^2 w'' + 4\beta^4 w \right] d\xi = \int_{\xi-0}^{\xi+0} \frac{-F_0}{EI}\delta(\xi) d\xi \ . \tag{2.7}$$

In the left-hand side, the integration of the stiffness foundation term is zero, because only a Dirac load gives a non-zero contribution when integrated over an infinitesimal portion, and we do not expect that the stiffness forces are infinite at any of the positions. Moreover, after integration, the first-order derivative term, representing the slope at the interface, is continuous, therefore gives zero contribution. In the right-hand side, we make use of the Dirac-delta property, which states:

$$\int_{-\infty}^{+\infty} \delta(x) dx = 1,$$

therefore, eq. (2.7) simplifies to the last condition in eq. (2.6).

For the infinite system, the boundary condition at infinity is the same in both co-ordinate systems considered. Therefore, considering the equations of motion, eq. (2.5), the interface conditions, eq. (2.6) and the boundary condition at infinity, eq. (2.2), the governing equation have been formulated also for the moving reference frame.

In the next sections, we proceed to solving the governing equations, therefore, obtaining the solution. Several methods of solving these equations are available and two of them are discussed in this thesis, namely the graphical method and the transform method.

2.2. Steady state solution for the infinite beam on homogeneous elastic foundation – Graphical method

In this section the steady state solution of the system previously described is derived by means of the graphical method. This derivation is performed to make use of the result in section 2.4, where initial conditions employed are based on the steady state solution derived here. Furthermore, the graphical method is also used to get better insight into the moving load problems and how to solve them. Firstly, a solution form is assumed based on the superposition principle. Next, the governing equations are solved, thus obtain the solution for the displacement. Lastly, the solution is presented graphically and discussed.

To solve the system using the graphical method, the moving reference frame is employed, as seen in Figure 2.2. The governing equations for this system have been derived in the previous section. The equations of motion, eq. (2.5), the interface conditions, eq. (2.6) and the boundary condition, eq. (2.2) compose the governing equations. Because the steady state solution is sought for, the initial conditions do not play a role in the derivation.

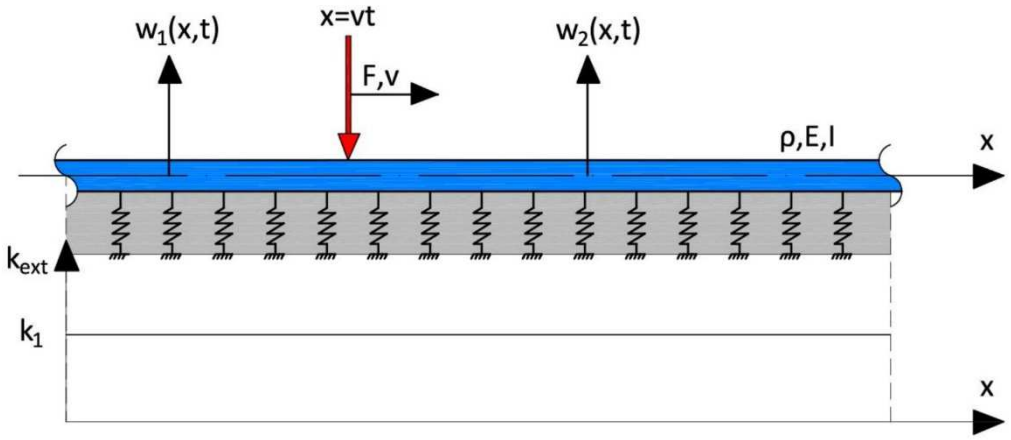

Figure 2.2 - Infinite system with a moving reference frame co-ordinate system

The elements of the system, the beam, the foundation and the moving load are considered to have a linear behaviour. Also, in this section, the Winkler foundation is homogeneous, as seen in Figure 2.2. Due to the linearity of the system and the homogeneity of the foundation, the response can be expressed as a superposition of harmonic waves. Thus, the steady state solutions of the equations of motion, eq. (2.5), are sought for in the form of harmonic waves,

$$w_1(x,t) = \sum A e^{i(\omega t - kx)},$$

$$w_2(x,t) = \sum B e^{i(\omega t - kx)}, \tag{2.8}$$

where A_n, B_n represent the amplitudes of the harmonic waves and ω_n , k_n represent the frequency and wavenumber, respectively, of the harmonic waves. Substituting these assumed form of the solutions, eq. (2.8), in the equations of motion of the system, eq. (2.5), one obtains:

$$\left(k_n{}^4 - 4\gamma^2\omega_n{}^2 + 4\beta^4\right) A_n e^{i(\omega_n t - k_n x)} = 0,$$

$$\left(k_n{}^4 - 4\gamma^2\omega_n{}^2 + 4\beta^4\right) B_n e^{i(\omega_n t - k_n x)} = 0\,. \tag{2.9}$$

The exponent in these equations cannot be zero for all time moments or positions in space, thus cannot satisfy the equation. Because we are not interested in the trivial solution, namely $A_n = B_n = 0$, in order to satisfy the equations, the expression in the parenthesis must be zero, namely:

$$k^4 - 4\gamma^2\omega^2 + 4\beta^4 = 0\,. \tag{2.10}$$

Equation (2.10) is called the dispersion equation for free waves and relates the wavenumber to the frequency and vice-versa. The dispersion equation represents solely the properties of the beam resting on elastic foundation, it does not incorporate the load or the boundary/interface conditions. Because the beam and foundation of the two domains have the same properties, the equation is the same for both domains. Expressing the frequency as a function of the wavenumber from the dispersion equation, eq. (2.10), one obtains:

$$\omega_{1,2} = \pm\sqrt{\frac{k^4}{4\gamma^2} + \frac{\beta^4}{\gamma^2}}\,. \tag{2.11}$$

In order to find expressions for the frequency and wavenumber independently from each other, we must express another equation that relates the two quantities. To this end, another parameter is introduced, the phase of the wave, which is defined as $\phi = \omega t - kx$, the argument of the exponent in eq. (2.8). For the wave to be harmonic, the phase must be constant. Consequently, its derivative with respect to time must be zero.

$$\frac{d\phi}{dt} = \omega - k\frac{dx}{dt} = 0 \tag{2.12}$$

Meanwhile, the load is traveling with the velocity v and it is located at each time moment at $x = vt$. The derivative with respect to time of this expression is $\frac{dx}{dt} = v$, the velocity of the load. Substituting this result in (2.12), one obtains the so called kinematic invariant equation:

$$\omega = kv\,. \tag{2.13}$$

It is important to highlight here that the kinematic invariant relates information about the loading, namely the velocity, to the parameters of the harmonic waves. Figure 2.3 offers a visualization of the two equations, the dispersion equation and the kinematic invariant, to obtain a better understanding of how they relate to each other. Depending on the velocity of the load, one can distinguish three cases. In the first case, the kinematic invariant does not cross the dispersion curves (blue line), in the second case it touches the dispersion curves (red line) and the third case it crosses the dispersion curves (green line), having four intersection points.

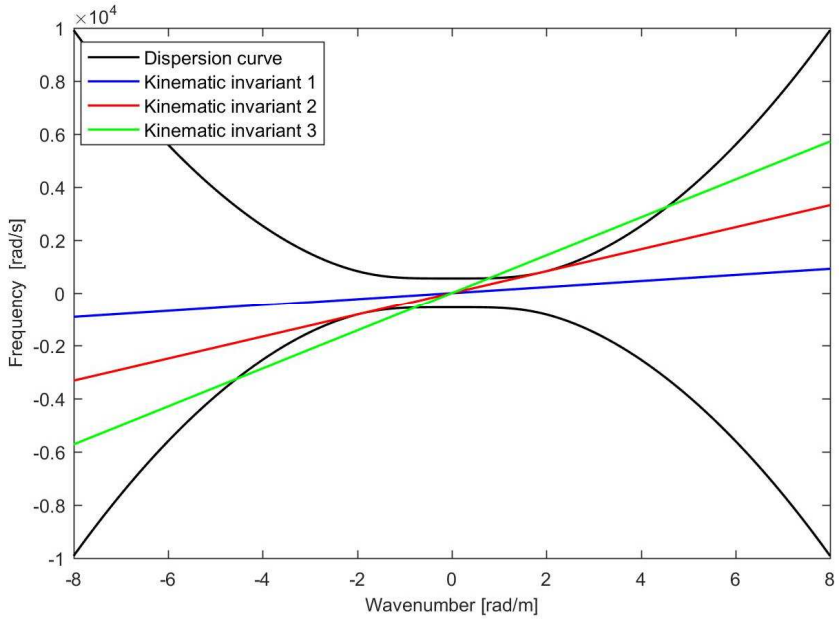

Figure 2.3 – Dispersion curve and the different kinematic invariants for: a) v<c (black line); b) v=c (red line); c) v>c (green line)

The first case represents the subcritical velocity case and it occurs for a load velocity smaller than the minimum phase velocity of the harmonic waves, defined as $c_{ph,\min} = \beta / \gamma$. The third case occurs for the load velocity larger than the minimum phase velocity, while the second case occurs when the two velocities are the same and leads to resonance. For a more extensive description of the three cases (see Wolfert 1999). In this thesis work we are only going to consider the first case, the subcritical velocity.

Solving the system of equations containing the kinematic invariant and the dispersion equation, one obtains the following expressions for the wavenumber.

$$\begin{cases} k_1 = p_1 + ip_2, \\ k_2 = p_1 - ip_2, \\ k_3 = -p_1 + ip_2 = -k_2, \\ k_4 = -p_1 - ip_2 = -k_1, \end{cases} \tag{2.14}$$

where $p_1 = \sqrt{\beta^2 + \gamma^2 v^2}$ and $p_2 = \sqrt{\beta^2 - \gamma^2 v^2}$.

The associated frequencies are:

$$\omega_{1-4} = k_{1-4} v \,. \tag{2.15}$$

Substituting the expressions for the wavenumber and frequency, eq. (2.14) and (2.15), into the general solutions, eq. (2.8), one obtains the following expressions for the displacements of the two domains:

$$w_1(x,t) = A_1 e^{ik_1(x-vt)} + A_2 e^{ik_2(x-vt)} + A_3 e^{-ik_1(x-vt)} + A_4 e^{-ik_2(x-vt)}, \quad x < vt,$$

$$w_2(x,t) = B_1 e^{ik_1(x-vt)} + B_2 e^{ik_2(x-vt)} + B_3 e^{-ik_1(x-vt)} + B_4 e^{-ik_2(x-vt)}, \quad x > vt. \tag{2.16}$$

It must be noted that each of these four terms, in each of the displacement expressions, represent evanescent waves. This fact is due to the wavenumbers being complex numbers. To obey the radiation condition, eq. (2.2), the correct terms for the wavenumbers need to be chosen, such that the real part of the argument in the exponents is negative. This implies that the solution does not become unbounded at infinite distance. To this end, one obtains that $A_1 = A_4 = 0$ and $B_2 = B_3 = 0$, thus eliminating the exponentially increasing waves. Now, the only unknowns remaining are A_2, A_3, B_1, B_4 which are easily found from the interface conditions, eq. (2.6), a system of four algebraic equations with four unknowns. The final displacement field, obtained by combining the two domains into one expression by the use of the absolute value of $x - vt$, reads:

$$w(x,t) = -\frac{iF_0}{2EI}\frac{1}{k_1^2 - k_2^2}\left(\frac{1}{k_1}e^{ik_1|x-vt|} + \frac{1}{k_2}e^{-ik_2|x-vt|}\right). \tag{2.17}$$

Two important things must be noted here. Firstly, the displacement solution, eq. (2.17), seems to be a complex valued function, due to the complex arguments of the exponents, complex wavenumbers and the imaginary number in front of the expression. This is not the case because the imaginary parts are canceling each other out, leading to a purely real valued function. To prove this, we express the exponents with Euler's formula and rearrange the expression, thus obtaining real valued functions, as follows:

$$w_1(x,t) = -\frac{F_0 e^{p_1(x-vt)}}{8p_1\beta^2}\left[\cos\left(p_2(x-vt)\right) - \frac{p_1}{p_2}\sin\left(p_2(x-vt)\right)\right], \quad x < vt,$$

$$w_2(x,t) = -\frac{F_0 e^{-p_1(x-vt)}}{8p_1\beta^2}\left[\cos\left(p_2(x-vt)\right) + \frac{p_1}{p_2}\sin\left(p_2(x-vt)\right)\right], \quad x > vt. \tag{2.18}$$

Secondly, the exponentials in eq. (2.17) represent evanescent waves. This means that there is no wave propagation through the system and that the displacement field is stationary with respect to the load, moving along with the load. This is only the case for the subcritical velocity of the load. This displacement field is going to be addressed throughout the thesis as the eigenfield and is depicted in Figure 2.4.

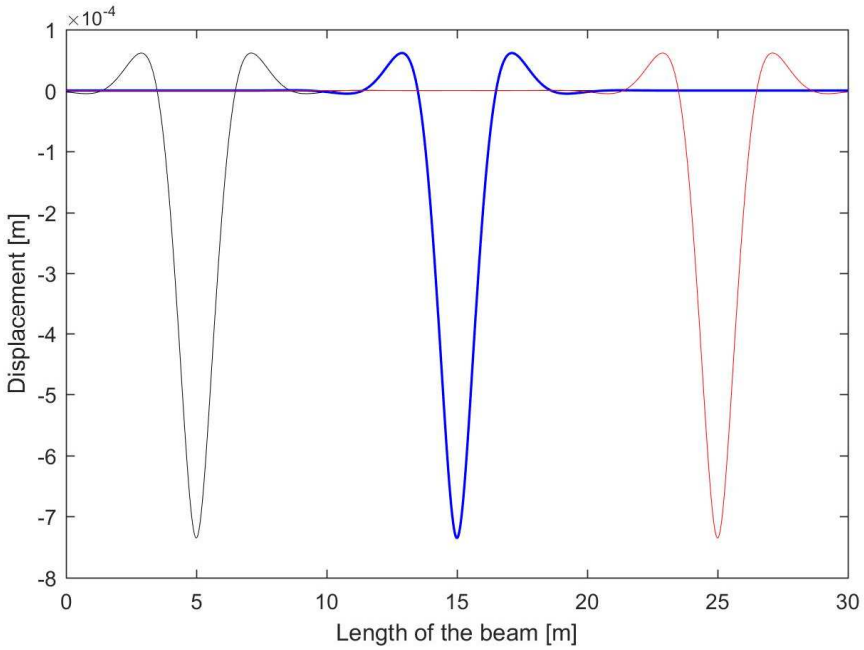

Figure 2.4 – Displacement field of the beam for the subcritical load velocity for different time moments: a) t=0.025 s (black line); b) t=0.075 s (blue line); c) t = 0.125 s (red line)

The displacement field depicted in Figure 2.4 is referred to as the eigenfield. It is stationary and, for the undamped case, symmetric with respect to the load. One important feature of the eigenfield for the beam is that it is continuous even at the position of the load, unlike for other model of a string or rod.

The steady state solution of the infinite beam resting on homogeneous elastic foundation subjected to a constant moving load has been derived by means of the graphical method. The advantage of the graphical method is that each step of the derivation is quite easy to understand and visualize because the whole derivation is performed in the space-time domain. But to observe the transition radiation the transient response of the system is required. To this end, the transform method is going to be used. In the next section, to introduce the concept, the steady state solution is derived by means of the transform method.

2.3. Steady state solution of the homogeneous and linear infinite system – Transform method

In this section another method of solving the previously described system is presented, namely the transform method. This method is introduced due to its ability to represent the transient behaviour of the system, unlike the graphical method. The transient solution of the system is needed in order to study the transition radiation. To this end, firstly the co-ordinate system and the afferent governing equations are chosen. Next, the concept of the method is introduced, and we proceed to solving the governing equations.

For this method, the stationary reference frame is chosen, represented in Figure 2.1. Although the method can be used also for the moving reference frame, keeping in mind that the end goal is to represent transition radiation phenomena, the stationary reference frame is more advantageous. The governing equations for this co-ordinate system is composed of the equation of motion, eq. (2.1), and the radiation condition. Once again, because the steady state solution is sought for, the initial conditions do not play a role in the derivation.

The principle of the transform method is similar to the graphical method, both relying on the superposition of harmonic waves as the form of the solution. The difference is that while the solution in the graphical method superimposes two harmonic waves for each of the domains, in the transform method an infinity of harmonic waves are superimposed. This is done by means of the Fourier transforms.

The Fourier transforms are a set of two transforms, forward and backward, respectively, defined as:

$$\tilde{w}(x,\omega) = \int_{-\infty}^{\infty} w(x,t) e^{-i\omega t} dt \,, \tag{2.19}$$

$$w(x,t) = \frac{1}{2\pi} \int_{-\infty}^{\infty} \tilde{w}(x,\omega) e^{i\omega t} d\omega \,. \tag{2.20}$$

The overhead tilde is meant to distinguish the expression in the Fourier domain from the ones in the time domain. Applying the forward Fourier transform over time to the equation of motion, eq. (2.1), one obtains the following equation:

$$\int_{-\infty}^{\infty} \left[w'''' + 4\gamma^2 \ddot{w} + 4\beta^4 w \right] e^{-i\omega t} dt = -\int_{-\infty}^{\infty} \frac{F_0}{EI} \delta(x - vt) e^{-i\omega t} dt \,. \tag{2.21}$$

In the left-hand side, the beam bending stiffness and the foundation stiffness terms, are straight forwardly transformed into their Fourier images. The integral for the inertia term is performed using integration by parts twice. In the left-hand side, we make use of yet another property of the Dirac delta function, which states:

$$\int_{-\infty}^{+\infty} f(x) \delta(x - a) dx = f(a) \,. \tag{2.22}$$

Therefore, after rearranging, the Fourier image of the time domain equation of motion is:

$$\tilde{w}'''' - k^4 \tilde{w} = -\frac{F_0}{vEI} e^{-i\omega \frac{x}{v}} \,, \tag{2.23}$$

where $k = \sqrt[4]{4\gamma^2\omega^2 - 4\beta^4}$. (2.24)

Looking at the equation (2.23) we observe that from a differential equation with respect to time, by applying forward Fourier transform, the equation became algebraic with respect to time, which is considerably easier to solve. Here is where the power of the transform method lies. One other important thing to mention is that once the integration over time has been performed, the time is no longer a variable in the equation, being replaced by the frequency as the variable.

To solve the fourth order differential equation with respect to space, one could apply once again the forward Fourier transform over space. This approach is used by Wolfert [1]. In this thesis, a different approach is chosen, based on the graphical method. We assume the shape of the solution as a superposition of harmonic waves in space for the homogeneous equation and a particular solution for the inhomogeneous equation. The shape of the solution for the homogeneous equation is once again:

$$\tilde{w}_h(x,\omega) = \sum A e^{irx} . \tag{2.25}$$

where r represents the wavenumber and subscript h denotes the homogeneous solution.

Substituting this solution into the homogeneous equation of motion in the Fourier domain, one straightforwardly finds that the wavenumber is:

$$r_{1-4} = \pm k, \pm ik . \tag{2.26}$$

Thus, the homogeneous solution becomes:

$$\tilde{w}_h(x,\omega) = A_1 e^{-ikx} + A_2 e^{ikx} + A_3 e^{kx} + A_4 e^{-kx} . \tag{2.27}$$

To obey the radiation condition, eq. (2.2), the correct terms for the wavenumbers need to be chosen, such that the solution is bounded at infinite distance. For the solution to be bounded at infinite distance, the real part of the exponents' argument must be negative. Unlike the graphical method where the frequency had a defined value, here, in the Fourier domain, the frequency is a variable, taking values from the whole real number domain. The wavenumber depends on the frequency as seen in eq. (2.24). Studying the expression under the fourth order square root in eq. (2.24), one observes that for $\omega = \pm(\beta^2/\gamma)$ the function has a discontinuity, changing suddenly from positive to negative and vice-versa. These two points are called branch points. The value of the function between these branch points must be formally defined in order to choose the correct terms for the wavenumbers in eq. (2.27). The branches are chosen as:

$$\begin{cases} k = -\sqrt[4]{4\gamma^2\omega^2 - 4\beta^4} , & \omega < -(\beta^2/\gamma), \\ k = \dfrac{1-i}{\sqrt{2}}\sqrt[4]{-4\gamma^2\omega^2 + 4\beta^4} , & |\omega| < (\beta^2/\gamma), \\ k = \sqrt[4]{4\gamma^2\omega^2 - 4\beta^4} , & \omega > (\beta^2/\gamma). \end{cases} \tag{2.28}$$

To obey the radiation condition with this choice of branches, for negative spatial co-ordinate $A_1 = A_4 = 0$ and for positive spatial co-ordinate $A_2 = A_3 = 0$. It must be noted that the choice of the branches is not unique, other choices are possible, which in turn will change the terms chosen from the homogeneous solution. With these considerations, the homogeneous solutions become:

$$\begin{aligned} \tilde{w}_{h,1}(x,\omega) &= A_2 e^{ikx} + A_3 e^{kx}, & x < 0 , \\ \tilde{w}_{h,2}(x,\omega) &= A_1 e^{-ikx} + A_4 e^{-kx}, & x > 0 . \end{aligned} \tag{2.29}$$

The particular solution is sought for assuming the same spatial form as the forcing, namely:

$$\tilde{w}_p(x,\omega) = W_p e^{-i\omega\frac{x}{v}} , \tag{2.30}$$

where W_p represents the yet unknown amplitude and subscript p stands for particular. To find the unknow amplitude, the particular solution is substituted in the inhomogeneous equation of motion, eq. (2.23) leading to an algebraic equation which is straightforwardly solved. The particular solution, then, becomes:

$$\tilde{w}_p(x,\omega) = -\frac{F_0 v^3}{EI}\frac{1}{\omega^4 - k^4 v^4} e^{-i\omega\frac{x}{v}}. \tag{2.31}$$

The solution to the inhomogeneous equation of motion is a superposition of the homogeneous and the particular solutions:

$$\tilde{w}_1(x,\omega) = A_2 e^{ikx} + A_3 e^{kx} - \frac{F_0 v^3}{EI}\frac{1}{\omega^4 - k^4 v^4} e^{-i\omega\frac{x}{v}}, \qquad x < 0,$$

$$\tilde{w}_2(x,\omega) = A_1 e^{-ikx} + A_4 e^{-kx} - \frac{F_0 v^3}{EI}\frac{1}{\omega^4 - k^4 v^4} e^{-i\omega\frac{x}{v}}, \qquad x > 0. \tag{2.32}$$

The solution had to be divided into two domains, depending on the positive and negative spatial co-ordinate. To find the four unknowns, interface condition must be imposed. The first three interface conditions in eq. (2.6), namely the continuity in displacement and slope and the moment equilibrium, are the same. The interface condition denoting the shear force equilibrium changes because the moving reference frame is static in this case. The interface conditions read:

$$\begin{aligned}
&\tilde{w}_1 = \tilde{w}_2, && x = 0,\\
&\tilde{w}_1' = \tilde{w}_2', && x = 0,\\
&\tilde{w}_1'' = \tilde{w}_2'', && x = 0,\\
&\tilde{w}_1''' = \tilde{w}_2''', && x = 0.
\end{aligned} \tag{2.33}$$

Substituting the solutions, eq. (2.32), into the interface conditions and solving the system of four algebraic equations for the four unknowns, one obtains that all four amplitudes are zero. This basically means that there are no free waves in the system, which could be anticipated by looking at the eigenfield derived in the previous section. The solution is the same for both domains and becomes:

$$\tilde{w}(x,\omega) = -\frac{F_0 v^3}{EI}\frac{1}{\omega^4 - k^4 v^4} e^{-i\omega\frac{x}{v}}. \tag{2.34}$$

To obtain the time domain solution, one must apply the backward Fourier transform:

$$w(x,t) = -\frac{F_0 v^3}{EI}\frac{1}{2\pi}\int_{-\infty}^{\infty}\frac{1}{\omega^4 - k^4 v^4} e^{-i\frac{\omega}{v}(x-vt)} d\omega. \tag{2.35}$$

The integral can be computed analytically by means of contour integration. This solution is presented by Wolfert [1] and the result is exactly the same as the one derived with the graphical method, eq. (2.17). In this thesis, for most of the problems studied in the next chapters the contour integration cannot be performed analytically. For this reason, the numerical approximation of the integral is introduced here. In order to evaluate the integral numerically, firstly the frequency domain, over which the

integration is performed, has to be truncated, because infinities cannot be computed numerically. Secondly, the frequency domain must be discretized into definite values. These two steps have to be performed carefully, otherwise computational artifacts are introduced in the solution, leading to large errors. Lastly, a numerical method of approximating the area enclosed by the function must be adopted. Throughout this thesis, the trapezoidal method is used, although there are more precise methods available. The integral is approximated using the following function:

$$\int_a^b f(\omega)d\omega \approx \frac{b-a}{2N}\sum_{n=1}^{N}\left(f(\omega_n)+f(\omega_n+1)\right) \tag{2.36}$$

where a,b represent the truncation limits of the frequency domain and N represents the number of frequency domain elements. Once this is applied for the whole integrand, the displacement in the time domain is found. Further, the numerical results obtained are compared to the analytical solution derived by the graphical method.

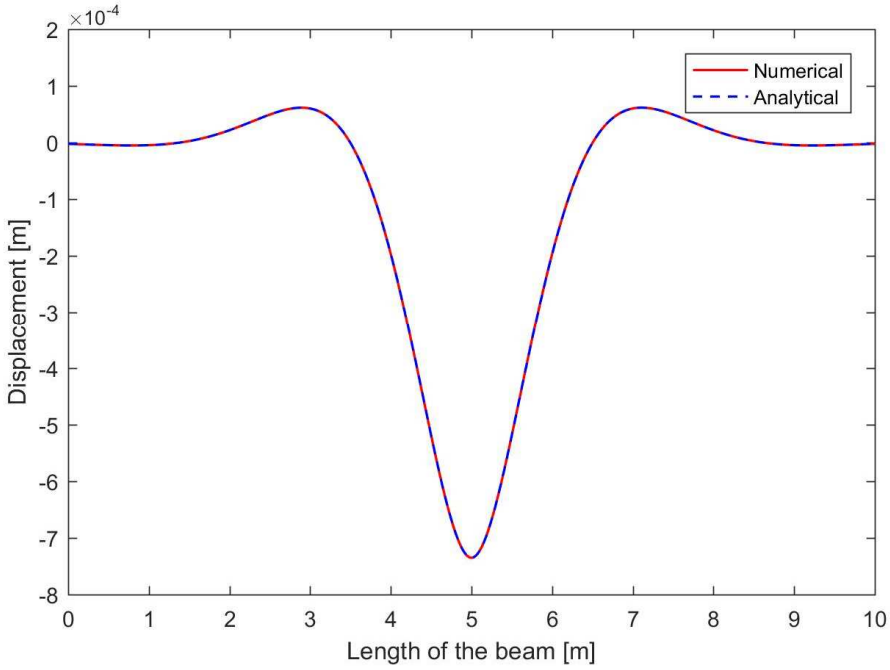

Figure 2.5 – Plot of the numerically obtained eigenfield (red) against the analytical solution (blue)

It can be observed from Figure 2.5 that the two solutions overlap completely, thus validating the numerically obtained solution. This tool, the numerical approximation of the inverse Fourier integral will prove very useful throughout the thesis. Of course, the numerical evaluation of the integral results in numerical data and the lack of a closed form solution can become problematic for a number of situations. One such situation is taking of derivatives of the numerical data which introduces significant error. Nevertheless, a closed form solution does often not exist, therefore numerical approaches prove to be indispensable.

In this section we have derived the steady-state solution to the previously described system by means of Fourier transform method. Although the two methods, graphical method and the transform method, rely on the same principle of superposition of harmonic waves, we shall see that the transform method is also suitable for studying the transient response of a system, thus also suitable for transition radiation problems. In this section, the contour integration has been also introduced, which is a very useful tool

for evaluating integrals, but it cannot always be applied. In the following, the transient response of the infinite system with a sudden transition in stiffness is studied.

2.4. Transition radiation in an inhomogeneous and linear infinite system

In this section the infinite system with a sudden jump in Winkler foundation stiffness is analyzed. The transient solution to the system is derived in a semi-analytical approach. Firstly, the Fourier transform method is applied over time. Next, the spatial form of the solution is assumed under the harmonic wave shape. Afterwards, the solution in the Fourier domain is determined. A numerical approach is used to determine the time domain response. Lastly, the results are shortly discussed. The approach is mainly based on van Dalen [3].

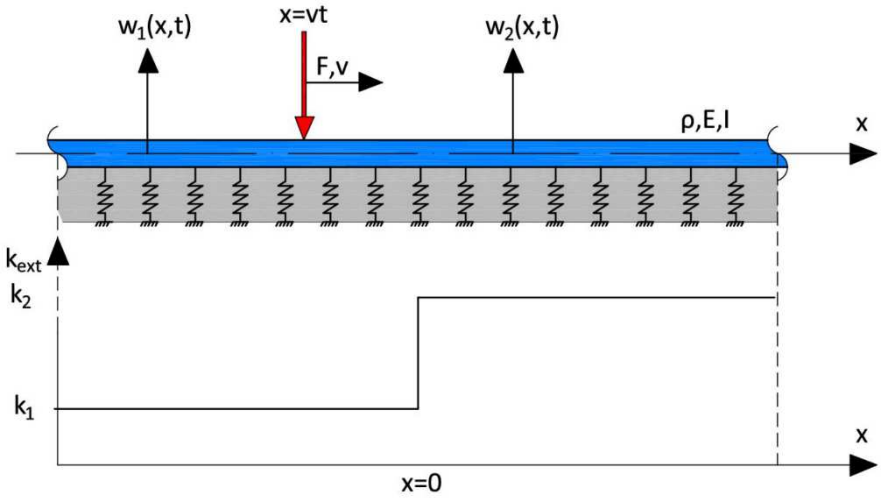

Figure 2.7 – Infinite system with a Heaviside jump in the Winkler foundation stiffness

The system studied in this section can be visualized in Figure 2.7. Due to the change in stiffness of the Winkler foundation, the system is divided in two domains. The first one defined on the negative space coordinate and the second one on the positive space coordinate. The equations of motion, in the time domain, are:

$$w_1''''+4\gamma^2\ddot{w}_1+4\beta_1^4 w_1=-\frac{F_0}{EI}\delta(x-vt), \qquad x<0,$$

$$w_2''''+4\gamma^2\ddot{w}_2+4\beta_2^4 w_2=-\frac{F_0}{EI}\delta(x-vt), \qquad x>0, \qquad (2.37)$$

where $\beta_{1,2}=\sqrt[4]{\frac{k_{d1,2}}{4EI}}$ represents the Winkler foundation stiffness term for the two domains.

Once again, we assume that the load has entered the system at infinite distance left of the origin, such that the initial conditions do not play a role in the solution close to the origin.

The boundary condition is the radiation condition and the interface conditions read:

$$\begin{aligned} w_1 &= w_2, && x = 0, \\ w_1' &= w_2', && x = 0, \\ w_1'' &= w_2'', && x = 0, \\ w_1''' &= w_2''', && x = 0. \end{aligned} \tag{2.38}$$

The governing equations have been stated, so we can proceed to solving them. Firstly, the direct Fourier transform is applied over all the governing equations. The boundary and interface conditions do not change their meaning, but only the quantities are transformed, thus they are not repeated. The equations of motion become:

$$\begin{aligned} \tilde{w}_1'''' - k_1^4 \tilde{w}_1 &= -\frac{F_0}{vEI} e^{-i\omega\frac{x}{v}}, && x < 0, \\ \tilde{w}_2'''' - k_2^4 \tilde{w}_2 &= -\frac{F_0}{vEI} e^{-i\omega\frac{x}{v}}, && x > 0, \end{aligned} \tag{2.39}$$

where $k_{1,2} = \sqrt[4]{4\gamma^2\omega^2 - 4\beta_{1,2}^4}$. (2.40)

Once again, the branches of the radical are chosen as follows:

$$k_{1,2} = \begin{cases} -\sqrt[4]{4\gamma^2\omega^2 - 4\beta_{1,2}^4}, & \omega < -\dfrac{\beta_{1,2}^2}{\gamma} = -\sqrt{\dfrac{k_{d1,2}}{\rho}}, \\ \dfrac{1-i}{\sqrt{2}}\sqrt[4]{-4\gamma^2\omega^2 + 4\beta_{1,2}^4}, & \omega^2 < \dfrac{\beta_{1,2}^4}{\gamma^2} = \dfrac{k_{d1,2}}{\rho}, \\ \sqrt[4]{4\gamma^2\omega^2 - 4\beta_{1,2}^4}, & \omega > \dfrac{\beta_{1,2}^2}{\gamma} = \sqrt{\dfrac{k_{d1,2}}{\rho}}. \end{cases} \tag{2.41}$$

The homogeneous solutions of (2.39), accounting for the radiation condition, are:

$$\begin{aligned} \hat{w}_{h,1}(x,\omega) &= A_2 e^{ik_1 x} + A_3 e^{k_1 x}, \\ \hat{w}_{h,2}(x,\omega) &= A_1 e^{-ik_2 x} + A_4 e^{-k_2 x}. \end{aligned} \tag{2.42}$$

The particular solutions are the same as in the previous section, eq. (2.31), except for the wavenumber expression which has to be substituted according to (2.40). The general solutions are a superposition of the homogeneous ones and particular ones, thus read:

$$\tilde{w}_1(x,\omega) = A_2 e^{ik_1 x} + A_3 e^{k_1 x} - \frac{F_0 v^3}{EI}\frac{1}{\omega^4 - k_1^4 v^4} e^{-i\omega\frac{x}{v}},$$

$$\tilde{w}_2(x,\omega) = A_1 e^{-ik_2 x} + A_4 e^{-k_2 x} - \frac{F_0 v^3}{EI}\frac{1}{\omega^4 - k_2{}^4 v^4} e^{-i\omega\frac{x}{v}}. \tag{2.43}$$

Now, the only unknows are the amplitudes of the free waves in the general solutions. These can be found from the interface conditions. Substituting the solutions into the interface conditions and solving the system of four algebraic equations for the four unknown amplitudes, one obtains:

$$A_1 = -\frac{1}{2}\frac{F_0 v^4}{EIk_2}\frac{(1+i)(k_1-k_2)(-k_1+ik_2)}{(k_1 v-\omega)(k_2 v+i\omega)(-k_1 v+i\omega)(k_2{}^2 v^2-\omega^2)},$$

$$A_2 = -\frac{1}{2}\frac{F_0 v^4}{EIk_1}\frac{(1-i)(k_1-k_2)(k_1+ik_2)}{(i\omega-k_1 v)(k_2 v+\omega)(k_2 v+i\omega)(k_1{}^2 v^2-\omega^2)},$$

$$A_3 = -\frac{1}{2}\frac{F_0 v^4}{EIk_1}\frac{(1+i)(k_1-k_2)(-k_1+ik_2)}{(k_1 v-\omega)(k_2 v+\omega)(k_2 v+i\omega)(k_1{}^2 v^2+\omega^2)},$$

$$A_4 = -\frac{1}{2}\frac{F_0 v^4}{EIk_2}\frac{(1+i)(k_1-k_2)(k_1+ik_2)}{(-k_1 v+i\omega)(k_2 v+\omega)(k_1 v-\omega)(k_2{}^2 v^2+\omega^2)}. \tag{2.44}$$

With the found amplitudes, the whole solution in the Fourier domain is known. The fact that the amplitudes are different from zero basically means that free waves are present in the system as well as the eigenfield derived in the previous section, represented by the particular solution.

The only procedure still needed is to apply the inverse Fourier transform to obtain the solution in the time domain. The exponentials in (2.43) related to the free waves introduce branch points in the complex plane. This makes the application of the contour integral much more cumbersome and impossible to carry out fully analytically. Consequently, the numerical integration is used. The results are presented in Figure 2.8.

The following parameters are used for the plots:

- Winkler stiffness in the soft part: $k_1 = 8.33\times10^7$ N/m^2
- Winkler stiffness in the stiff part: $k_2 = 8.33\times10^8$ N/m^2
- Distributed mass of beam and sleepers: $m = 268$ kg/m
- Beam bending stiffness: $EI = 6.42\times10^6$ N/m^2
- Constant load amplitude: $F_0 = 8\times10^4$ N
- Load velocity: $v = 200$ m/s

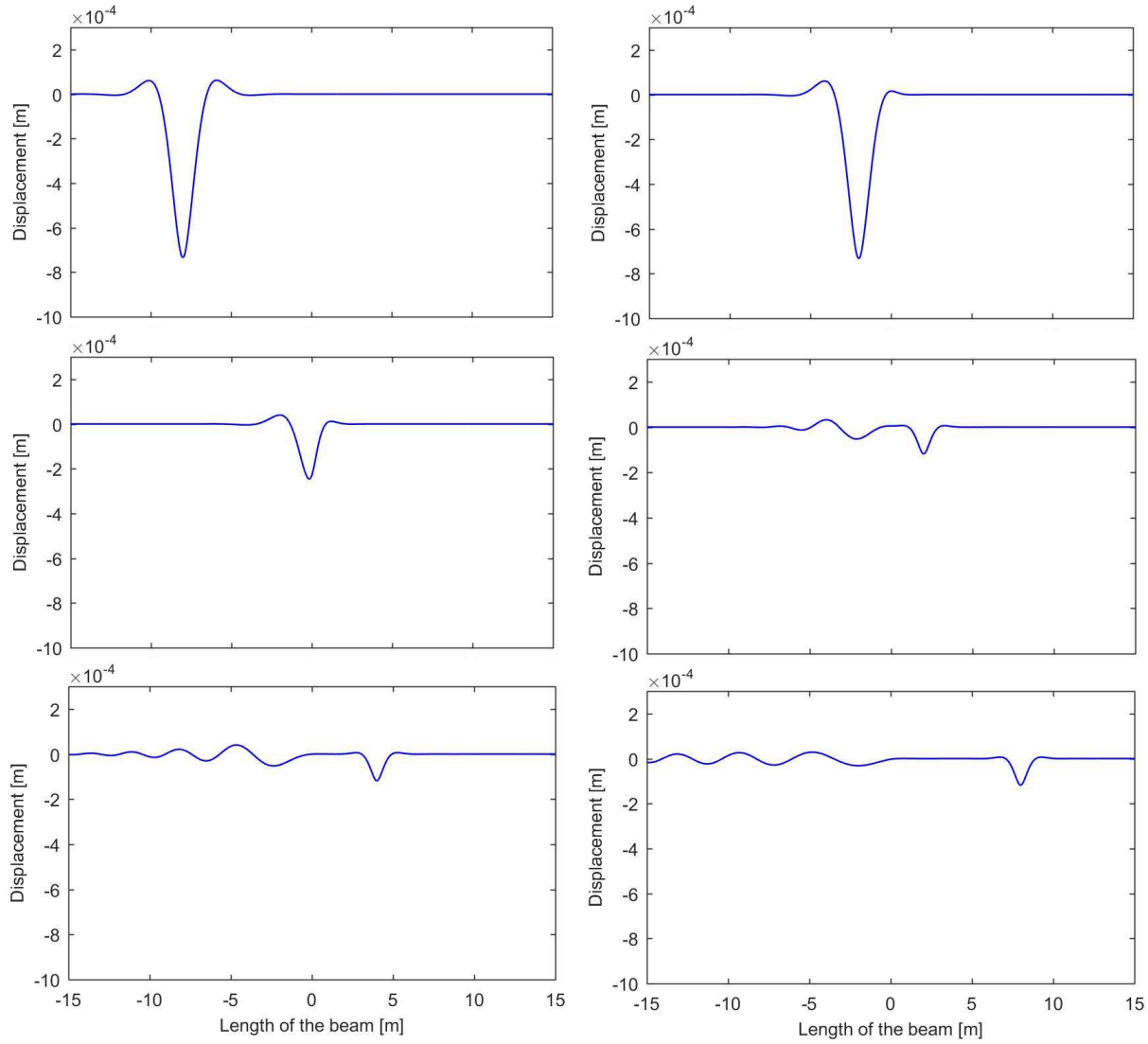

Figure 2.8 – Displacement field at different time moments for a jump in stiffness of 10 times

From the plots in Figure 2.8, it can be observed that the transition radiation is more powerful in the part of the system with softer Winkler stiffness. Moreover, as van Dalen [3] has showed, as the load velocity approaches the wave speed in the system, the transition radiation is more powerful.

In this section, the transient solution has been derived by means of the transform method. Also, the methodology of approximating the inverse Fourier transform numerically has been introduced and used. Finally, the results have been presented in Figure 2.8, in which the transient behaviour consists of the transition radiation. In the next chapter the finite system and the challenges that come with it are discussed and analysed.

3. Finite system

In reality, the stiffness transition between a softer soil to a stiffer bridge is not always as abrupt as presented in the previous chapter, but develops over a certain length. Consequently, for a model to be more realistic, it must incorporate a smooth Winkler stiffness transition, as presented in Figure 3.1.

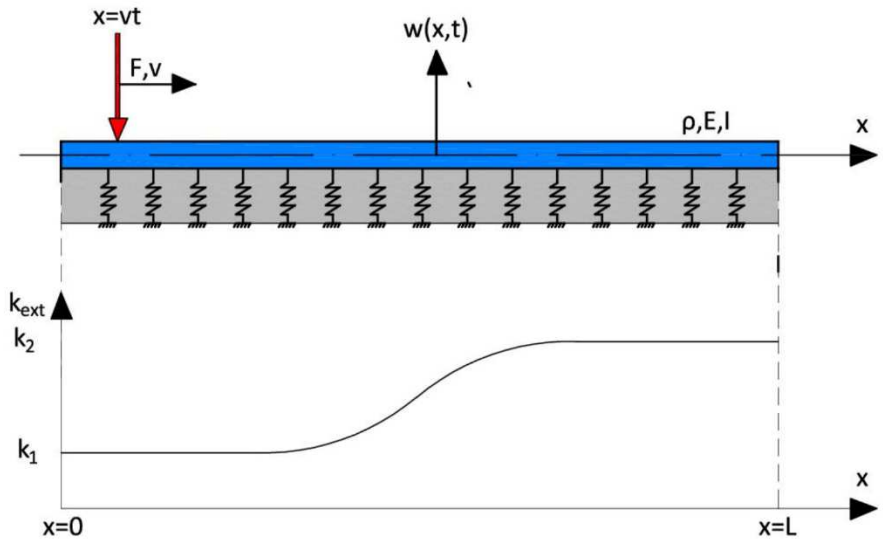

Figure 3.1 – Finite system with smooth Winkler stiffness transition

Incorporating a smooth stiffness transition is very cumbersome to do analytically (see Wolfert 1999 [1]), therefore numerical methods represent a good alternative. When numerical methods are used, the system must be finite, because an infinite system would require an infinite number of elements when analysed numerically. However, as discussed in the previous chapter, the real behaviour of a railway track is represented by an infinite system. This leads to two possibilities: either make the finite system long enough such that it exhibits similar behaviour as an infinite system, or apply a special set of boundaries to account for the missing semi-infinite parts at the left and right of the finite domain. The first option can become very computationally expensive, especially if the model is further developed as a two-dimensional model. Moreover, once wave radiation is excited by the transition and waves travel towards the boundaries, depending on the boundaries imposed these waves can get reflected back and strongly influence the behaviour in the vicinity of the transition. Consequently, the second option is chosen in this thesis, to impose a set of boundaries such that the finite system exhibits exactly the same behaviour as an infinite system. This allows the domain of the finite system to be short, therefore computationally inexpensive. This set of boundaries are referred to as non-reflective boundaries throughout the thesis.

The finite system also poses two other issues. In the previous chapter, we assumed that the moving load entered the domain very far from the transition zone, such that the initial conditions did not play a significant role in the derivation of the solution. The finite domain and the desire for the domain to be as small as possible, lead to the load entering the domain close to the transition zone. As a result, waves are excited by the load entering the domain, which are not present in the infinite system that we aim to mimic. The same issue arises at the end of the finite domain, where at some point in time, the load exits the finite domain leading to unrealistic excitation of free waves.

In this chapter the issues raised above are addressed. Firstly, the issues posed by the load entering and exiting the domain are demonstrated and addressed by using an infinite system. Next, a set of non-reflective boundary conditions are derived such that the system exhibits exactly the same behaviour as an infinite system. Then, the finite system with a smooth inhomogeneous Winkler stiffness is addressed and solved using the Finite Difference Method, employing the non-reflective boundary conditions. Finally, graphical results and concluding remarks of the chapter are presented.

3.1. Suppression of transient behaviour induced by the load entering and exiting the computational domain

Once the system is finite, the load must enter the domain and also exit it, at certain points in time. This matter induces excitation of waves in the system which do not occur in the equivalent infinite system. Consequently, these transient waves have to be suppressed in order for the model to be realistic. In this section, the two issues raised are first exemplified using an infinite system. In order to do this, a new type of transform method which incorporates initial conditions is introduced. Next, a set of initial conditions are applied to suppress the transients induced by the load entering the domain. Finally, a set of forces acting at the right boundary of the computational domain are derived to suppress the transients induced by the load removal. Note that in this section, the homogeneous Winkler stiffness is used for all derivations.

To derive the transients induced by the load entering and exiting the domain, an infinite system is used. The system analysed in this section can be visualized in Figure 3.2.

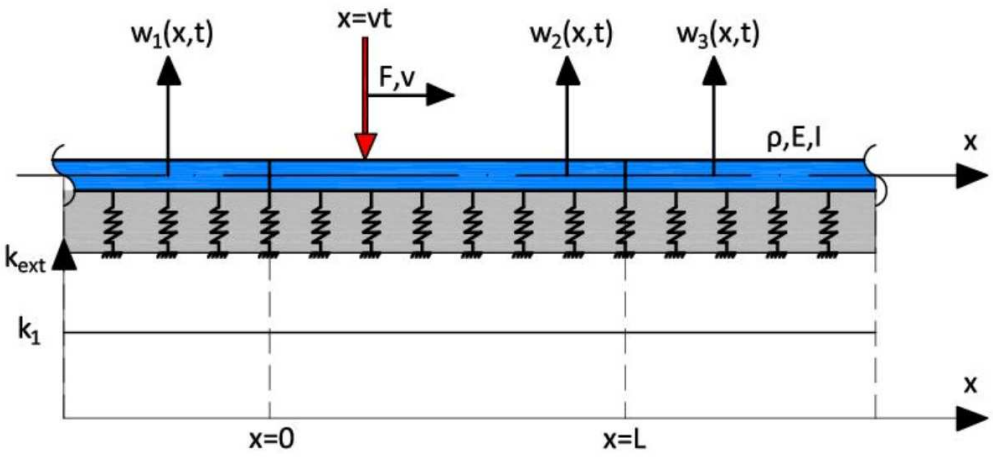

Figure 3.2 – Infinite system with homogeneous Winkler foundation divided in three domains

To demonstrate the transient waves generated by the load entrance and removal, the infinite system is divided into three domains. *Domain 1* represents the semi-infinite domain for $x < 0$, *Domain 2* represents the finite domain for $0 < x < L$, and *Domain 3* the semi-infinite domain for $x > L$. The load is only acting on *Domain 2,* meaning that it enters the domain at $x = 0$ and exits at $x = L$.

The equations of motion describing the behaviour of the three domains read:

$$\begin{aligned} &w_1''''+4\gamma^2\ddot{w}_1+4\beta^4 w_1=0, && x<0,\\ &w_2''''+4\gamma^2\ddot{w}_2+4\beta^4 w_2=-\frac{F_0}{EI}\delta\left(x-vt\right), && 0<x<L,\\ &w_3''''+4\gamma^2\ddot{w}_3+4\beta^4 w_3=0, && x>L. \end{aligned} \tag{3.1}$$

The boundary condition for the semi-infinite domains at $|x|\to\infty$ is the radiation condition. The interface conditions are the same as the ones used for the transform method in Chapter 2.3, just that in this case another four must be imposed at the interface between *Domain 2* and *Domain 3.* The interface conditions read:

$$\begin{aligned} &w_1=w_2,\ w_1'=w_2',\ w_1''=w_2'',\ w_1'''=w_2''', && x=0,\\ &w_2=w_3,\ w_2'=w_3',\ w_2''=w_3'',\ w_2'''=w_3''', && x=L. \end{aligned} \tag{3.2}$$

In this situation, because the load enters at $x=0$, and consequently at $t=0$ due to the delta function's argument, the initial conditions play a role in the derivation of the solution. To incorporate also the influence of the initial conditions in the transform method, explained in Chapter 2.3, another transform method must be used, namely the Laplace transform. This is defined by the following set of forward and inverse transforms:

$$\hat{w}\left(x,s\right)=\int_0^\infty w\left(x,t\right)e^{-st}dt, \tag{3.3}$$

$$w\left(x,t\right)=\frac{1}{2\pi i}\lim_{\omega\to\infty}\int_{\sigma-i\omega}^{\sigma+i\omega}\hat{w}\left(x,s\right)e^{st}ds, \tag{3.4}$$

where $s=\sigma+i\omega$ represents the complex Laplace variable, σ is the real part of the variable, usually chosen very small, ω represents the frequency and the *"over-hat"* marks the Laplace-domain expressions. In the case of choosing the real part of the Laplace variable as zero and considering trivial initial conditions, the inverse Laplace integral reduces to the inverse Fourier integral. However, the forward integrals are still different. After applying the forward Laplace transform to the equations of motion, eq. (3.1), they become:

$$\begin{aligned} &\hat{w}_1''''-k^4\hat{w}_1=4\gamma^2\left(sw_1\left(x,0\right)+\dot{w}_1\left(x,0\right)\right), && x<0,\\ &\hat{w}_2''''-k^4\hat{w}_2=-\frac{F_0}{vEI}e^{-s\frac{x}{v}}+4\gamma^2\left(sw_2\left(x,0\right)+\dot{w}_2\left(x,0\right)\right), && 0<x<L,\\ &\hat{w}_3''''-k^4\hat{w}_3=4\gamma^2\left(sw_3\left(x,0\right)+\dot{w}_3\left(x,0\right)\right), && x>L, \end{aligned} \tag{3.5}$$

where $k=\sqrt[4]{-4\gamma^2s^2-4\beta^4}$ and $w_{1,2,3}\left(x,0\right)$, $\dot{w}_{1,2,3}\left(x,0\right)$ represent the initial displacement and initial velocity, respectively, of each of the three domains.

The branches of the radical have to be formally defined. For the real part of the Laplace variable greater than zero, the radical is always complex valued. Therefore, the necessary and sufficient conditions are: $\mathrm{Re}\{k\} \geq 0$ and $\mathrm{Im}\{k\} \leq 0$.

To demonstrate the transients induced by the load entering the domain, a trivial initial state is chosen, representing that the system is at rest before the load enters. The solutions of the semi-infinite domains, accounting for the radiation condition, are similar to the ones derived in Chapter 2.3, except that they do not incorporate the particular solution due to the moving load because, in this case, the load does not act on these domains. Therefore, they read:

$$\hat{w}_1(x,s) = A_2 e^{ikx} + A_3 e^{kx}, \qquad x < 0,$$
$$\hat{w}_3(x,s) = C_1 e^{-ikx} + C_4 e^{-kx}, \qquad x > L. \tag{3.6}$$

The homogeneous solution for the second domain contains all four types of free waves because the domain is finite, therefore the radiation condition does not apply. Physically this implies that waves can travel both forward and backward throughout the domain and their amplitudes depend on the behaviour at the interfaces with the semi-infinite domains, eq. (3.2). The procedure of deriving the particular solution due to the moving load is exactly the same as in Chapter 2.3. Combining the particular and the homogeneous solutions results in the solution of the second domain, which reads:

$$\hat{w}_2(x,s) = B_1 e^{-ikx} + B_2 e^{ikx} + B_3 e^{kx} + B_4 e^{-kx} - \frac{F_0 v^3}{EI} \frac{1}{s^4 - k^4 v^4} e^{-s\frac{x}{v}}, \quad 0 < x < L. \tag{3.7}$$

Substituting the Laplace domain solutions of the three domains into the interface conditions, eq. (3.2), results in an algebraic system of eight equations with eight unknowns which can easily be solved for the unknown amplitudes in the equations of motion. The eight unknowns read:

$$A_2 = -\frac{1}{4}\frac{F_0}{EIk^3}\frac{1}{is-kv} + \frac{1}{4}\frac{F_0}{EIk^3}\frac{e^{-L(s+ikv)/v}}{is-kv} \qquad C_1 = -\frac{1}{4}\frac{F_0}{EIk^3}\frac{1}{is+kv} + \frac{1}{4}\frac{F_0}{EIk^3}\frac{e^{-L(s-ikv)/v}}{is+kv}$$
$$A_3 = \frac{1}{4}\frac{F_0}{EIk^3}\frac{1}{s+kv} - \frac{1}{4}\frac{F_0}{EIk^3}\frac{e^{-L(s+kv)/v}}{s+kv} \qquad C_4 = \frac{1}{4}\frac{F_0}{EIk^3}\frac{1}{s-kv} - \frac{1}{4}\frac{F_0}{EIk^3}\frac{e^{-L(s-kv)/v}}{s-kv}$$
$$B_2 = \frac{1}{4}\frac{F_0}{EIk^3}\frac{e^{-L(s+kv)/v}}{is-kv} \qquad B_1 = -\frac{1}{4}\frac{F_0}{EIk^3}\frac{1}{is+kv}$$
$$B_3 = -\frac{1}{4}\frac{F_0}{EIk^3}\frac{e^{-L(s+kv)/v}}{s+kv} \qquad B_4 = \frac{1}{4}\frac{F_0}{EIk^3}\frac{1}{s-kv} \tag{3.8}$$

From the expressions of the amplitudes of the waves, eq. (3.8), one can judge their physical meaning by inspecting their exponentials. In *Domain 1*, there are waves traveling to the left due to the load entering *Domain 2* (blue line), as well as due to the load exiting *Domain 2* (green line). In *Domain 3*, there are waves traveling to the right due to the load entering *Domain 2* (yellow line), as well as due to the load exiting *Domain 2* (black line). In *Domain 2*, there are waves traveling towards the right boundary ($x = L$) due to the load entering the domain (purple line) and waves traveling towards the left boundary ($x = 0$) due to the load exiting the domain (red line). To better understand the nature of

these waves, we apply the inverse Laplace transform to all three solutions to obtain the response in the time domain. In Figure 3.3, the transients due to the load entering and exiting the domain are visualized. The parameters used for the plots are the same as in section 2.4.

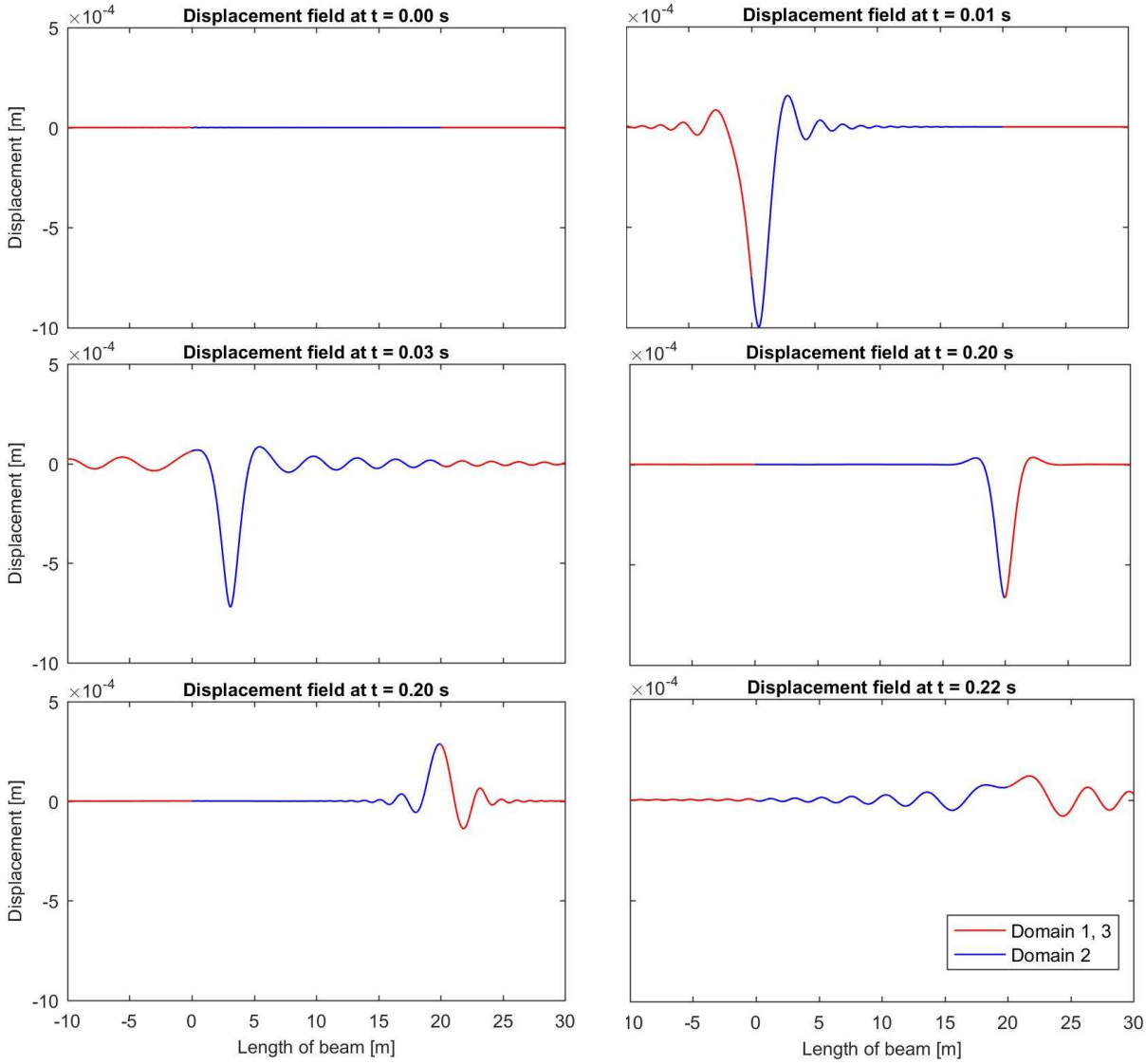

Figure 3.3 – The displacement fields at different time moments for the system with trivial initial conditions and the moving load acting only on Domain 2

At time $t = 0$ s, the system is at rest due to trivial initial conditions imposed. Once the load enters the domain, it generates significant transient behaviour in all three domains. For this visualization, the system possesses damping so that, once the load reaches the right-most boundary, the free waves due to the load entrance are damped out. This is done to visualize the free waves due to the different factors individually. Right after the load exit, clearly other free waves propagate throughout the system.

For the model to be more realistic, these transient waves, observed in Figure 3.3, must be suppressed. First, we address the waves generated by the load entering the domain by prescribing a set of initial conditions. The load is considered to have travelled a long time before reaching the computational domain, thus it is natural to assume that it is in the steady-state regime. Consequently, by applying the initial conditions based on the eigenfield evaluated at $t = 0$, the transients induced by the load entering

the domain must be suppressed. Evaluating the eigenfield, eq. (2.17), and its time derivative at $t = 0$, the set of initial conditions reads:

$$w(x,t=0) = -\frac{iF_0}{2EI}\frac{1}{k_1^{\,2}-k_2^{\,2}}\left(\frac{1}{k_1}e^{ik_1|x|}+\frac{1}{k_2}e^{-ik_2|x|}\right), \qquad -\infty < x < \infty,$$

$$\dot{w}(x,t=0) = -\frac{F_0 v}{2EI}\frac{1}{k_1^{\,2}-k_2^{\,2}}\left(e^{-ik_1 x}-e^{ik_2 x}\right), \qquad x < 0,$$

$$\dot{w}(x,t=0) = -\frac{F_0 v}{2EI}\frac{1}{k_1^{\,2}-k_2^{\,2}}\left(-e^{ik_1 x}+e^{-ik_2 x}\right), \qquad x > 0. \tag{3.9}$$

It is important to realise that these initial conditions have to be applied to *Domain 2* as well as to *Domain 1* and *Domain 3* (if the eigenfield displacement or velocity reaches *Domain 3*). Substituting these initial conditions in the Laplace-domain equations of motion, one obtains:

$$\hat{w}_1'''' - k^4\hat{w}_1 = -\frac{F_0}{2EI}\frac{4\gamma^2}{k_1^{\,2}-k_2^{\,2}}\left(\frac{1}{k_1}(is+k_1 v)e^{-ik_1 x}+\frac{1}{k_2}(is-k_2 v)e^{ik_2 x}\right), \qquad x < 0,$$

$$\hat{w}_2'''' - k^4\hat{w}_2 = -\frac{F_0}{2EI}\frac{4\gamma^2}{k_1^{\,2}-k_2^{\,2}}\left(\frac{1}{k_1}(is-k_1 v)e^{ik_1 x}+\frac{1}{k_2}(is+k_2 v)e^{-ik_2 x}\right)-\frac{F_0}{vEI}e^{-s\frac{x}{v}}, \qquad 0 < x < L,$$

$$\hat{w}_3'''' - k^4\hat{w}_3 = -\frac{F_0}{2EI}\frac{4\gamma^2}{k_1^{\,2}-k_2^{\,2}}\left(\frac{1}{k_1}(is-k_1 v)e^{ik_1 x}+\frac{1}{k_2}(is+k_2 v)e^{-ik_2 x}\right), \qquad x > L. \tag{3.10}$$

The procedure of deriving the particular solutions corresponding to the initial state is similar to the one corresponding to the moving load, as explained in section 2.3. The only difference comes from the fact that the initial conditions contain two different forms for the spatial distribution, therefore two amplitudes must be derived, one for each spatial form. The assumed particular solutions read:

$$\hat{w}_{1,p} = P_1 e^{-ik_1 x} + P_2 e^{ik_2 x}, \qquad x < 0,$$

$$\hat{w}_{2,p} = Q_1 e^{ik_1 x} + Q_2 e^{-ik_2 x}, \qquad 0 < x < L,$$

$$\hat{w}_{3,p} = R_1 e^{ik_1 x} + R_2 e^{-ik_2 x}, \qquad x > L, \tag{3.11}$$

where P_1, P_2, Q_1, Q_2, R_1 and R_2 are the unknown amplitudes. Substituting these solutions into the inhomogeneous equations of motion, eq. (3.10), one can find the unknowns by equating the amplitudes corresponding to the same exponentials. The determined particular solutions corresponding to the initial conditions become:

$$\hat{w}_{1,p} = -\frac{F_0}{2EI}\frac{4\gamma^2}{k_1^{\,2}-k_2^{\,2}}\left(\frac{1}{k_1}\frac{is-k_1 v}{k_1^4-k^4}e^{-ik_1 x}+\frac{1}{k_2}\frac{is+k_2 v}{k_2^4-k^4}e^{ik_2 x}\right), \qquad x < 0,$$

$$\hat{w}_{2,p} = -\frac{F_0}{2EI}\frac{4\gamma^2}{k_1^2 - k_2^2}\left(\frac{1}{k_1}\frac{is + k_1 v}{k_1^4 - k^4}e^{ik_1 x} + \frac{1}{k_2}\frac{is - k_2 v}{k_2^4 - k^4}e^{-ik_2 x}\right), \qquad 0 < x < L,$$

$$\hat{w}_{3,p} = -\frac{F_0}{2EI}\frac{4\gamma^2}{k_1^2 - k_2^2}\left(\frac{1}{k_1}\frac{is + k_1 v}{k_1^4 - k^4}e^{ik_1 x} + \frac{1}{k_2}\frac{is - k_2 v}{k_2^4 - k^4}e^{-ik_2 x}\right), \qquad x > L. \quad (3.12)$$

To simplify these expressions, one must remember that $k_1^4 - 4\gamma^2 k_1^2 v^2 + 4\beta^4 = 0$ and $k_2^4 - 4\gamma^2 k_2^2 v^2 - 4\beta^4 = 0$ from the dispersion equation and kinematic invariant, derived in section 2.2. Moreover, $k^4 = -4\gamma^2 s^2 - 4\beta^4$ represents the wavenumber of the free waves. Substituting these expressions and rearranging, eq. (3.12) reduces to:

$$\hat{w}_{1,p}(x,s) = -\frac{iF_0}{2EI}\frac{1}{k_1^2 - k_2^2}\left(\frac{1}{k_1}\frac{1}{s - ik_1 v}e^{-ik_1 x} + \frac{1}{k_2}\frac{1}{s + ik_2 v}e^{ik_2 x}\right), \qquad x < 0,$$

$$\hat{w}_{2,p}(x,s) = -\frac{iF_0}{2EI}\frac{1}{k_1^2 - k_2^2}\left(\frac{1}{k_1}\frac{1}{s + ik_1 v}e^{ik_1 x} + \frac{1}{k_2}\frac{1}{s - ik_2 v}e^{-ik_2 x}\right), \qquad 0 < x < L,$$

$$\hat{w}_{3,p}(x,s) = -\frac{iF_0}{2EI}\frac{1}{k_1^2 - k_2^2}\left(\frac{1}{k_1}\frac{1}{s + ik_1 v}e^{ik_1 x} + \frac{1}{k_2}\frac{1}{s - ik_2 v}e^{-ik_2 x}\right), \qquad x > L. \quad (3.13)$$

The homogeneous solutions for all three domains are the same as in the situation with trivial initial conditions, eq. (3.6) and (3.7), and the same holds for the particular solution due to the moving load. Combining the homogeneous solutions and the particular ones, we obtain the solutions in the Laplace domain of all three domains:

$$\hat{w}_1(x,s) = A_2 e^{ikx} + A_3 e^{kx} + \hat{w}_{1,p}, \qquad x < 0,$$

$$\hat{w}_2(x,s) = B_1 e^{-ikx} + B_2 e^{ikx} + B_3 e^{kx} + B_4 e^{-kx} + \hat{w}_{2,p} - \frac{F_0 v^3}{EI}\frac{1}{s^4 - k^4 v^4}e^{-s\frac{x}{v}}, \qquad 0 < x < L$$

$$\hat{w}_3(x,s) = C_1 e^{-ikx} + C_4 e^{-kx} + \hat{w}_{3,p}, \qquad x > L. \quad (3.14)$$

Substituting these solutions into the interface conditions, eq. (3.2), and solving the system of eight algebraic equations for the eight unknown amplitudes, one obtains:

$$A_2 = 0 + \frac{1}{4}\frac{F_0}{EIk^3}\frac{e^{-L(s+ikv)/v}}{is - kv} \qquad C_1 = 0 + \frac{1}{4}\frac{F_0}{EIk^3}\frac{e^{-L(s-ikv)/v}}{is + kv}$$

$$A_3 = 0 - \frac{1}{4}\frac{F_0}{EIk^3}\frac{e^{-L(s+kv)/v}}{s + kv} \qquad C_4 = 0 - \frac{1}{4}\frac{F_0}{EIk^3}\frac{e^{-L(s-kv)/v}}{s - kv}$$

$$B_2 = \frac{1}{4}\frac{F_0}{EIk^3}\frac{e^{-L(s+kv)/v}}{is-kv} \qquad B_1 = 0$$

$$B_3 = -\frac{1}{4}\frac{F_0}{EIk^3}\frac{e^{-L(s+kv)/v}}{s+kv} \qquad B_4 = 0 \tag{3.15}$$

By analyzing the amplitude expressions and comparing them to the ones presented in eq. (3.8), we observe that the terms generated due to the load entering the domain (blue, yellow and purple lines) have become zero. This physically means that the load entering the domain does not excite free waves in the system. Therefore, the goal of suppressing the transients due to the load entry has been achieved.

The only terms left in the amplitudes corresponding to the free waves are those related to the removal of the load. These can be suppressed by implementing a set of forces at the interface between *Domain 2* and *Domain 3,* such that they mimic the effect of the load continuing its movement after has exited *Domain 2*. This set of forces are not known a priori, but can be derived by imposing an unknown shear force and an unknown bending moment, at $x = L$, and determine their expressions such that they cancel the contributions given by the removal of the load in *Domain 2*, namely B_2 and B_3. By applying these unknown forces at the interface between *Domain 2* and *Domain 3,* the new interface conditions, in the Laplace domain, become:

$$\begin{aligned}
&\hat{w}_1 = \hat{w}_2,\ \hat{w}_1' = \hat{w}_2',\ \hat{w}_1'' = \hat{w}_2'',\ \hat{w}_1''' = \hat{w}_2''', && x = 0,\\
&\hat{w}_2 = \hat{w}_3,\ \hat{w}_2' = \hat{w}_3', && x = L,\\
&EI\left(\hat{w}_3'' - \hat{w}_2''\right) = M_r, && x = L,\\
&EI\left(\hat{w}_3''' - \hat{w}_2'''\right) = V_r, && x = L,
\end{aligned} \tag{3.16}$$

where M_r and V_r are the moment and shear force, respectively, and subscript *"r"* stands for removal. These forces are addressed throughout the thesis as the removal forces. Substituting the Laplace-domain solutions including the initial state, eq. (3.14), into the interface conditions, eq. (3.16), one can obtain the amplitudes as functions of the yet unknown removal forces. Equating the obtained expressions for B_2 and B_3 to zero and solving the system of two algebraic equations for the two removal forces, one obtains:

$$V_r = -\frac{1}{2}(1+i)F_0\frac{\left((-1+i)s-2kv\right)e^{-s\frac{L}{v}}}{(s+kv)(s+ikv)},$$

$$M_r = -\frac{F_0 v e^{-s\frac{L}{v}}}{(s+kv)(s+ikv)}. \tag{3.17}$$

The exponential $e^{-s\frac{L}{v}}$ in (3.17), implies that they will be active only at and after time $t = L/v$, which represents the time moment of load exiting the domain. To better understand the nature of these forces, we apply the inverse Laplace transform and graphically represent them in Figure 3.4; details regarding the evaluation of the associated integral are given below.

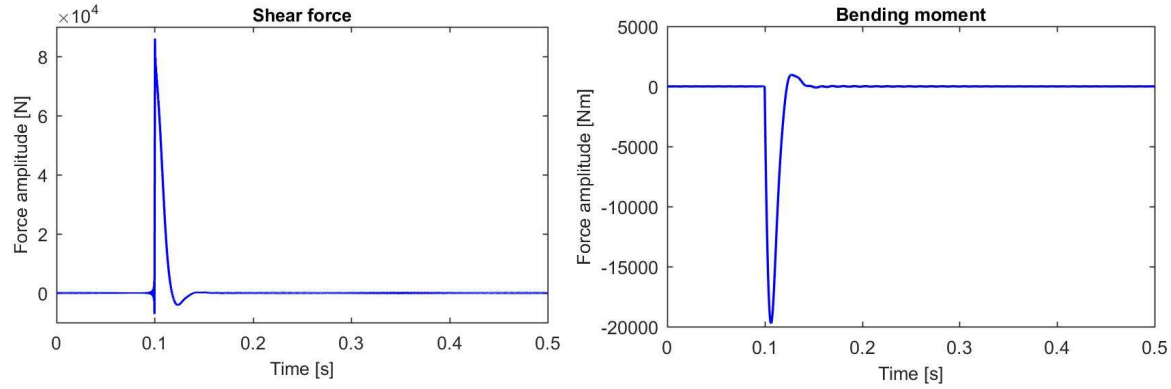

Figure 3.4 - Forces to suppress transients induced by the removal of the load; L/v=0.1 [s]

It can be observed from Figure 3.4 that the forces are inactive until the load exits the domain, which occurs at $L/v = 0.1$ s. At the time moment of exit, the shear force exhibits an immediate jump up to the magnitude of the moving load (80 kN) and decreases gradually, simulating the load moving away from the right boundary. On the other hand, the magnitude of the bending moment only increases gradually to its maximum value after the time of removal.

Applying the removal forces at the interface results in the following expressions for the amplitudes of the free waves of the Laplace domain solutions:

$$A_2 = A_3 = B_1 = B_2 = B_3 = B_4 = 0,$$

$$C_1 = -\frac{1}{2}\frac{iF_0}{EIk^3}\frac{(-1+i)k^2v^2e^{-L(s-ikv)/v}}{(s+kv)(k^2v^2+s^2)},$$

$$C_4 = \frac{1}{2}\frac{iF_0}{EIk^3}\frac{(1+i)k^2v^2e^{-L(s-kv)/v}}{(is-kv)(k^2v^2-s^2)}. \qquad (3.18)$$

The amplitudes of the free waves in *Domain 1* and *Domain 2* become zero. This means that there are no free waves present at all in these domains. In *Domain 3* the amplitudes of the free waves are nonzero, but this is to be expected. The removal forces have been derived such that they ensure a smooth exit for *Domain 2*, this does not ensure the canceling of the free waves in *Domain 3*, as seen from (3.18). This matter does not pose any problems, since the aim was that *Domain 2* exhibits the same behaviour as the infinite system, from the point of view of load entry and load removal, which was successfully achieved.

Considering (3.14) with the determined amplitudes from (3.18) and the particular solutions corresponding to the initial state from (3.13), the final Laplace-domain solutions of the displacement of the three domains are now fully determined. To determine the time-domain displacements, the inverse Laplace transform is performed numerically. When applying the inverse Laplace transform numerically in a straightforward manner, due to the truncation in the frequency the time-domain, the displacement

at and close to $t = 0$ is inaccurate. To this end, the causality principle is employed and two alternative expressions for the inverse Laplace transform are obtained. The original expression for the inverse Laplace transform is:

$$w(x,t) = \frac{1}{2\pi i} \lim_{\omega \to \infty} \int_{\sigma - i\omega}^{\sigma + i\omega} \hat{w}(x,s) e^{st} ds \,. \tag{3.19}$$

Substituting the Laplace variable $s = \sigma + i\omega$, (3.19) reduces to:

$$w(x,t) = \frac{e^{\sigma t}}{2\pi} \int_{-\infty}^{\infty} \hat{w}(x,\omega) e^{i\omega t} d\omega \,. \tag{3.20}$$

Considering that $\mathrm{Im}\left\{\hat{w}(x,\omega) e^{i\omega t}\right\}$ is an antisymmetric function and $\mathrm{Re}\left\{\hat{w}(x,\omega) e^{i\omega t}\right\}$ is a symmetric function, also considering the truncation limit, (3.20) becomes:

$$w(x,t) = \frac{e^{\sigma t}}{\pi} \int_{0}^{\omega_{tr}} \mathrm{Re}\left\{\hat{w}(x,\omega) e^{i\omega t}\right\} d\omega \,. \tag{3.21}$$

The two alternative expressions read:

$$w(x,t) = \frac{2e^{\sigma t}}{\pi} \int_{0}^{\omega_{tr}} \mathrm{Re}\left\{\hat{w}(x,\omega)\right\} \cos(\omega t)\, d\omega \,,$$

$$w(x,t) = -\frac{2e^{\sigma t}}{\pi} \int_{0}^{\omega_{tr}} \mathrm{Im}\left\{\hat{w}(x,\omega)\right\} \sin(\omega t)\, d\omega \,. \tag{3.22}$$

If the integral over frequency were not truncated, (3.20) and (3.22) would be completely equivalent. In Figure 3.5, we can observe the differences obtained in the response at $t = 0$, eq. (3.14) with amplitudes from (3.18), by using each of these three expressions for the inverse Laplace transform.

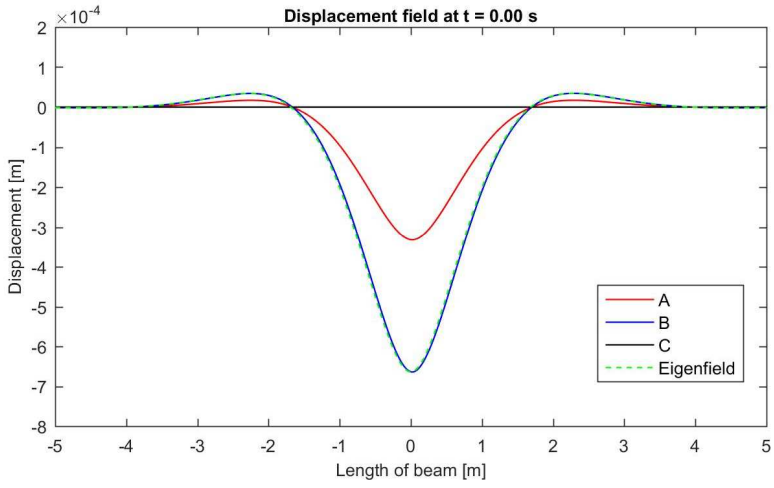

Figure 3.5 - Displacement field at t=0 obtained by applying inverse Laplace transform to eq. (3.14) using: Re{ŵ exp(iωt)} (A), alternative expression Re{ŵ}cos(ωt) (B), alternative expression Im{ŵ}sin(ωt)

From Figure 3.5, it is clear that using the first alternative expression in (3.22), the best results at and close to $t = 0$ are obtained. The reason is that $\cos(0) = 1$, meaning that at $t = 0$, the displacement will exhibit the shape imposed by the initial displacement. The sine alternative expression gives a zero initial displacement, while the exponential gives an average between these two. The drawback of using the cosine expression is that the velocity exhibited by the response, close to $t = 0$, is considerably smaller compared to the imposed initial velocity. However, the error introduced by the small exhibited initial velocity is negligible, because the time-domain response exhibits the correct behaviour, as can be seen in Figure 3.6. The cosine expression in (3.22) is used throughout Chapter 3. In section 4.2, this matter will be again addressed.

Applying the inverse Laplace transform to the Laplace-domain solutions of the three domains, the time-domain displacements are obtained. These are visualized in Figure 3.6.

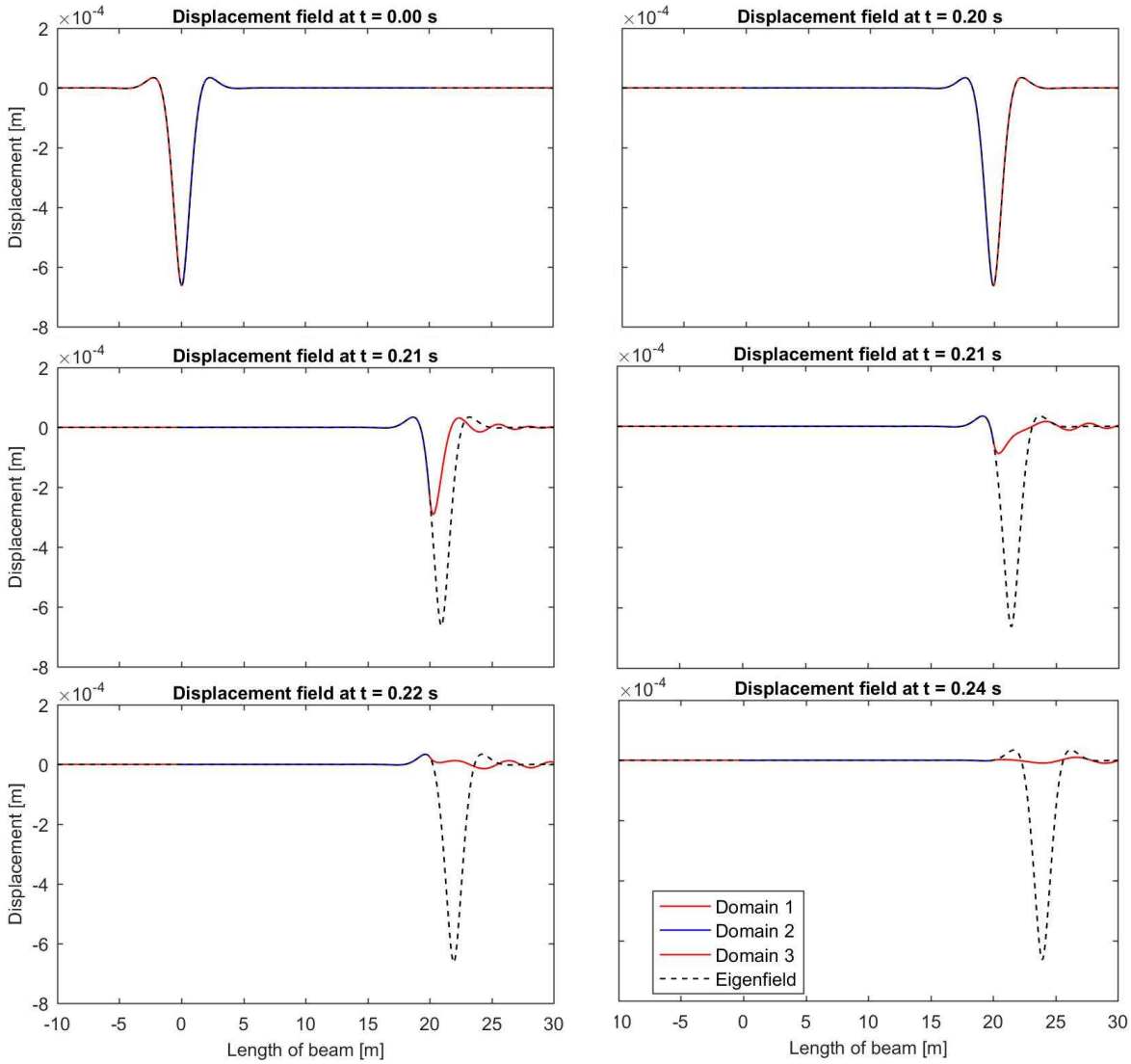

Figure 3.6 – The displacement fields at different time moments for the system with tuned initial conditions, removal of the load forces and the moving load acting only on Domain 2, against the eigenfield

It can be seen in Figure 3.6 that the removal forces ensure a smooth exit of the load for the computational domain (*Domain 2*), which exhibits exactly the same behaviour as the eigenfield. *Domain 3* exhibits free waves due to the removal of the load, but this does not affect the solution in the computational domain. When comparing Figure 3.6 with Figure 3.3, we observe that the transient waves induced by the load entrance and removal have been totally suppressed for *Domain 2*. Therefore, the finite *Domain 2* exhibits exactly the same behaviour as the infinite system.

In this section we have addressed the issues of the load entering and exiting the finite domain. The transient waves generated by the load entrance have been suppressed by imposing a set of initial conditions derived based on the steady-state eigenfield. The transient waves generated by the load exit have been suppressed by imposing a set of forces at the interface ($x = L$) ensuring a smooth exit of the moving load. Also, an alternative expression for the inverse Laplace transform has been introduced. In the next section, the two semi-infinite domains, *Domain 1* and *Domain 3* are replaced by a set of boundary conditions to mimic their behaviour without the need of solving the equations of motion of the two semi-infinite domains.

3.2. Derivation of the non-reflective boundary conditions

In this section, a set of boundary conditions are derived to represent the behaviour of the two semi-infinite domains at the left and right of the computational domain, eliminating the need to also derive the response of these domains. The set of boundary conditions are derived by means of the substructuring method. Firstly, the substructuring method is presented. Next, the boundary conditions are derived. Finally, the system incorporating these boundary conditions is solved and the results are visualized. It must be noted that, once more, the derivation of the boundary conditions is performed for the system with homogeneous Winkler foundation because it allows for an analytical solution in the Laplace domain.

The substructuring method enables one to analyse the dynamic behaviour of the substructures individually and analyse the dynamic behaviour of the entire system by coupling the individual substructures. As seen in the previous section, the moving load acts only on the computational domain. Consequently, the only excitation of the two semi-infinite domains comes from the interface with the computational domain. Therefore, solving the two semi-infinite domains individually and expressing their behaviour as functions of the excitation at the interfaces, one can replace them by a set of boundary conditions. Applying this procedure enables us to finally only solve the computational domain, therefore reducing the computational time considerably. Firstly, the substructuring is performed for the left semi-infinite domain. The substructuring procedure for our case can be visualized in Figure 3.7.

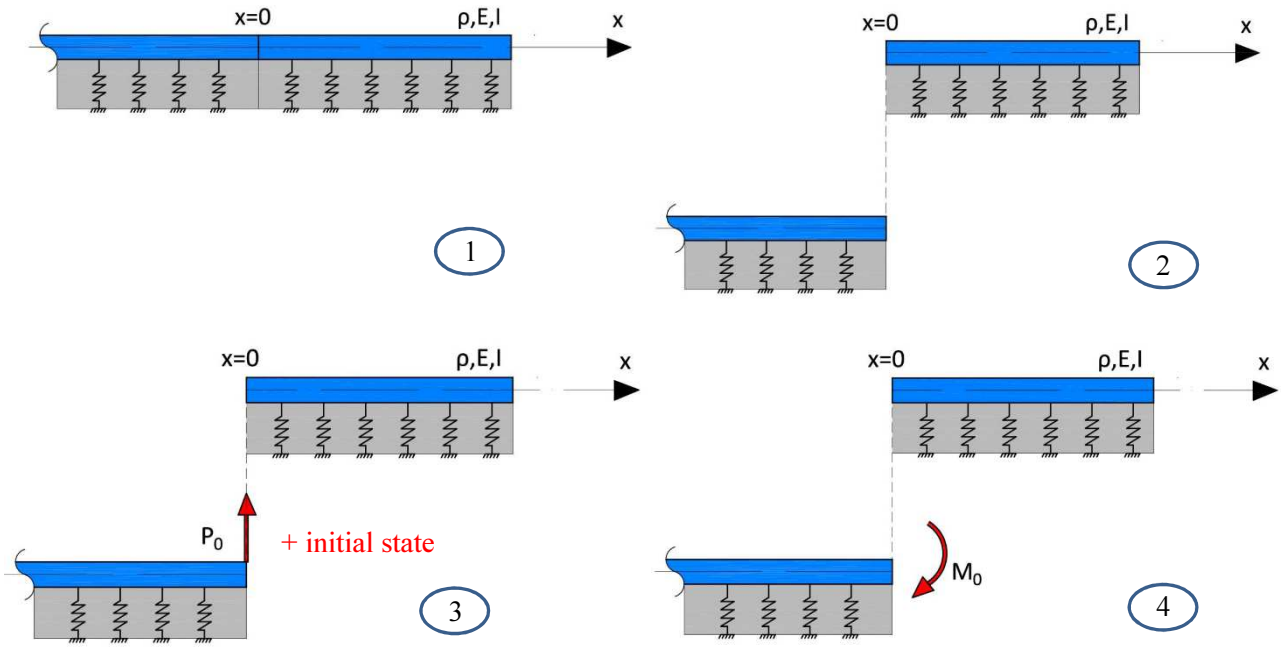

Figure 3.7 – Substructuring procedure description; 1) the actual system; 2) isolate the substructure; 3) apply a general shear force and general initial state; 4) apply a general bending moment

Firstly, the semi-infinite domain at the left of the computational domain is isolated. The aim of the procedure is to determine the reaction of the semi-infinite domain at the interface ($x = 0$) due to excitation at the interface. To this end, an unknown shear force, P_0, and an unknown bending moment, M_0, are exerted at the interface. Moreover, as seen in section 3.1, the semi-infinite domains are

subjected to non-trivial initial state to suppress the transient waves generated by the load entrance. Due to the linearity of the system, the principle of superposition is employed. Therefore, in *case 1* the shear force combined with the initial state are applied first (panel 3 of Figure 3.7) and the corresponding solution is derived. Separately, in *case 2* the bending moment is applied (panel 4 of Figure 3.7), and the corresponding solution is derived as well. The total solution of the semi-infinite system subjected to the shear force, bending moment and initial state is the superposition of the solutions from the two cases. Finally, once the total solutions for the displacement and slope are obtained, as functions of the shear force, P_0, and bending moment, M_0, we express these forces in terms of the displacement and slope. These forces represent the non-reflective boundaries. In the following, the substructuring method is performed.

The Laplace domain equation of motion of the semi-infinite domain at the left of the computational domain is the same as derived in the previous sections and reads:

$$\hat{w}_1'''' - k^4 \hat{w}_1 = 4\gamma^2 \left(s w_1(x,0) + \dot{w}_1(x,0) \right), \qquad x < 0 . \tag{3.23}$$

The solution to the homogeneous Laplace domain equation of motion is also the same as derived in the previous section and reads:

$$\hat{w}_1(x,s) = A_2 e^{ikx} + A_3 e^{kx}, \qquad x < 0 . \tag{3.24}$$

In the following, *case 1* introduced above is addressed.

1) Applied shear force and initial state

The initial state, eq. (3.2), and the particular solution corresponding to the initial state, eq. (3.11), have been derived in the previous section. Although the particular solution is determined in a closed form, the analysis in this section is performed using a particular solution for a general initial state. This is done because we make use of the general initial state in Chapter 4. At the end of the current derivation the general particular solution is replaced by (3.11) to account for the specific initial state imposed, namely the eigenfield. The Laplace-domain displacement, therefore, is a superposition of the solution to the homogeneous equation of motion and the generalized particular solution, and reads:

$$\hat{w}_1(x,s) = A_2 e^{ikx} + A_3 e^{kx} + \hat{w}_{1,p}, \qquad x < 0 . \tag{3.25}$$

The boundary conditions for the applied shear force case, are:

$$\begin{aligned} -EI\hat{w}_{1,V}''' &= P_0, \qquad x = 0, \\ \hat{w}_{1,V}'' &= 0, \qquad x = 0, \end{aligned} \tag{3.26}$$

where subscript V stands for the case of applied shear force. The two unknows in (3.25) are found by substituting it into the boundary conditions, eq. (3.26). The slope is also be determined, because of the coupling between applied shear force and resulting slope, by taking the first spatial derivative of the displacement. The two expressions, the displacement and slope are evaluated at the interface, $x = 0$, because the aim is to derive the response of the semi-infinite domain at the interface. Therefore, the Laplace domain displacement and slope in *case 1*, evaluated at the interface, are:

$$\hat{w}_{1,P}(0,s) = \frac{-1-i}{EIk^3} P_0 - \frac{1+i}{k^3} \hat{w}'''_{1,p}\Big|_{x=0} + \frac{i}{k^2} \hat{w}''_{1,p}\Big|_{x=0} + \hat{w}_{1,p}\Big|_{x=0},$$

$$\hat{w}'_{1,P}(0,s) = \frac{-i}{EIk^2} P_0 - \frac{i}{k^2} \hat{w}'''_{1,p}\Big|_{x=0} - \frac{1-i}{k} \hat{w}''_{1,p}\Big|_{x=0} + \hat{w}'_{1,p}\Big|_{x=0}. \tag{3.27}$$

In the following, *case 2* as introduced previously is addressed.

2) Applied bending moment

In the current derivation, the initial state is not included so that it is not accounted for twice, since the two solutions of *case 1* and *case 2* are superimposed finally. Consequently, only the solution to the homogeneous equation of motion is used for this derivation, namely eq. (3.24). The boundary conditions for the applied bending moment case read:

$$\hat{w}'''_{1,M} = 0, \qquad x = 0,$$

$$-EI\hat{w}''_{1,M} = M_0, \qquad x = 0. \tag{3.28}$$

The two unknowns in (3.24) are found by substituting it in the boundary conditions, eq. (3.28). Once again, the slope is also determined by taking the first spatial derivative of the displacement. Evaluating the obtained displacement and slope at the interface, $x = 0$, they read:

$$\hat{w}_{1,M}(0,s) = \frac{1+i}{EIk^2} M_0,$$

$$\hat{w}'_{1,M}(0,s) = \frac{-1+i}{EIk} M_0. \tag{3.29}$$

To determine the entire expressions for the displacement and slope, the solutions derived in *case 1* and *case 2* are superimposed. Rewriting those in a matrix form, one obtains:

$$\begin{pmatrix} \hat{w}_1(0,s) \\ \hat{w}'_1(0,s) \end{pmatrix} = \underbrace{\begin{pmatrix} \frac{-1-i}{EIk^3} & \frac{i}{EIk^2} \\ \frac{-i}{EIk^2} & \frac{-1+i}{EIk} \end{pmatrix}}_{\text{Compliance matrix } \mathbf{C}} \begin{pmatrix} P_0 \\ M_0 \end{pmatrix} + \mathbf{B}, \tag{3.30}$$

where **B** is the vector incorporating the contributions from the initial state, and reads:

$$\mathbf{B} = \begin{pmatrix} -\frac{1+i}{k^3} \hat{w}'''_{1,p}\Big|_{x=0} + \frac{i}{k^2} \hat{w}''_{1,p}\Big|_{x=0} + \hat{w}_{1,p}\Big|_{x=0} \\ -\frac{i}{k^2} \hat{w}'''_{1,p}\Big|_{x=0} - \frac{1-i}{k} \hat{w}''_{1,p}\Big|_{x=0} + \hat{w}'_{1,p}\Big|_{x=0} \end{pmatrix}. \tag{3.31}$$

To obtain the expressions of the unknown shear force, P_0, and bending moment, M_0, as functions of the displacement and slope at the interface, the compliance matrix is inverted, thus obtaining the stiffness matrix: $\mathbf{K}=\mathbf{C}^{-1}$. Equation (3.30) is now left-multiplied by the stiffness matrix and after rearranging, the expressions for the two forces are obtained. They read:

$$\begin{pmatrix} P_0 \\ M_0 \end{pmatrix} = \underbrace{EI\begin{pmatrix} (-1+i)k^3 & -ik^2 \\ ik^2 & (-1-i)k \end{pmatrix}}_{\text{Stiffness matrix } \mathbf{K}} \begin{pmatrix} \hat{w}_1(0,s) \\ \hat{w}_1'(0,s) \end{pmatrix} - \mathbf{D_0}, \tag{3.32}$$

where vector $\mathbf{D_0}$ incorporates the contribution from the initial state and reads:

$$\mathbf{D_0} = EI\begin{pmatrix} \hat{w}_{1,p}'''\big|_{x=0} - ik^2\,\hat{w}_{1,p}'\big|_{x=0} + (-1+i)k^3\,\hat{w}_{1,p}\big|_{x=0} \\ \hat{w}_{1,p}''\big|_{x=0} - (1+i)k\,\hat{w}_{1,p}'\big|_{x=0} + ik^2\hat{w}_{1,p}\big|_{x=0} \end{pmatrix}. \tag{3.33}$$

Considering (3.32) and (3.33), the non-reflective boundary conditions, for the left edge of the computational domain, are fully determined. To derive expressions for the right boundary, the same procedure is used. A concise derivation of the non-reflective boundary conditions at the right edge of the computational domain is presented in the following.

The Laplace domain solution and the boundary conditions for *case 1,* of applied shear force and initial state, read:

$$\hat{w}_3(x,s) = C_1 e^{-ikx} + C_4 e^{-kx} + \hat{w}_{3,p}, \qquad x > L, \tag{3.34}$$

$$EI\hat{w}_{3,V}''' = P_L, \qquad x = L,$$

$$\hat{w}_{3,V}'' = 0, \qquad x = L. \tag{3.35}$$

The displacement and slope, evaluated at $x = L$, read:

$$\hat{w}_{3,P}(L,s) = \frac{-1-i}{EIk^3}P_L + \frac{1+i}{k^3}\hat{w}_{3,p}'''\big|_{x=L} + \frac{i}{k^2}\hat{w}_{3,p}''\big|_{x=L} + \hat{w}_{1,p}\big|_{x=L},$$

$$\hat{w}_{3,P}'(L,s) = \frac{i}{EIk^2}P_L - \frac{i}{k^2}\hat{w}_{3,p}'''\big|_{x=L} + \frac{1-i}{k}\hat{w}_{3,p}''\big|_{x=L} + \hat{w}_{3,p}'\big|_{x=L}. \tag{3.36}$$

The Laplace domain solution for *case 2,* of applied bending moment, is the homogeneous part of (3.34). The boundary conditions for *case 2* read:

$$\hat{w}_{3,V}''' = 0, \qquad x = L,$$

$$EI\hat{w}_{3,V}'' = M_L, \qquad x = L. \tag{3.37}$$

The displacement and slope, evaluated at $x = L$, then read:

$$\hat{w}_{3,M}(L,s) = \frac{-i}{EIk^2} M_L,$$
$$\hat{w}'_{3,M}(L,s) = \frac{-1+i}{EIk} M_L. \tag{3.38}$$

Following the same procedure of superimposing the solutions from the two cases, rewriting the expressions in a matrix form, inverting the compliance matrix and left-multiplying the whole expression by the stiffness matrix, the shear force and bending moment become:

$$\begin{pmatrix} P_L \\ M_L \end{pmatrix} = EI \begin{pmatrix} (-1+i)k^3 & ik^2 \\ -ik^2 & (-1-i)k \end{pmatrix} \begin{pmatrix} \hat{w}_3(L,s) \\ \hat{w}'_3(L,s) \end{pmatrix} - \mathbf{D_L}, \tag{3.39}$$

where vector $\mathbf{D_L}$ incorporates the contribution from the initial state and reads:

$$\mathbf{D_L} = EI \begin{pmatrix} -\hat{w}'''_{3,p}\big|_{x=L} + ik^2\,\hat{w}'_{3,p}\big|_{x=L} + (-1+i)k^3\,\hat{w}_{3,p}\big|_{x=L} \\ -\hat{w}''_{3,p}\big|_{x=L} - (1+i)k\,\hat{w}'_{3,p}\big|_{x=L} - ik^2\hat{w}_{3,p}\big|_{x=L} \end{pmatrix}. \tag{3.40}$$

Considering (3.32) and (3.39), both non-reflective boundaries have been obtained. To validate them, the computational domain with initial state, removal of the load forces and non-reflective boundaries is solved in the following and compared to the eigenfield. The system to be solved is visualized in Figure 3.8.

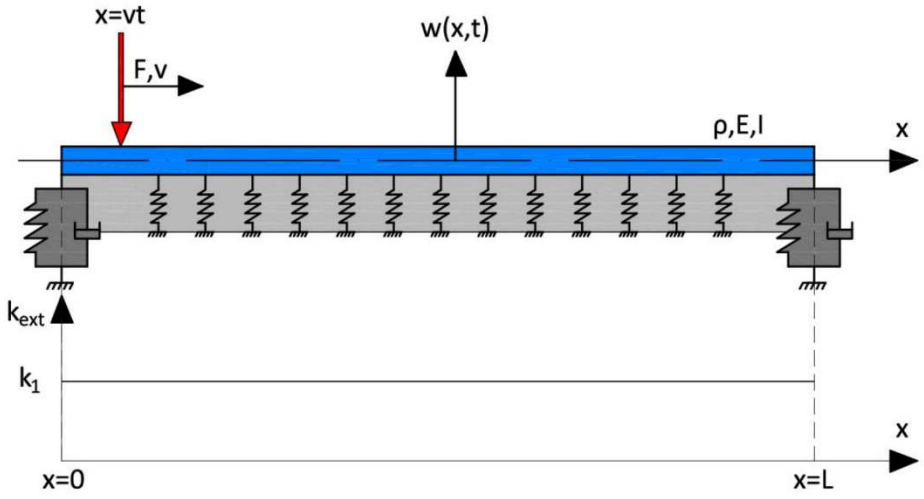

Figure 3.8 - Finite system with non-reflecting boundaries and homogeneous Winkler stiffness

The Laplace domain equation of motion and the initial state of the computational domain are the same as in the previous section, eq. (3.1) and (3.2), respectively. The displacement solution is also the same as in the previous section, eq. (3.14), and reads:

$$\hat{w}(x,s) = B_1 e^{-ikx} + B_2 e^{ikx} + B_3 e^{kx} + B_4 e^{-kx} + \hat{w}_p - \frac{F_0 v^3}{EI} \frac{1}{s^4 - k^4 v^4} e^{-s\frac{x}{v}}, \quad 0 < x < L, \tag{3.41}$$

where the particular solution corresponding to the initial state is given by (3.13). The difference compared to the last section lies in the boundary conditions. Because the semi-infinite domains have been replaced by non-reflective boundaries, instead of interface conditions, boundary conditions are applied. The Laplace domain boundary conditions read:

$$\begin{aligned} &EI\hat{w}''' + k_{Vt}\hat{w} - k_{Vr}\hat{w}' - D_{0,1} = 0, && x = 0, \\ &EI\hat{w}'' + k_{Mt}\hat{w} - k_{Mr}\hat{w}' - D_{0,2} = 0, && x = 0, \\ &-EI\hat{w}''' + k_{Vt}\hat{w} + k_{Vr}\hat{w}' - D_{L,1} + V_r = 0, && x = L, \\ &-EI\hat{w}'' - k_{Mt}\hat{w} - k_{Mr}\hat{w}' + D_{L,2} + M_r = 0, && x = L, \end{aligned} \qquad (3.42)$$

where subscripts V, M stand for shear force and moment, respectively, and t, r for translation and rotation, respectively. Coefficients $D_{0,1}$, $D_{0,2}$, $D_{L,1}$ and $D_{L,2}$ represent the first and second entries in each of the vectors corresponding to the initial conditions. To obtain the specific non-reflective boundaries for the current system, the particular solutions to the specific initial conditions imposed have to be substituted in (3.27) and (3.36). The particular solutions corresponding to the initial conditions based on the eigenfield for left (*Domain 1*) and right (*Domain 3*) domains are the ones in (3.13). The coefficients in front of the displacement and slope are the entries in the dynamic stiffness matrix and they read:

$$k_{Vt} = \left(-1+i\right)k^3 EI, \quad k_{Vr} = ik^2 EI, \quad k_{Mt} = ik^2 EI, \quad k_{Mr} = \left(1+i\right)kEI. \qquad (3.43)$$

Substituting the Laplace domain solution in the boundary conditions and solving the system of four algebraic equations for the four unknown amplitudes, one obtains:

$$B_1 = B_2 = B_3 = B_4 = 0 \qquad (3.44)$$

As obtained in the previous section, the amplitudes of the free waves are zero, meaning that there are no free waves generated by the load entering, exiting or traveling through the finite computational domain. The Laplace domain displacement solution of the computational domain becomes:

$$\hat{w}\left(x,s\right) = -\frac{iF_0}{2EI}\frac{1}{k_1^{\,2} - k_2^{\,2}}\left(\frac{1}{k_1}\frac{1}{s+ik_1v}e^{ik_1x} + \frac{1}{k_2}\frac{1}{s-ik_2v}e^{-ik_2x}\right) - \frac{F_0v^3}{EI}\frac{1}{s^4 - k^4v^4}e^{-s\frac{x}{v}}. \qquad (3.45)$$

Applying the inverse Laplace transform to (3.45), the time domain displacement of the computational domain is obtained. The displacement of the computational domain is exactly the same as the one of *Domain 2* in the previous section, eq. (3.14), therefore its behaviour as visualized in Figure 3.6 is not repeated.

In this section, the semi-infinite domains bounding the computational domain have been replaced by non-reflective boundaries, enabling the analysis to be limited to the computational domain, without the need of also computing the solutions of the two semi-infinite domains. The finite computational domain exhibits exactly the same behaviour as the infinite system. In the next section, the inhomogeneous Winkler stiffness is addressed.

3.3. Inhomogeneous foundation stiffness

As stated in the beginning of this chapter, for the model to be more realistic, a smoothly varying Winkler stiffness must be incorporated. Although analytical methods are available (see Wolfert 1999[1]), they are cumbersome to perform, therefore numerical methods are used for obtaining the solution for the system with smoothly varying Winkler stiffness. To this end, the finite length system that exhibits exactly the same behaviour as the infinite one was derived in the previous sections. The derived finite length system only incorporates a homogeneous Winkler stiffness, therefore, in this section, a smoothly varying stiffness is introduced, and the system is solved using a Finite Difference Method. Firstly, the reason of using a numerical approach is explained. Then, the methodology of the Finite Difference Method is described. Next, it is applied to our system and the solution is computed. Finally, intermediate results are presented. The system to be modeled is visualized in Figure 3.9.

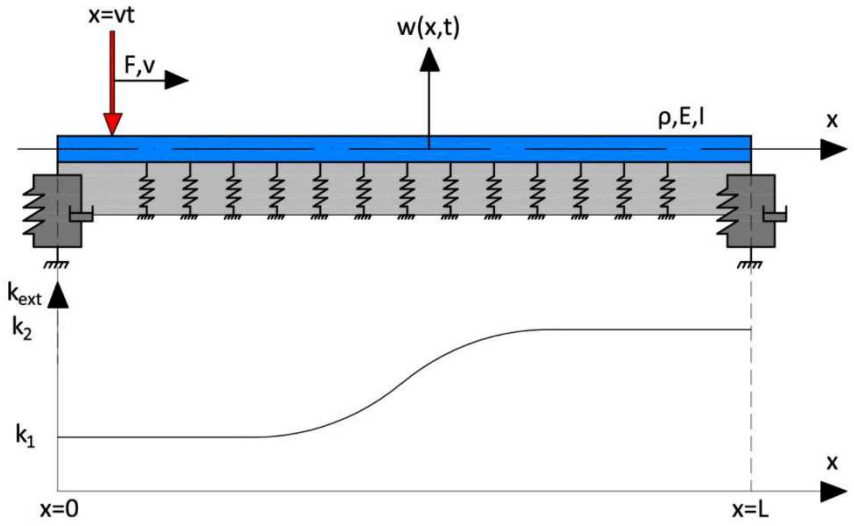

Figure 3.9 - Finite system with smooth Winkler stiffness transition

The equation of motion of this system, in the time domain, reads:

$$w'''' + 4\gamma^2 \ddot{w} + 4\beta^4(x)w = -\frac{F_0}{EI}\delta(x - vt) \tag{3.46}$$

where $\beta(x) = \sqrt[4]{\frac{k_d(x)}{4EI}}$ is the varying stiffness coefficient. This system is linear, therefore the Laplace transform over time can be applied. The equation of motion becomes:

$$\hat{w}'''' + \left[4\gamma^2 s^2 + 4\beta^4(x)\right]\hat{w} = 4\gamma^2\left[sw(t=0) + \dot{w}(t=0)\right] - \frac{F_0}{vEI}e^{-s\frac{x}{v}} \tag{3.47}$$

Due to the varying stiffness coefficient, the solution to the Laplace-domain equation of motion cannot be found under the harmonic wave form as in the previous section. Consequently, the Laplace-domain equation of motion, which is a fourth-order ordinary differential equation, is solved numerically, using a Finite Difference Method.

It is very important to note that imposing the initial state based on the eigenfield to suppress the transient waves due to the load entrance, as done in section 3.1, is also valid for this system, provided that the far most point of the non-zero initial state does not interact with the transition zone, defined in Figure 3.9. Because the eigenfield is derived for the system with homogeneous Winkler stiffness, it only represents the correct initial state for the part of the system with constant stiffness. Moreover, the dynamic stiffness matrices in (3.32) and (3.39) are valid, but the corresponding Winkler stiffness must be adopted in the expression of the wavenumber, namely k_1 for the boundary at $x=0$ and k_2 for the boundary at $x=L$. In the following, a methodology description of the Finite Difference Method is presented.

Finite Difference Methods are numerical methods for solving differential equations by approximating them with difference equations, in which finite differences approximate the derivatives. Therefore, by approximating the fourth-order derivative in (3.47) with difference equations, the fourth-order ordinary differential equation is converted into a system of coupled algebraic equations, which is considerably easier to solve. The finite difference method chosen for this thesis is the central difference, due to its higher accuracy compared to the forward or backward differences. To derive the central difference approximation for the fourth-order derivative of the displacement, the function, displacement in this case, is assumed to behave properly. Then, the spatial domain is discretized in $n-1$ elements of length $L/(n-1)$ connected by n nodes. Next, the Taylor series expansion is performed at node x_0, truncating the expansion after the fourth-order derivative term:

$$w(x)=w(x_0)+\frac{w'(x_0)}{1!}(x-x_0)+\frac{w''(x_0)}{2!}(x-x_0)^2+\frac{w'''(x_0)}{3!}(x-x_0)^3+\frac{w''''(x_0)}{4!}(x-x_0)^4+R_5(x) \tag{3.48}$$

where $R_5(x)$ is the remainder term, denoting the difference between the Taylor polynomial and the original function. Because the central difference approximation of the fourth-order derivative is derived, the Taylor series expansion must be evaluated at the node where the derivative is approximated, x_0, as well as at two nodes on each side of node x_0. The Taylor series expansions evaluated at each of these nodes are weighed by unknown factors and combined into a polynomial, which reads:

$$p=a_1w(x_0-2l)+a_2w(x_0-l)+a_3w(x_0)+a_4w(x_0+l)+a_5w(x_0+2l), \tag{3.49}$$

where a_1,a_2,a_3,a_4,a_5 are the unknown weighing factors and l is the dimension of the discretization. Polynomial p is rearranged, grouping same order derivatives together, thus obtaining:

$$p=f_1w(x_0)+f_2w'(x_0)+f_3w''(x_0)+f_4w'''(x_0)+f_5w''''(x_0), \tag{3.50}$$

where f_1,f_2,f_3,f_4,f_5 are functions of the unknown weighing factors a_1,a_2,a_3,a_4,a_5. Because the fourth-order derivative is sought for, we impose functions $f_1=f_2=f_3=f_4=0$ and $f_5=1$, consequently polynomial p becomes the fourth-order derivative:

$$p=w''''(x_0). \tag{3.51}$$

The system of five algebraic equations composed of $f_1 = f_2 = f_3 = f_4 = 0$ and $f_5 = 1$, is solved for the five unknown weighing factors, thus obtaining:

$$a_1 = 1, \qquad a_2 = -4, \qquad a_3 = 6, \qquad a_4 = -4, \qquad a_5 = 1. \tag{3.52}$$

Replacing the determined weighing coefficients in (3.49) and considering (3.51), the central difference approximation of the fourth-order derivative becomes:

$$w''''(x_0) \approx \frac{w(x_0 - 2l) - 4w(x_0 - l) + 6w(x_0) - 4w(x_0 + l) + 6w(x_0 + 2l)}{l^4}. \tag{3.53}$$

The one challenge encountered using the Finite Difference Method is to incorporate the boundary conditions. The boundary conditions are the same as in the previous section, eq. (3.42). The first, second and third-order derivatives approximation using the central difference are obtained by setting the corresponding functions in (3.50) to one and deriving the weighing factors. Evaluating the approximations of the derivatives using the central difference at the boundaries, results in four nodes lying outside the computational domain, two for *x<0* and two for *x>L*. These nodes are referred to as ghost nodes. From the four boundary conditions, these four ghost nodes are expressed in terms of the nodes inside the computational domain. This way, the boundary conditions are incorporated into the central difference approximation of the fourth-order derivatives of the nodes at the boundaries and the nodes next to the boundaries (inside the computational domain). Writing as well the central difference approximation of the fourth-order derivative for all the nodes inside the computational domain, the stiffness matrix of the beam is obtained.

By applying the central difference approximation to the fourth-order derivative, the Laplace domain equation of motion, eq. (3.47), becomes:

$$\left[K_{i,j} + 4\gamma^2 s^2 I_{i,j} + 4\beta_i^4 I_{i,j}\right]\hat{w}_j = 4\gamma^2\left[s w_i(t=0) + \dot{w}_i(t=0)\right] - \frac{F_0}{vEI} e^{-s\frac{x_i}{v}} + F_{b,i}, \tag{3.54}$$

where $I_{i,j}$ represents the identity matrix, β_i is the discretized Winkler stiffness vector, $\hat{w}_j$ is the discretized Laplace domain displacement vector, $w_i, \dot{w}_i$ are the discretized initial displacement and velocity vectors, respectively, x_i is the discretized spatial coordinate vector, $F_{b,i}$ is the vector containing forces from the applied boundary conditions and $K_{i,j}$ represents the beam stiffness matrix, which reads:

$$K_{i,j} = \frac{1}{l^4}\begin{pmatrix}
K_{1,1} & K_{1,2} & K_{1,3} & 0 & 0 & 0 & \dots & 0 & 0 & 0 & 0 & 0 & 0 \\
K_{2,1} & K_{2,2} & K_{2,3} & 1 & 0 & 0 & \dots & 0 & 0 & 0 & 0 & 0 & 0 \\
1 & -4 & 6 & -4 & 1 & 0 & \dots & 0 & 0 & 0 & 0 & 0 & 0 \\
0 & 1 & -4 & 6 & -4 & 1 & \dots & 0 & 0 & 0 & 0 & 0 & 0 \\
\dots & \dots & \dots & \dots & \dots & \dots & \dots & \dots & \dots & \dots & \dots & \dots & \dots \\
0 & 0 & 0 & 0 & 0 & 0 & \dots & 1 & -4 & 6 & -4 & 1 & 0 \\
0 & 0 & 0 & 0 & 0 & 0 & \dots & 0 & 1 & -4 & 6 & -4 & 1 \\
0 & 0 & 0 & 0 & 0 & 0 & \dots & 0 & 0 & 1 & K_{n-1,n-2} & K_{n-1,n-1} & K_{n-1,n} \\
0 & 0 & 0 & 0 & 0 & 0 & \dots & 0 & 0 & 0 & K_{n,n-2} & K_{n,n-1} & K_{n,n}
\end{pmatrix} \tag{3.55}$$

where $K_{1,1}, K_{1,2}, K_{1,3}, K_{2,1}, K_{2,2}, K_{2,3}, K_{n-1,n-2}, K_{n-1,n-1}, K_{n-1,n}, K_{n,n-2}, K_{n,n-1}$ and $K_{n,n}$ are obtained from the boundary conditions and read:

$$K_{1,1} = K_{n,n} = \frac{12\left(k_{Mr}k_{Vt} - k_{Mt}k_{Vr}\right)l^4 + 36EIk_{Vt}l^3 - 36EI\left(k_{Mt} - \frac{7}{6}k_{Vr}\right)l^2 - 54EIk_{Mr}l - 36EI^2}{EI\left(2k_{Vr}l^2 - 9k_{Mr}l - 21EI\right)},$$

$$K_{2,1} = K_{n-1,n} = \frac{3\left(k_{Mr}k_{Vt} - k_{Mt}k_{Vr}\right)l^4 + 3EIk_{Pt}l^3 + 18EI\left(k_{Mt} - \frac{1}{36}k_{Vr}\right)l^2 + 36EIk_{Mr}l + 39EI^2}{EI\left(2k_{Vr}l^2 - 9k_{Mr}l - 21EI\right)},$$

$$K_{1,2} = K_{n,n-1} = \frac{-48k_{Vr}l^2 + 72k_{Mr}l + 72EI}{2k_{Vr}l^2 - 9k_{Mr}l - 21EI}, \qquad K_{1,3} = K_{n,n-2} = \frac{-48k_{Vr}l^2 + 72k_{Mr}l + 72EI}{2k_{Vr}l^2 - 9k_{Mr}l - 21EI},$$

$$K_{1,2} = K_{n,n-1} = \frac{6k_{Vr}l^2 - 63k_{Mr}l - 99EI}{2k_{Vr}l^2 - 9k_{Mr}l - 21EI}, \qquad K_{2,2} = K_{n-1,n-1} = \frac{-\frac{15}{2}k_{Vr}l^2 + 36k_{Mr}l + 81EI}{2k_{Vr}l^2 - 9k_{Mr}l - 21EI}.$$

(3.56)

It must be noted here, that although the expressions in (3.56) are equivalent for both boundaries (subscript *1, 2, 3* for the left boundary and *n, n-1, n-2* for right boundary), the coefficients $k_{Mr}, k_{Vt}, k_{Mt}, k_{Vr}$ are dependent on the wavenumber according to (3.43). The wavenumber is proportional to k_1 at the left boundary, while proportional to k_2 at the right boundary. Consequently, the values of the coefficients in (3.56) are different at the left boundary compared to the ones at the right boundary. This must be accounted for when assembling the stiffness matrix of the beam.

The coefficients in the boundary conditions, eq. (3.42), which are not proportional to the unknown displacement, namely $D_{0,1}, D_{0,2}, D_{L,1}, D_{L,2}, V_r$ and M_r, are incorporated in the right-hand side of the equation of motion, eq. (3.54), in vector $F_{b,i}$, as follows:

$$F_{B,1} = \frac{12l^2\left(k_{Mr}D_{0,1}l^2 - k_{Vr}D_{0,2}l^2 + 3EID_{0,1}l - 3EID_{0,2}\right)}{EI\left(2k_{Vr}l^2 - 9k_{Mr}l - 21EI\right)},$$

$$F_{B,2} = \frac{3l^2\left(k_{Mr}D_{0,1}l^2 - k_{Vr}D_{0,2}l^2 + EID_{0,1}l + 6EID_{0,2}\right)}{EI\left(2k_{Vr}l^2 - 9k_{Mr}l - 21EI\right)},$$

$$F_{B,n} = \frac{12l^2\left(k_{Vr}\left(M_r + D_{L,2}\right)l^2 - k_{Mr}\left(V_r + D_{L,1}\right)l^2 - 3EI\left(V_r + D_{L,1}\right)l + 3EI\left(M_r + D_{L,2}\right)\right)}{EI\left(2k_{Vr}l^2 - 9k_{Mr}l - 21EI\right)},$$

$$F_{B,n-1} = \frac{3l^2\left(k_{Vr}\left(M_r + D_{L,2}\right)l^2 - k_{Mr}\left(V_r + D_{L,1}\right)l^2 - EI\left(V_r + D_{L,1}\right)_r l - 6EI\left(M_r + D_{L,2}\right)\right)}{EI\left(2k_{Vr}l^2 - 9k_{Mr}l - 21EI\right)}.$$

(3.57)

At this point, it is imperative to note that when the system with inhomogeneous Winkler stiffness is considered, the initial state of the semi-infinite domain at the right of the computational domain is the trivial initial state. The reason behind applying the initial state, as seen in section 3.1, is to suppress the transient waves induced by the load entry. This initial state is chosen based on the eigenfield, which is derived for the homogeneous foundation system. The initial state based on the eigenfield is the correct initial state as long as the length of the computational domain is taken such that it has decayed before it reaches the transition zone, at $t=0$. To exemplify, we consider the infinite system with immediate jump in stiffness, solved in section 2.4. The solution of the infinite system is compared to the eigenfield derived for the Winkler stiffness of the left domain, firstly for the displacement field not yet interacting with the transition and secondly when the two only barely interact, well before the load reaches the inhomogeneity. The two cases are depicted in Figure 3.10.

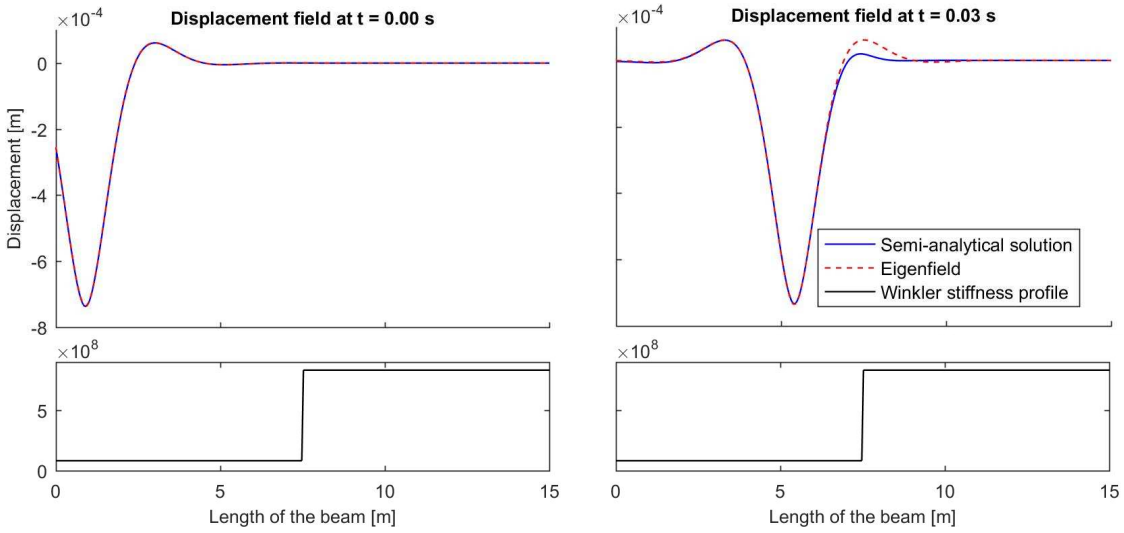

Figure 3.10 – Infinite system with sudden transition in Winkler stiffness. Eigenfield coincides with the response (left) and does not coincide with the response (right)

Comparing the two cases, it can be seen that if the displacement field does not interact with the transition zone, the eigenfield would represent the correct initial state. On the contrary, if the situation depicted in the right plot in Figure 3.10, would represent the moment of load entry, the initial state assumed based on the eigenfield would not be the correct one, leading to transients due to the load entrance.

Therefore, the system with inhomogeneous foundation will only have a non-trivial initial state at the left side of the transition zone, where the load enters. Considering a trivial initial state for the right boundary, the terms in $F_{b,i}$ related to the right boundary become:

$$F_{B,n} = \frac{12l^2\left(k_{Vr}M_r l^2 - k_{Mr}V_r l^2 - 3EIV_r l + 3EIM_r\right)}{EI\left(2k_{Vr}l^2 - 9k_{Mr}l - 21EI\right)},$$
$$F_{B,n-1} = \frac{3l^2\left(k_{Vr}M_r l^2 - k_{Mr}V_r l^2 - EIV_r l - 6EIM_r\right)}{EI\left(2k_{Vr}l^2 - 9k_{Mr}l - 21EI\right)}. \quad (3.58)$$

To obtain the Laplace domain displacement, the matrix formed by adding together, according to eq. (3.54), the beam stiffness matrix, the inertia term diagonal matrix and the Winkler foundation stiffness diagonal matrix, is inverted and both sides of (3.54) are left-multiplied. To obtain the time domain displacement, the inverse Laplace transform is applied numerically. Therefore, the solution to the system with smoothly varying Winkler stiffness has been obtained. To validate the solution, two limit cases are considered. In the first limit case, the solution to the system with homogeneous Winkler foundation is derived using the finite difference method and compared to the eigenfield. The results can be visualized in Figure 3.11.

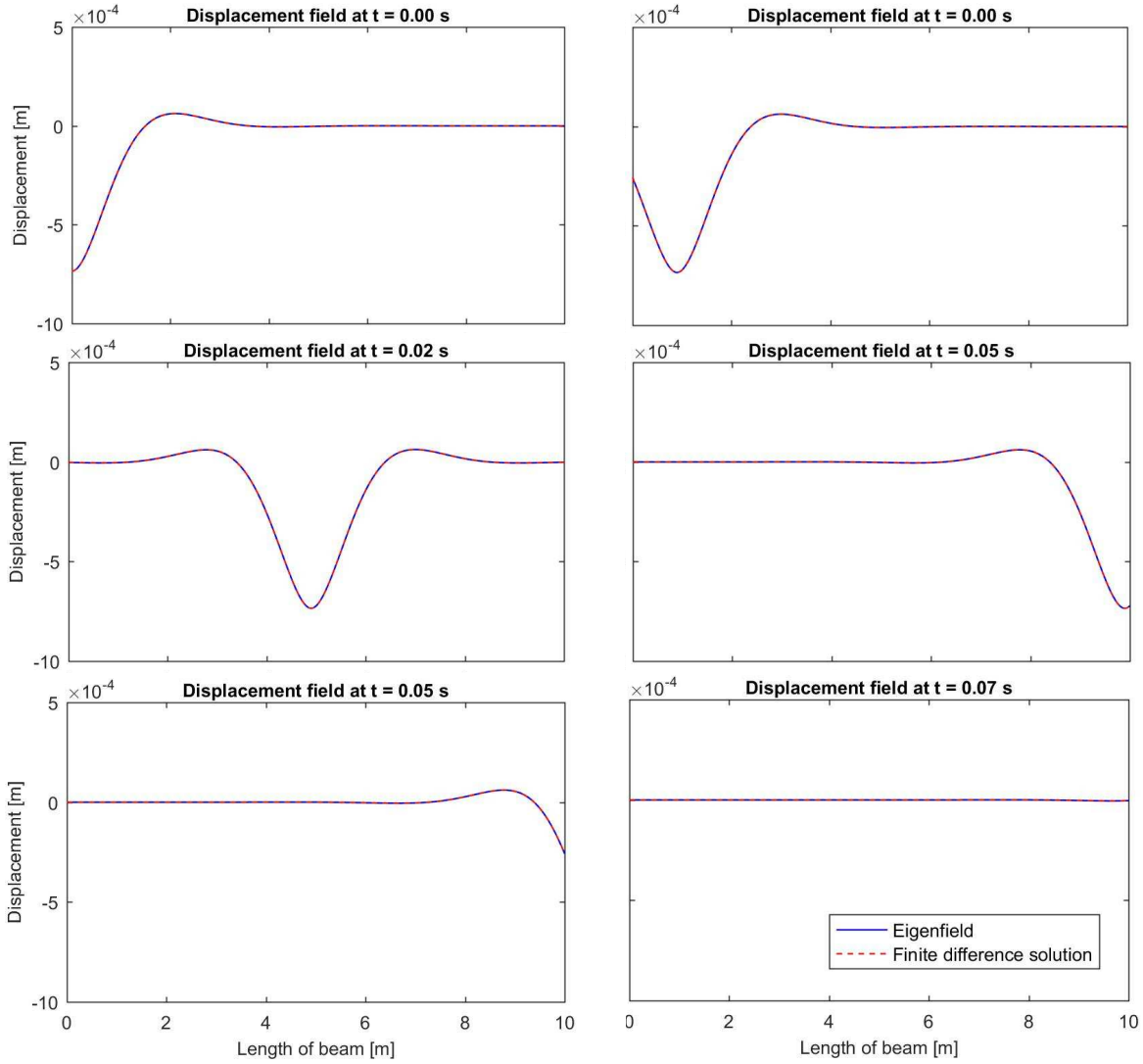

Figure 3.11 – Displacement field of the system with homogeneous Winkler foundation computed by means of finite difference approximation (red line) versus the eigenfield (blue line) at different time moments

The numerical solution, derived by means of the Finite Difference Method, exhibits the same behaviour as the eigenfield, as seen in Figure 3.11. Numerical errors due to the finite different approximation are negligible. Moreover, the non-reflective boundary conditions and the removal of the load forces have been implemented correctly, since no transients are induced by the load entering, neither by the load exiting the computational domain.

In the second limit case, the solution for the system with an abrupt transition in Winkler stiffness is derived using the Finite Difference Method and compared to the semi-analytical solution obtained in section 2.4. The results are visualized in Figure 3.12, where the jump in foundation stiffness lies at $x = 5$ m.

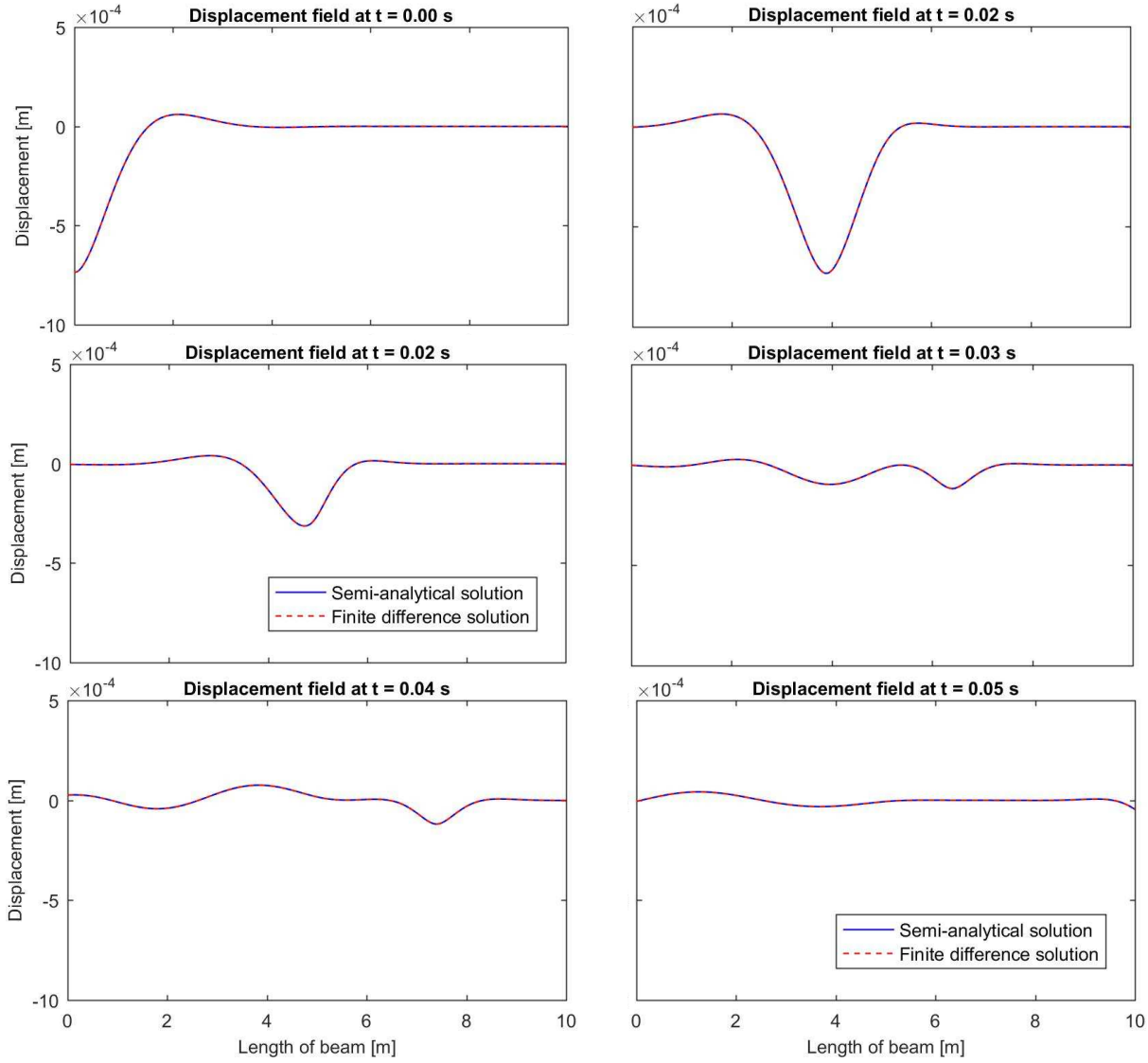

Figure 3.12 – Displacement field of the system with abrupt transition in foundation stiffness derived by means of finite difference approximation (red line) versus the semi-analytical solution (blue line) at different time moments

Once again, the solution derived by means of the Finite Difference Method exhibits the same behaviour as the semi-analytical solution derived in section 2.4.

Considering the results visualized in Figure 3.11 and Figure 3.12, we conclude that the numerical solution possesses a high accuracy when tested in limit cases. In this section, the solution to the system that can incorporate smoothly varying stiffness has been derived by means of the finite difference method. The solution obtained has been validated in the limit cases of homogeneous Winkler stiffness against the eigenfield and sudden jump in stiffness against the semi-analytical solution derived in Chapter 2.4. In the next section, the solution to the system with smoothly varying stiffness is graphically represented for different stiffness profiles and concluding chapter remarks are made.

3.4. Graphical results and concluding remarks of the chapter

In the previous section, the numerical model derived using the Finite Difference Method has been validated in the limit case of homogeneous Winkler foundation against the eigenfield. The numerical model has also been validated in the limit case of a sudden jump in Winkler stiffness against the semi-analytical solution derived in section 2.4. The advantage of the numerical model is that it can incorporate a smooth transition in Winkler stiffness, which corresponds better to reality, where the transition in stiffness develops over a certain length. In this section, the system with smooth Winkler stiffness transition is analyzed graphically.

To understand the influence of the smooth transition in Winkler stiffness, three cases are analyzed, where the length of the transition zone is varied, as follows:

- *Case 1*: $l_{t,1} = 1$ m,
- *Case 2*: $l_{t,2} = 2.5$ m,
- *Case 3*: $l_{t,3} = 20$ m.

The expression used for the Winkler stiffness profile reads:

$$k_{W,n}(x) = \begin{cases} k_1, & x < x_s, \\ k_1 + (k_2 - k_1)\sin^2\left[(x - x_s)\dfrac{\pi}{2l_{t,n}}\right], & x_s < x < x_s + l_{t,n}, \\ k_2, & x > x_s + l_{t,n}, \end{cases}$$

where x_s represents the position where the transition zone starts, $l_{t,n}$ and $k_{W,n}$ represent the transition length and the Winkler stiffness, respectively, for each of the three cases. Of course, the choice of the transition shape, namely a squared sine, is not unique. However, this definition of the stiffness profile ensures completely homogeneous Winkler stiffness up to the transition zone. This matter is important for the accuracy of the initial state chosen based on the eigenfield.

The following parameters are used for the graphical results:

- Winkler stiffness in the soft part: $k_1 = 8.33 \times 10^7$ N/m^2,
- Winkler stiffness in the stiff part: $k_2 = 8.33 \times 10^8$ N/m^2,
- Distributed mass of the beam and slippers: $m = 268$ kg/m,
- Beam bending stiffness: $EI = 6.42 \times 10^6$ N/m^2,
- Constant load amplitude: $F_0 = 8 \times 10^4$ N,
- Load velocity: $v = 350$ m/s.

With the considered velocity of the load of $v = 350$ m/s, it represents 85% of the minimum phase velocity of the waves in the system.

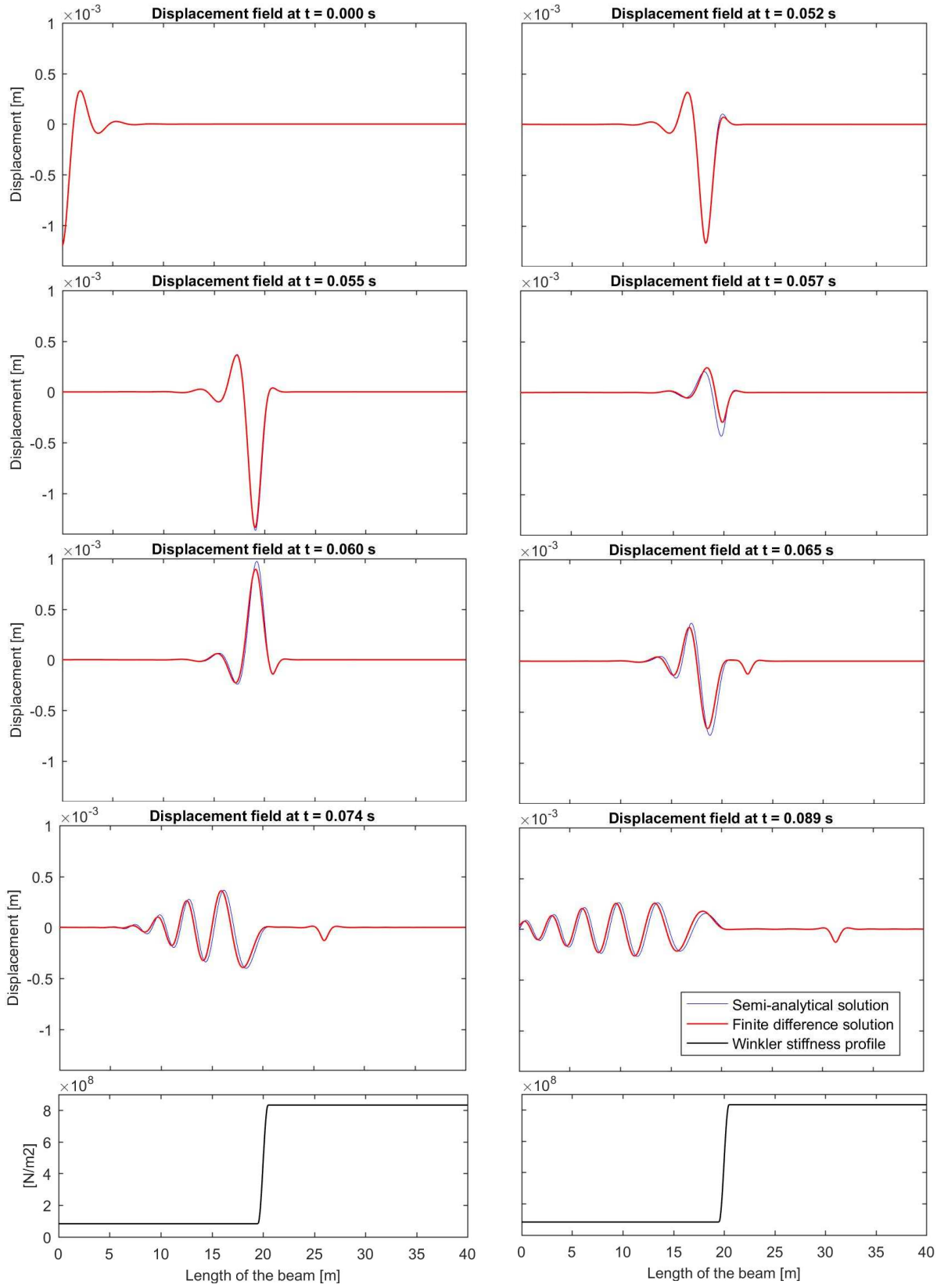

Figure 3.13 – Displacement field of the numerical model for a transition length of 1 m, compared to the displacement field for the sudden jump in stiffness transition

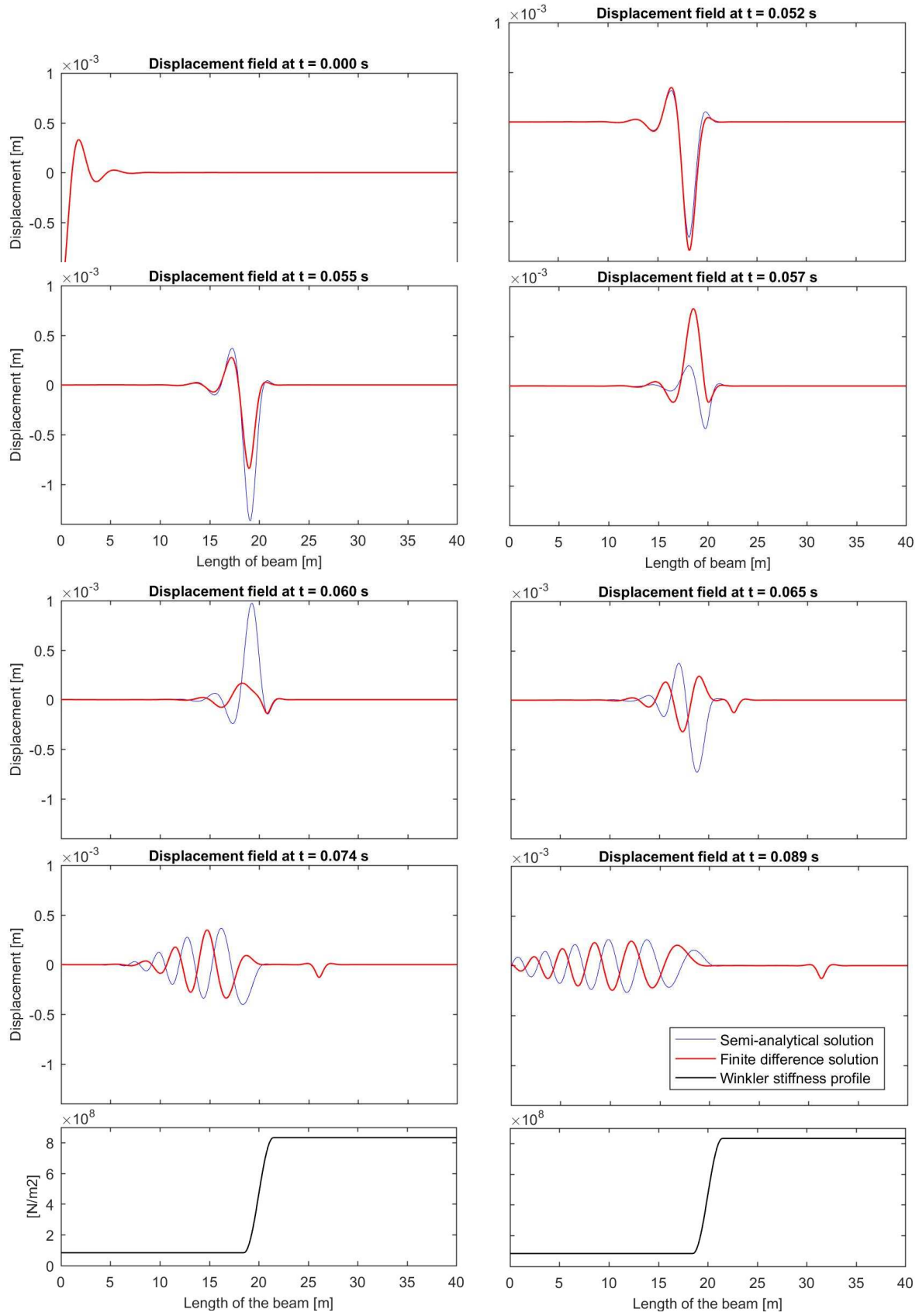

Figure 3.14 - Displacement field of the numerical model for a transition length of 3 m, compared to the displacement field for the sudden jump in stiffness transition

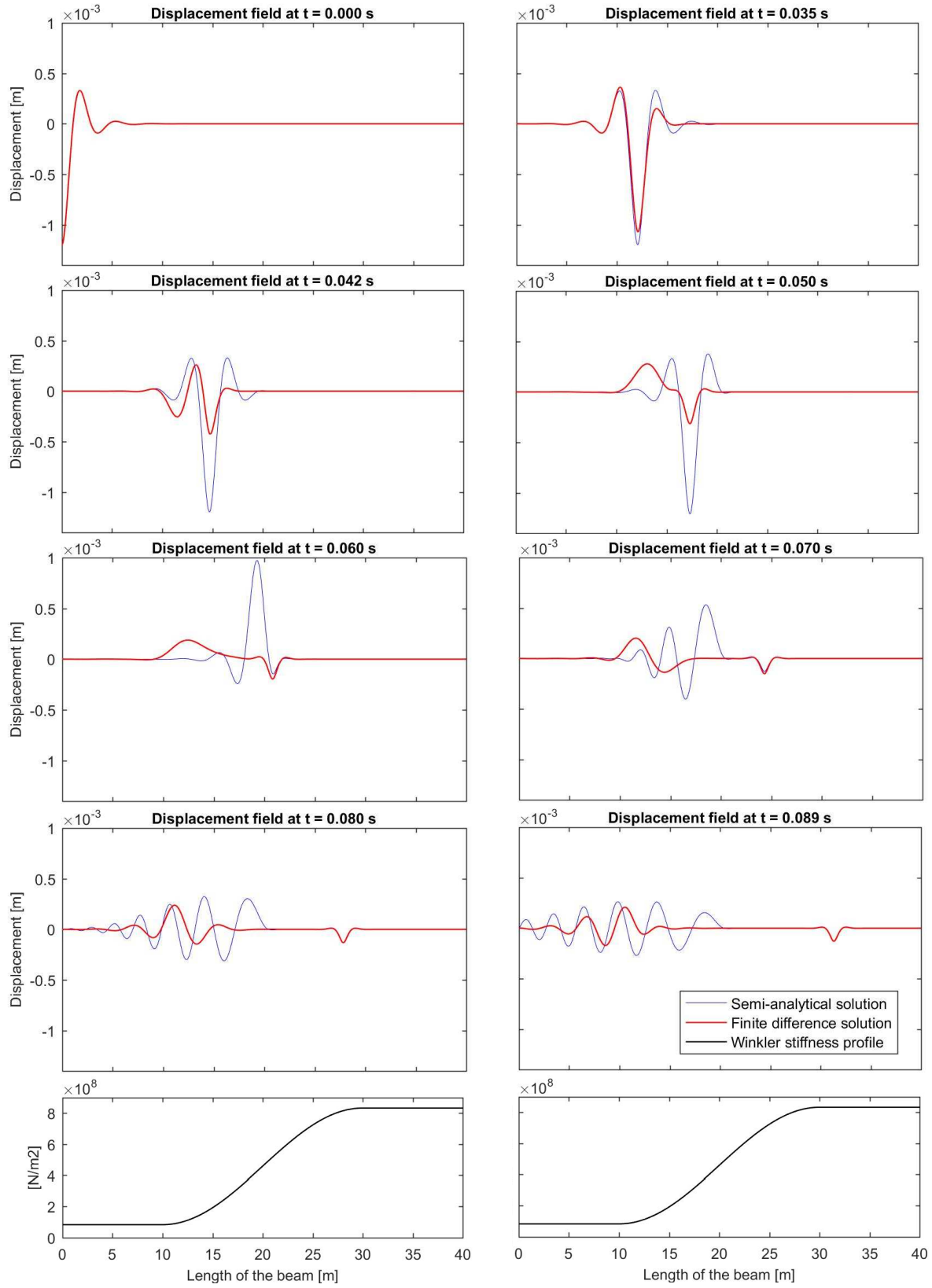

Figure 3.15 - Displacement field of the numerical model for a transition length of 20 m, compared to the displacement field for the sudden jump in stiffness transition

In *case 1*, depicted in Figure 3.13, the two displacement fields are close to one another, because the transition in Winkler stiffness is close to the sudden transition. Although the displacement fields are similar, there are differences. The amplitude of the waves propagating towards the left boundary are slightly smaller than for the sudden transition. Moreover, the free waves of the two solutions are shifted in phase with respect to each other.

In *case 2*, depicted in Figure 3.14, the two displacement fields are significantly different to one another. The difference in amplitude of the free waves is not significantly different from each other. But, the shift exhibited in *case 2* between the two displacement fields is much more pronounced than in *case 1*.

In *case 3*, depicted in Figure 3.15, the behaviour of the two displacement fields is very different. The amplitude of the free waves is comparable at the point where the smooth transition starts, but the decaying character of the solution with smooth transition is much more pronounced. Also, the shift exhibited in *case 3* between the two displacement fields is more pronounced than in *case 1*, but less pronounced than in *case 2*.

The phase shift of the free waves between the case with smooth transition and the abrupt transition depends on the position of the smooth transition starting point relative to the abrupt transition point. Also, as pointed out by van Dalen [2], the amplitude of the free waves generated due to the transition in stiffness is larger in the softer part of the domain.

In this chapter, the solution for the system of a finite beam resting on inhomogeneous Winkler stiffness with a smooth transition profile, subjected to a constant moving load, has been derived. The finite system exhibits the same behaviour as the infinite system, which best represents reality. The solution can be used to analyse the most favorable/unfavorable transition length and profile, such that the damages to the railway track are minimized. In the next chapter, the solution derived in this chapter will also incorporate non-linear Winkler stiffness behavior, to assess the plastic deformations due to transition radiation.

4. Finite system with inhomogeneous and non-linear Winkler stiffness

In delta areas, such as the Netherlands, railway tracks in the vicinity of transition zones require four to eight times more maintenance than the rest of the track. One key factor for this happening is the transition radiation which leads to plastic deformations in the ballast layer. To analyse and predict plastic deformations in the ballast layer, a model must incorporate non-linear foundation stiffness. This leads to the aim of this chapter, which is to incorporate a non-linear Winkler stiffness in the model developed in Chapter 3.

When a system possesses a non-linear behaviour, the principle of superposition cannot be applied to solve for the solution. Several methods are available to solve non-linear systems, among them are iterative schemes performed in the time domain or a mixed time-frequency approach. Considering that the model derived in Chapter 3 uses the frequency approach (i.e. Laplace domain) it comes as a natural step to choose a mixed time-frequency approach to solve the same governing equations, but with non-linear Winkler stiffness. Moreover, mixed time-frequency methods have the potential of being computationally inexpensive compared to the time-domain approaches when considering two-dimensional or three-dimensional systems. The mixed time-frequency approach used in this chapter is based on Hoving [5].

In this chapter, firstly, the mixed time-frequency methodology is described. Then, the described approach is applied to the model derived in Chapter 3. Next, several improvements are made to the frequency spectrum of the Laplace-domain solution, such that the time-domain solution is improved significantly. Finally, the obtained solution is validated for certain limit cases and concluding remarks of the chapter are presented.

4.1. Mixed time-frequency approach methodology

Let us consider the system described in section 3.3, composed of a finite beam resting on inhomogeneous Winkler foundation, but for which instant non-linear events may occur due to the action of the moving load. For the sake of illustration, the system is considered to have trivial initial state at the moment of load entrance, namely $t = 0$. It is safe to assume that the system which is at rest will initially behave linearly, meaning that the entire Winkler stiffness is in the linear regime. Because the system initially behaves linearly, it can be solved in the frequency domain, using the Laplace transform, as done throughout Chapter 3. Solving the system in the said manner, the time-domain displacement is obtained for the entire domain and for all the time moments. This solution is valid until a non-linear event occurs in the system.

A non-linear event occurs when the displacement of any spatial point of the domain exceeds a certain elastic displacement limit, referred to throughout the thesis as w_e. Suppose that such a non-linear event occurs at a given time moment $t = t_0$. Due to the non-linear event occurrence, the properties and behaviour of the system changes, therefore the solution obtained previously is not valid after time t_0. Nevertheless, the changed system will behave linearly until the next non-linear event occurrence, provided that the Winkler-stiffness behaviour is piecewise linear (see Figure 4.1). Therefore, the new

system can be also described and solved in the Laplace domain and the obtained time-domain solution will be valid until the next non-linear event. For the solution before and after the non-linear event occurrence to be continuous, the state of the system at $t = t_0$ is imposed as initial state for the new system. To this end, the time is reset such that the new system starts at $t_2 = 0$, where $t_2 = t - t_0$ for $t \geq t_0$. This new, changed system, with reset time, is solved in the Laplace domain with the corresponding initial state, yielding the time-domain solution between the first and second non-linear events. This procedure is applied each time a non-linear event occurs until the entire time-domain solution is obtained.

In the next section, the described mixed time-frequency method is applied to solve the system analyzed in section 3.3, but for the case of trivial input initial state.

4.2. Finite system with inhomogeneous and non-linear Winkler foundation – solution using mixed time-frequency approach

In this section, the solution to the system composed of a finite beam with non-reflective boundaries and inhomogeneous and non-linear Winkler stiffness is derived using the mixed time-frequency approach. In order to test the method for a large number of non-linear events, the system is chosen to have trivial input initial state. The input initial state refers to the initial state at the global $t = 0$, not to be confused with the initial state at local $t_2 = 0$, used in the mixed time-frequency method. The system with trivial input initial state exhibits larger free vibrations than the system with tuned initial state (compare Figure 3.3 and Figure 3.12), therefore non-linear events are more likely to occur and thus, the method is better validated. It is important to realise that the system with trivial input initial state is used just as a validation for the mixed time-frequency method and does not represent the system aimed to be solved in this chapter. After validating the method, the system with tuned input initial state will be further analyzed.

The system to be solved in this section as well as the non-linear stiffness profile are depicted in Figure 4.1.

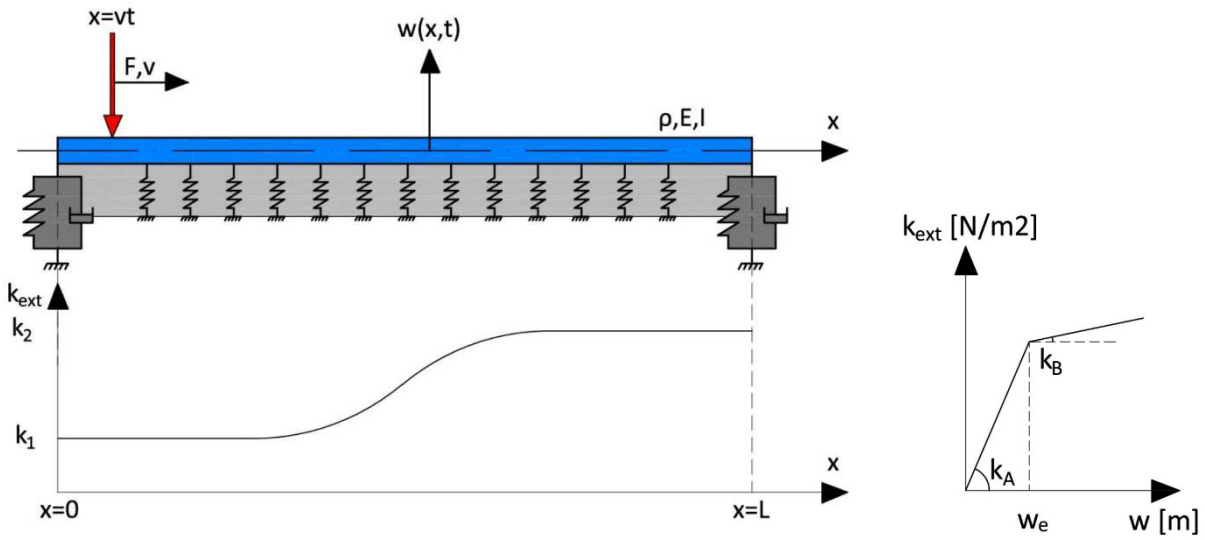

Figure 4.1 - Finite system with inhomogeneous and non-linear Winkler stiffness and trivial input initial state

The system is considered to be at rest at $t = 0$, therefore the behaviour of the Winkler stiffness will initially be linear. Consequently, for the first step of the analysis, the Winkler stiffness has a value of $k_A(x)$ throughout the entire domain, where $k_A(x)$ is the smoothly varying stiffness in the elastic regime. The time-domain equation of motion of the system reads:

$$w'''' + 4\gamma^2 \ddot{w} + 4\beta_A{}^4(x)\, w = \frac{F_0}{EI}\delta(x - vt), \qquad 0 < x < L, \tag{4.1}$$

where $\beta_A = \sqrt[4]{\frac{k_A(x)}{4EI}}$ represents the Winkler stiffness term in the linear regime. Performing the forward Laplace transform for (4.1), considering trivial input initial state and the central difference approximation of the fourth-order derivative, the Laplace-domain equation of motion becomes:

$$\left[K_{i,j} + 4\gamma^2 s^2 I_{i,j} + 4\beta_i{}^4 I_{i,j}\right]\hat{w}_j = -\frac{F_0}{vEI} e^{-s\frac{x_i}{v}} + F_{b,i}, \tag{4.2}$$

where $\beta_i = \sqrt[4]{\frac{k_A(x_i)}{4EI}}$ represents the discretized Winkler stiffness vector and $F_{b,i}$ represents the boundary forcing vector, which in this case, contains only the removal forces due to trivial initial state. The Laplace-domain displacement is obtained by left-multiplying (4.2) with the inverse of the dynamic stiffness matrix. The time-domain displacement is obtained by applying the inverse Laplace transform numerically. The time-domain solution is obtained for the entire computational domain, therefore, a search for a possible non-linear event occurrence must be performed. A non-linear event occurs whenever the displacement of any spatial point in the computational domain exceeds the elastic displacement limit, namely w_e.

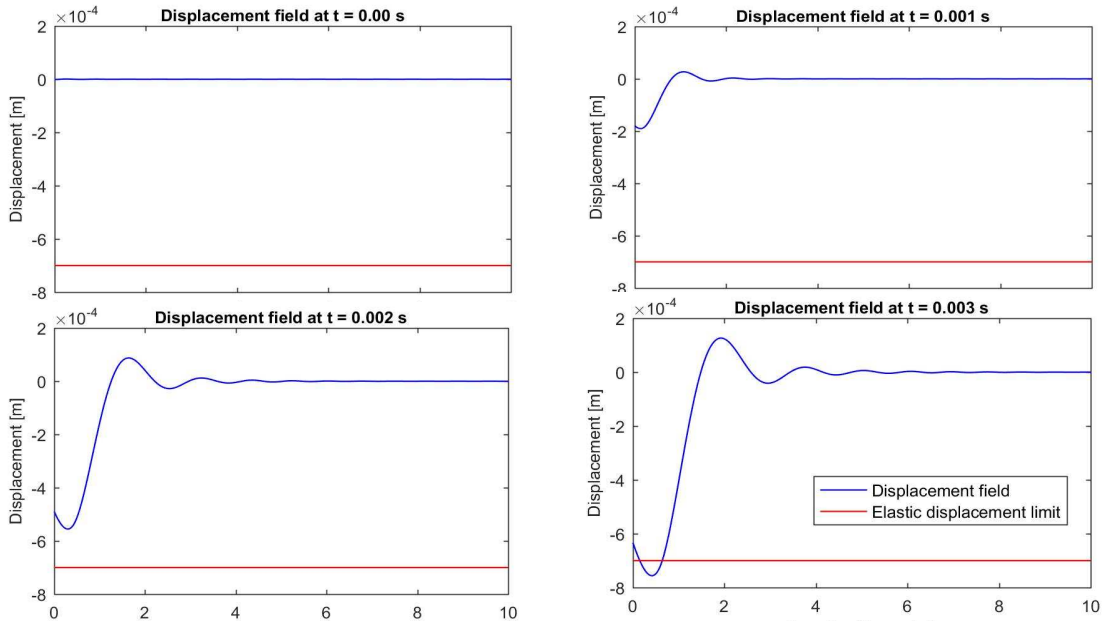

Figure 4.2 - Displacement field of the system with trivial initial conditions for different times moments

In Figure 4.2, the system is at rest at $t = 0$, when the load is entering the domain. The first non-linear event occurs, as seen in the fourth panel of Figure 4.2, at $t = 0.003\,\text{s}$. Therefore, the solution obtained is valid until the occurrence of the non-linear event, thus $t_0 = 0.003\,\text{s}$. The new system is constructed, firstly, performing the variable change in the equation of motion. The new time variable is defined as:

$$t_2 = t - t_0 \qquad <=> \qquad t = t_2 + t_0 . \tag{4.3}$$

Performing the variable change for (4.1), we obtain:

$$w''''\left(x, t_2 + t_0\right) + 4\gamma^2 \ddot{w}\left(x, t_2 + t_0\right) + 4\beta^4\left(x\right) w\left(x, t_2 + t_0\right) = -\frac{F_0}{EI}\delta\left(x - v\left(t_2 + t_0\right)\right). \tag{4.4}$$

A new displacement variable is defined for the new system, namely:

$$w_2\left(x, t_2\right) = w\left(x, t_2 + t_0\right), \qquad t_2 \geq 0 \tag{4.5}$$

The final expression for the time-domain equation of motion becomes:

$$w_2'''' + 4\gamma^2 \ddot{w}_2 + F_W\left(x, t_2\right) = -\frac{F_0}{EI}\delta\left(x - v\left(t_2 + t_0\right)\right), \tag{4.6}$$

where $F_W\left(x, t_2\right)$ represents the force given by the Winkler stiffness and is defined as:

$$F_W\left(x, t_2\right) = \begin{cases} 4\beta_A{}^4 w_2\left(x, t_2\right), & w\left(x, t_0\right) \leq w_e, \\ 4\beta_B{}^4 w_2\left(x, t_2\right) + \underbrace{4\left(\beta_A{}^4 - \beta_B{}^4\right) w_e}, & w\left(x, t_0\right) > w_e, \end{cases} \tag{4.7}$$

Additional constant force

where $\beta_B = \sqrt[4]{\dfrac{k_B\left(x\right)}{4EI}}$ represents the Winkler stiffness in the non-linear regime for the locations where elastic displacement limit is exceeded. The meaning of the additional constant force due to the non-linearity of the Winkler stiffness is graphically represented in Figure 4.3. The first term in the second line of (4.7) assumes that the Winkler stiffness force is proportional to k_B for the entire displacement w_2, therefore it has to be compensated by adding an additional constant force.

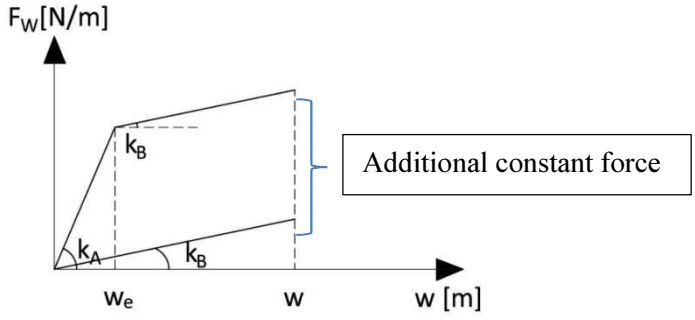

Figure 4.3 - Graphical representation of the additional constant force due to the non-linear regime

The new system exhibits a linear behaviour until the next non-linear event occurrence, thus the Laplace transform is applied to the equation of motion, with respect to the new time variable, t_2 , obtaining:

$$\left[K_{i,j}+4\gamma^2 s^2 I_{i,j}+4\beta_i^4 I_{i,j}\right]\hat{w}_{2,j}=-\frac{F_0}{vEI}e^{-s\left(\frac{x_i}{v}-t_0\right)}H\left(\frac{x_i}{v}-t_0\right)+\frac{F_{NL,i}}{s}+F_{IC,i}+F_{b,i}, \qquad (4.8)$$

where β_i is the discretized Winkler stiffness vector containing only the term in (4.7) proportional to w_2, $\hat{w}_{2,i}$ is the discretized Laplace-domain displacement vector of the new system, $H\left(\frac{x_i}{v}-t_0\right)$ represents the Heaviside function, $F_{NL,i}$ is the discretized additional constant forcing in (4.7), $F_{b,i}$ represents the boundary forces vector containing the initial state influence at the non-reflective boundaries as well as the removal forces, and $F_{IC,i}$ represents the discretized initial state vector which reads:

$$F_{IC,i}=4\gamma^2\left[sw_{1,i}\left(t=t_0\right)+\dot{w}_{1,i}\left(t=t_0\right)\right], \qquad (4.9)$$

where $w_{1,i}$, $\dot{w}_{1,i}$ represent the initial displacement and velocity of the previous system at the time of the non-linear event, $t=t_0$. In (4.8), all terms are known, except for the boundary forces vector. This vector is obtained after applying the boundary conditions using the finite difference method, described in section 3.3, and has nonzero entries only for the first, second, last and last but one nodes. The entries read:

$$F_{B,1}=\frac{12l^2\left(k_{Mr}D_{0,1}l^2-k_{Vr}D_{0,2}l^2+3EID_{0,1}l-3EID_{0,2}\right)}{EI\left(2k_{Vr}l^2-9k_{Mr}l-21EI\right)},$$

$$F_{B,2}=\frac{3l^2\left(k_{Mr}D_{0,1}l^2-k_{Vr}D_{0,2}l^2+EID_{0,1}l+6EID_{0,2}\right)}{EI\left(2k_{Vr}l^2-9k_{Mr}l-21EI\right)},$$

$$F_{B,n}=\frac{12l^2\left(k_{Vr}\left(M_r+D_{L,2}\right)l^2-k_{Mr}\left(V_r+D_{L,1}\right)l^2-3EI\left(V_r+D_{L,1}\right)l+3EI\left(M_r+D_{L,2}\right)\right)}{EI\left(2k_{Vr}l^2-9k_{Mr}l-21EI\right)},$$

$$F_{B,n-1}=\frac{3l^2\left(k_{Vr}\left(M_r+D_{L,2}\right)l^2-k_{Mr}\left(V_r+D_{L,1}\right)l^2-EI\left(V_r+D_{L,1}\right)_r l-6EI\left(M_r+D_{L,2}\right)\right)}{EI\left(2k_{Vr}l^2-9k_{Mr}l-21EI\right)},$$

(4.10)

where $F_{B,1}$, $F_{B,2}$, $F_{B,n}$ and $F_{B,n-1}$ are the first, second, last and last but one entries, respectively. All quantities are known, except for the vectors D_0 and D_L . As described in Chapter 3.2, the non-reflective boundaries represent the reaction of two semi-infinite systems, one to the left of the computational domain and one to the right, in such a way that the finite computational domain exhibits the same behaviour as an infinite system. Vectors D_0 and D_L represent the influence of the initial state of these

semi-infinite systems at the interface with the computational domain. The expressions for D_0 and D_L are known and given by (3.33) and (3.39), but the particular solutions due to initial state of the semi-infinite domains are not yet known. The particular solutions found in Chapter 3.1, correspond to the initial state chosen based on the eigenfield. However, for the current system, the state of the semi-infinite domains at $t = t_0$, is arbitrary. Therefore, firstly the state of the semi-infinite domains has to be found at $t = t_0$ and then the particular solution related to the obtained state must be determined.

4.2.1. Determine the state of the semi – infinite domains at $t=t_0$

One should realize that there is no force acting on the semi-infinite domains, such that the only external forcing comes from the interface with the computational domain. Consequently, to find the displacement and velocity fields of the semi-infinite domain at $t = t_0$, the solution of the system has to be derived for imposed displacement and slope at the interface with the computational domain. Firstly, the procedure is performed for the semi-infinite domain at the left of the computational domain, and then a concise derivation for the domain on the right is performed. The system for which the solution is derived is depicted in Figure 4.4.

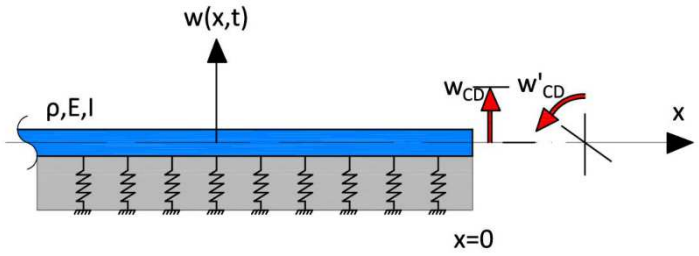

Figure 4.4 – Left semi–infinite domain with imposed displacement and slope at the interface with the computational domain

The time-domain equation of motion and the boundary conditions for the system depicted in Figure 4.4, respectively, read:

$$w_L'''' + 4\gamma^2 \ddot{w}_L + 4\beta^4 w_L = 0\,, \qquad x < 0\,,$$

$$w_L(0,t) = w_{CD}(0,t)\,,$$

$$w_L'(0,t) = w_{CD}'(0,t)\,, \qquad (4.11)$$

where w_L is the displacement of the left semi-infinite domain, and w_{CD}, w_{CD}' are the displacement and slope of the computational domain. Applying the forward Laplace transform to (4.11), one obtains:

$$\hat{w}_L'''' - k^4 \hat{w}_L = 4\gamma^2 \left[s w_L(x,0) + \dot{w}_L(x,0) \right], \qquad x < 0\,,$$

$$\hat{w}_L(0,s) = \hat{w}_{CD}(0,s)\,,$$

$$\hat{w}_L'(0,s) = \hat{w}_{CD}'(0,s)\,. \qquad (4.12)$$

The current system for which the solution is derived, depicted in Figure 4.1, has trivial input initial state, therefore the input initial state for the semi-infinite domain to the left should also be trivial. However, to solve the system with tuned input initial state, performed in Chapter 4.4, the left semi-infinite domain has to account also for non-trivial input initial state, therefore the derivation is performed using a particular solution corresponding to the tuned input initial state. At the end of the derivation, the particular solution will be set to zero to account for the trivial input initial state, for the system discussed in this section.

The Laplace-domain solution to the equation of motion in (4.12) reads:

$$\hat{w}_L\left(x,s\right)=A_1e^{ikx}+A_2e^{kx}+\hat{w}_{L,in,p}\,,\qquad x<0\,,\tag{4.13}$$

where $\hat{w}_{L,in,p}$ represents the particular solution corresponding to the tuned input initial state. Substituting (4.13) in the boundary conditions of (4.12) and solving the system of two algebraic equations for the two unknowns, A_1 and A_2, one obtains the Laplace-domain solution for the left semi-infinite domain:

$$\hat{w}_L\left(x,s\right)=\frac{1+i}{2k}\left[k\hat{w}_{CD}\left(0,s\right)-\hat{w}'_{CD}\left(0,s\right)-k\hat{w}_{L,in,p}\left(0,s\right)+\hat{w}'_{L,in,p}\left(0,s\right)\right]e^{ikx}+$$

$$+\frac{1}{2k}\left[\left(1-i\right)k\hat{w}_{CD}\left(0,s\right)+\left(1+i\right)\hat{w}'_{CD}\left(0,s\right)+\left(1-i\right)k\hat{w}_{L,in,p}\left(0,s\right)-\left(1+i\right)\hat{w}'_{L,in,p}\left(0,s\right)\right]e^{kx}+\hat{w}_{L,in,p}\left(x,s\right).\tag{4.14}$$

To find the time-domain displacement of the semi-infinite domain, one has to perform the inverse Laplace transform of (4.14). To find the time-domain velocity of the semi-infinite domain at $t=t_0$, one has to perform the inverse Laplace transform of the Laplace-domain velocity expression, which is defined as:

$$\dot{w}_L\left(x,t\right)=\frac{e^{\sigma t}}{\pi}\int_0^{\omega_{\max}}\underbrace{\left(s\hat{w}_L-w_L\left(t=0\right)\right)}_{\text{Laplace-domain velocity}}e^{i\omega t}d\omega\,.\tag{4.15}$$

Evaluating the time-domain displacement and velocity at $t=t_0$, the state of the left semi-infinite domain at $t=t_0$ is obtained. To obtain the state of the right semi-infinite domain, one has to keep in mind that it will always have trivial input initial state. The reason behind the input initial state is to suppress the transient waves induced by the load entry. This input initial state is chosen based on the eigenfield, which is derived for the homogeneous foundation system, as discussed in section 3.1. Therefore, the system with inhomogeneous foundation will only have an input initial state at the left side of the transition, where the load enters. This is more thoroughly explained in section 3.3.

Following the same procedure for the right semi-infinite domain, and considering trivial initial state, the Laplace domain displacement is:

$$\hat{w}_3(x,s)=\frac{1+i}{2k}\left[k\hat{w}_{CD}(L,s)+\hat{w}'_{CD}(L,s)\right]e^{-ik(x-L)}+\frac{1}{2k}\left[(1-i)k\hat{w}_{CD}(L,s)-(1+i)\hat{w}'_{CD}(L,s)\right]e^{-k(x-L)}. \tag{4.16}$$

Applying the inverse Laplace transform to the Laplace-domain displacement and velocity of the right semi-infinite domain and evaluating the resulting time-domain displacement and velocity at $t=t_0$, the state of the right semi-infinite domain at $t=t_0$ is obtained. In the next section, the particular solutions for the obtained states of the semi-infinite domains, at $t=t_0$, are obtained, with which vectors D_0 and D_L are fully determined.

4.2.2. Deriving the particular solution due to a generalized initial state

The states of the semi-infinite domains at the moment of non-linearity occurrence, $t=t_0$, have been derived and will be applied as initial states for the boundary conditions of the new system. The response of the semi-infinite domains at the boundary has been derived in section 3.2, the only unknowns still to be found are the particular solutions corresponding to the initial states of the semi-infinite domains.

The states of the semi-infinite domains at the non-linear event, $t=t_0$, derived in section 4.2.1, are only known numerically. This is due to the application of the inverse Laplace transform numerically. As a restul, the particular solutions cannot be sought for as done previously, in Chapter 3. Therefore, another method of finding the particular solution is employed, namely the Green's function approach. The Green's function of a system is the response of the system to an impulse force. The Laplace-domain equation of motion of the left semi-infinite domain reads:

$$\hat{w}_L''''-k^4\hat{w}_L=4\gamma^2\left[sw_L(x,t_0)+\dot{w}_L(x,t_0)\right], \qquad x<0, \tag{4.17}$$

where $w_L(x,t_0)$ and $\dot{w}_L(x,t_0)$ are the displacement and velocity of the left semi-infinite domain at $t=t_0$, obtained in section 4.2.1. To find the Green's function of the left semi-infinite domain, the initial state force is replaced by an impulse force, thus obtaining:

$$\hat{w}_L''''-k^4\hat{w}_L=1\cdot\delta(x-\xi), \qquad x<0, \tag{4.18}$$

where ξ is the point of impulse application. Solving (4.18) for the displacement, the Green's function is obtained:

$$\hat{g}(x,\xi,s)=\frac{1}{4}\frac{1}{k^3}\left(-ie^{-ik|x-\xi|}-e^{-k|x-\xi|}\right), \tag{4.19}$$

where $\hat{w}$ has been replaced with $\hat{g}$, which denotes the Green's function.

The particular solution for the general initial state is obtained by means of a convolution integral of the initial state and the Green's function, as follows:

$$\hat{w}_{L,p}(x,s) = 4\gamma^2 \int_{-\infty}^{0} \hat{g}(x,\xi,s)\left(sw_L(\xi,t_0) + \dot{w}_L(\xi,t_0)\right)d\xi \,. \tag{4.20}$$

Once again, because the initial conditions are only known numerically, the convolution integral is also performed numerically. Following the same procedure for the right semi-infinite domain, one obtains:

$$\hat{w}_{R,p}(x,s) = 4\gamma^2 \int_{L}^{\infty} \hat{g}(x,\xi,s)\left(sw_R(\xi,t_0) + \dot{w}_R(\xi,t_0)\right)d\xi \,. \tag{4.21}$$

To improve accuracy and reduce computational time, the spatial derivation of the particular solution required in vectors D_0 and D_L according to (3.33) and (3.39), is performed analytically. The limits of integration in eq. (4.20) and (4.21) are not space dependent, thus, according to Leibniz rule, the order of integration and derivation can be interchanged. Because the only x dependent term in (4.20) and (4.21) is the Green's function, taking the derivatives comes down to taking the derivatives of the Green's function. The derivatives, therefore, become:

$$\begin{aligned}
\hat{w}'_{L,p}(0,s) &= 4\gamma^2 \int_{-x_{\max}}^{0} \hat{g}'(0,\xi,s)\left(sw_L(\xi,t_0) + \dot{w}_L(\xi,t_0)\right)d\xi \,, \\
\hat{w}''_{L,p}(0,s) &= 4\gamma^2 \int_{-x_{\max}}^{0} \hat{g}''(0,\xi,s)\left(sw_L(\xi,t_0) + \dot{w}_L(\xi,t_0)\right)d\xi \,, \\
\hat{w}'''_{L,p}(0,s) &= 4\gamma^2 \int_{-x_{\max}}^{0} \hat{g}'''(0,\xi,s)\left(sw_L(\xi,t_0) + \dot{w}_L(\xi,t_0)\right)d\xi \,,
\end{aligned} \tag{4.22}$$

where the lower boundary has been replaced by $x_{\max}$, which is the position of the wave-front, defined in our case as:

$$x_{\max} = c_{gr,\max} \cdot t_0 \,, \tag{4.23}$$

where $c_{gr,\max}$ is the maximum group velocity of the waves in the system, defined as:

$$c_{gr,\max} = 2\sqrt{\frac{EI}{\rho}}k \,, \tag{4.24}$$

where k is the wavenumber. The truncation of the integration over spatial domain is chosen based on the position of the wave-front, because beyond it the system is at rest, therefore not having a contribution to the particular solution.

The derivatives of the particular solution for the right semi-infinite domain read:

$$\hat{w}'_{R,p}(L,s) = 4\gamma^2 \int_L^{x_{\max}-L} \hat{g}'(L,\xi,s)\left(sw_R(\xi,t_0) + \dot{w}_R(\xi,t_0)\right)d\xi ,$$

$$\hat{w}''_{R,p}(L,s) = 4\gamma^2 \int_L^{x_{\max}-L} \hat{g}''(L,\xi,s)\left(sw_R(\xi,t_0) + \dot{w}_R(\xi,t_0)\right)d\xi ,$$

$$\hat{w}'''_{R,p}(L,s) = 4\gamma^2 \int_L^{x_{\max}-L} \hat{g}'''(L,\xi,s)\left(sw_R(\xi,t_0) + \dot{w}_R(\xi,t_0)\right)d\xi . \qquad (4.25)$$

With the obtained particular solutions of the semi-infinite domains and their spatial derivatives, the vectors corresponding to the initial states of the semi-infinite domains, D_0 and D_L, are fully determined. Consequently, $F_{b,i}$ in eq. (4.8), representing the boundary forces vector containing the initial state at the non-reflective boundaries as well as the removal forces, is fully determined.

Now, the Laplace-domain displacement for the new system can be obtained. Eq. (4.8) is multiplied at the left by the inverse of the dynamic stiffness matrix, therefore obtaining the Laplace-domain displacement for the new system. Applying the inverse Laplace transform to the Laplace-domain displacement of the new system, the time-domain displacement is obtained. The process of searching for the next non-linear event occurrence is now performed again. The entire process is repeated until the entire time-domain solution is obtained.

The solution of the system with inhomogeneous and non-linear Winkler stiffness has therefore been computed. To validate the solution, it is tested in the linear limit case ($k_A = k_B$), implying that although the solution is found using the mixed-time frequency approach, the behaviour of the system is linear. To have an accurate benchmark solution, the Winkler stiffness is considered to be homogeneous, for which the semi-analytical solution has been derived in Chapter 3.1, eq. (3.7) with coefficients in (3.8). The graphical results are presented in Figure 4.5.

From Figure 4.5, it can be concluded that the solution obtained by means of the mixed time-frequency approach is not satisfactory, exhibiting significant error compared to the benchmark solution. The main source of error comes from the application of the inverse Laplace transform numerically several times. As stated in Chapter 3.1, by using the cosine alternative expression for the inverse Laplace transform, the velocity exhibited by the solution close to $t = 0$ is considerably smaller than the initial velocity imposed. Usually, the initial velocity does not have a major impact on the solution, as seen throughout Chapter 3. However, in this case, because the non-linear events occur close to one another, the error accumulates, leading to the erroneous results seen in Figure 4.5. To obtain a more accurate solution, several improvements will be made to the Laplace-domain solution's frequency spectrum as well as a higher-order finite difference approximation will be employed, in the next section.

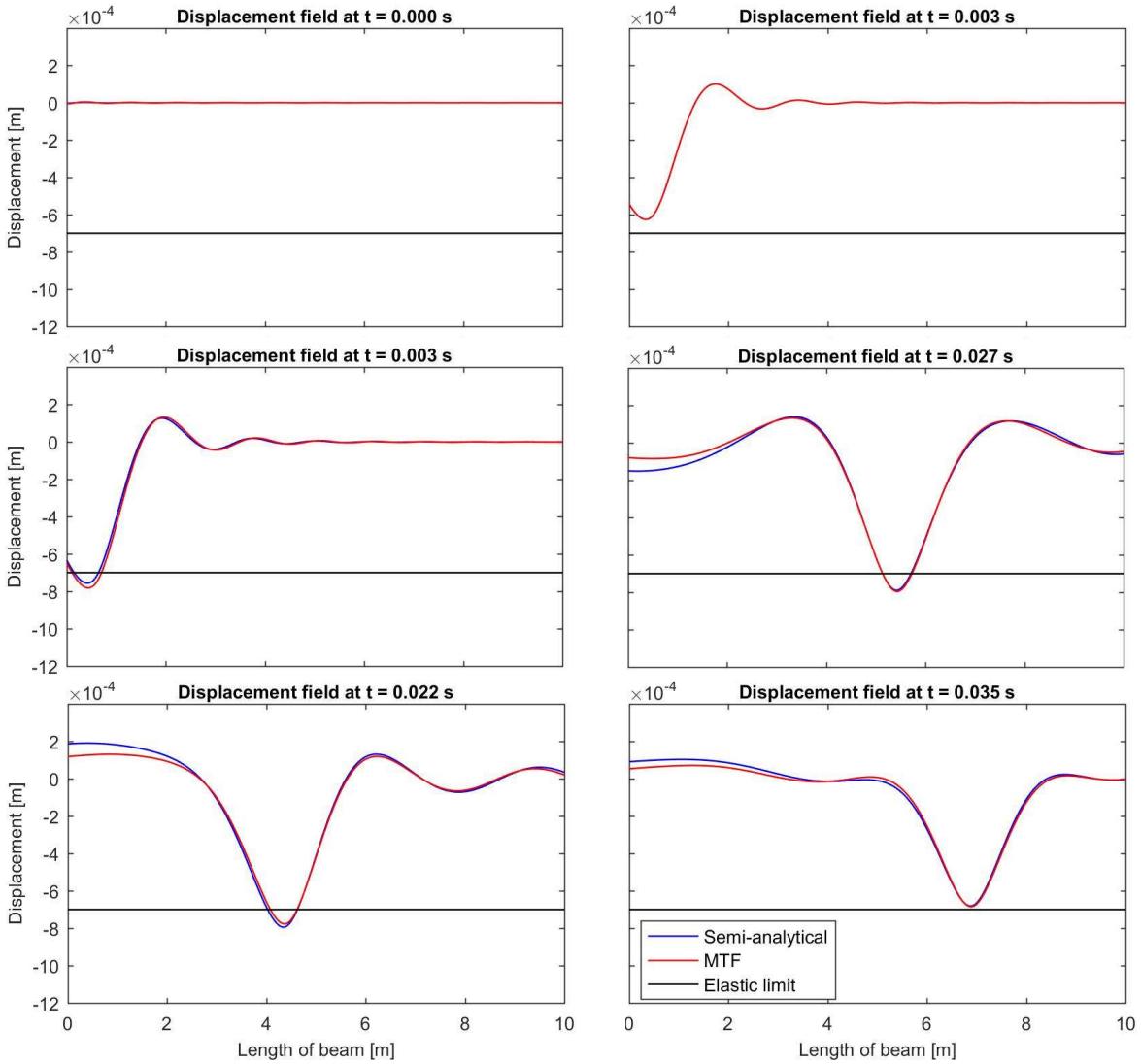

Figure 4.5 – Displacement field obtained by means of mixed time-frequency approach in the linear limit case (k_A=k_B) with homogeneous stiffness compared to the semi-analytical solution obtained in section 3.1 for the system with trivial input initial state

In this section, the solution of the system with inhomogeneous and non-linear Winkler stiffness with trivial input initial state has been found using the mixed time-frequency approach. Firstly, the entire system has been solved assuming linear behaviour. Then, the first non-linear event occurrence has been determined. The time was reset, and the new system was derived, imposing as initial state, the state of the previous system at the time of the non-linear event occurrence. Next, the updated non-reflective boundaries have been determined. Finally, after applying the procedure several times, the entire time-domain solution has been obtained. The solution appeared not satisfactory when tested in the limit case, therefore, in the next section, several improvements are made to the model, such that the error becomes negligible.

4.3. Improvement of the solution for the mixed time-frequency method

As seen in the previous section, the solution obtained using the mixed time-frequency method is not satisfactory when tested in the limit case. The main source of the error is the application of the inverse Laplace transform numerically several times. Another source of error comes from the finite difference approximation. In this section, the frequency spectrum of the Laplace-domain solution is analyzed, especially the behaviour at high frequencies. Then, to obtain more accurate time-domain solutions at and close to $t_2 = 0$, the decay of the frequency spectrum is improved. Also, a higher order finite difference approximation is employed. Finally, the improved time-domain solution is graphically represented and validated in the elastic limit case. For the sake of illustration, the homogeneous Winkler stiffness is chosen for this derivation.

4.3.1. Improvement of the frequency-spectra decay

For the first step of the analysis using the mixed time-frequency method, when the system is at rest at global time $t = 0$, the Laplace-domain displacement is described by the following expression:

$$\mathbf{w} = \mathrm{K_{dyn}}^{-1}\mathbf{F}, \tag{4.26}$$

where $F_i = -\dfrac{F_0}{vEI} e^{-s\frac{x_i}{v}} + F_{b,i}$.

In Figure 4.6, the frequency spectra of the first and last nodes are graphically represented. The frequency spectra exhibit a good decay, therefore the frequency truncation in the inverse Laplace transform does not introduce significant error.

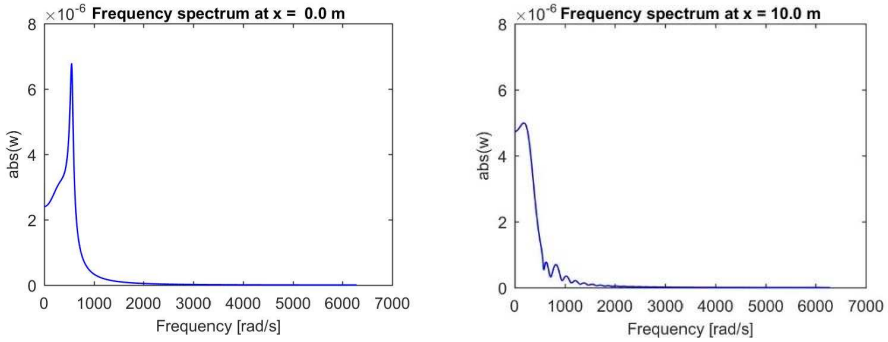

Figure 4.6 – Frequency spectra for the first step of the mixed time-frequency analysis, at the first and last nodes, for the system with trivial input initial state

For the second step of the mixed time-frequency analysis, after the first non-linear event has been found, the system is reset and the state of the previous system at $t = t_0$ is applied as initial state for the new system, the Laplace-domain displacement reads:

$$\mathbf{w_2} = \mathrm{K_{dyn}}^{-1}\mathbf{F}, \tag{4.27}$$

where $F_i = -\dfrac{F_0}{vEI} e^{-s\left(\frac{x_i}{v} - t_0\right)} H\left(\dfrac{x_i}{v} - t_0\right) + \dfrac{F_{NL,i}}{s} + F_{IC,i} + F_{b,i}$.

In Figure 4.7, the frequency spectra of the first and last nodes as well as at the position of the load, are graphically represented. The frequency spectra of the first node and at the position of the load exhibit a poor decay, therefore the frequency truncation in the inverse Laplace transform introduces significant error in the result. The frequency spectrum of the last node exhibits a very similar character as the one in Figure 4.6.

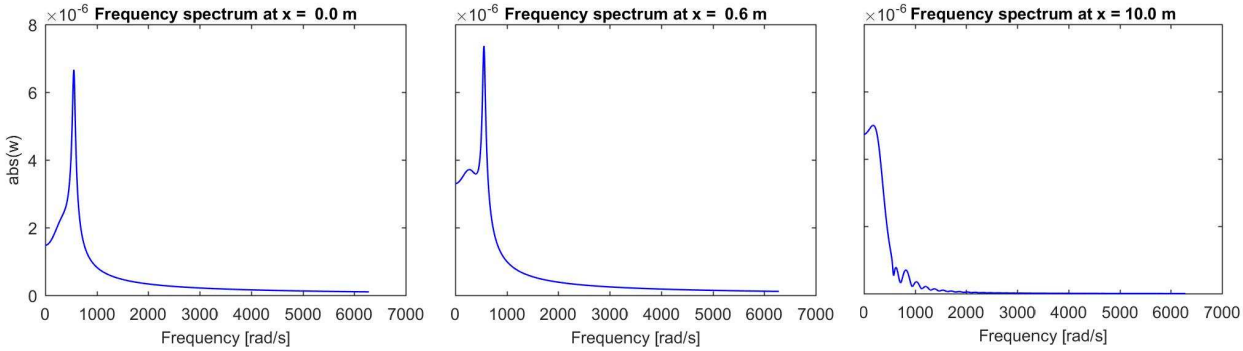

Figure 4.7 – Displacement frequency spectra for the second step of the mixed time-frequency analysis, at the first and last nodes, as well as at the position of the load (middle), for the system with trivial input initial state

To improve the decay of the frequency spectra, first, the cause of this poor decay must be determined. The cause can be found by analyzing **Error! Reference source not found.** in the high frequency regime and finding the dominating term at high frequencies. From the dynamic stiffness matrix which lies in the denominator, the inertia term is proportional to s^2, the Winkler stiffness does not depend on frequency, while the beam stiffness matrix only depends on frequency at the boundaries. Considering (3.56), we observe that the dominant coefficients are $K_{1,1}, K_{n,n}, K_{2,1}, K_{n-1,n}$ in which the dominant terms are the products $k_{Mr}k_{Pt}/k_{\mathrm{Pr}}$. Considering (3.43), we conclude that these terms are proportional to the squared wavenumber, meaning that they are proportional to s, therefore the inertia term is the dominant term in the denominator. Now, we analyze the numerator terms. The moving load term, decays exponentially and at the point of the load, where the exponential reduces to unity, it is constant. Therefore, when considering the denominator, it will decay with s^{-2}. The non-linear forcing term, also considering the denominator, decays with s^{-3}. The boundary forcing vector is harder to analyze at high frequency. Analyzing (4.10), the boundary forcing vector $F_{b,i}$ is proportional to D_0 and D_L. These vectors, are in turn proportional to: $k^3\hat{w}_p, k^2\hat{w}_p', k\hat{w}_p'', \hat{w}_p'''$. Considering (4.22), we conclude that these terms have a decay proportional to $sw_1(0,t=0)$ at the left boundary and $sw_3(L,t=0)$ at the right boundary, therefore when considering the denominator as well, the boundary forcing vector $F_{b,i}$ exhibits a decay proportional to s^{-1}. The initial state vector, $F_{IC,i}$, also exhibits a decay proportional to s^{-1}, when also considering the denominator.

Consequently, the behaviour of the Laplace-domain displacement in the high-frequency regime, is dominated by the initial displacement applied:

$$\lim_{s\to\infty}\hat{w}_{2,i}=\frac{w_2(x_i,t_2=0)}{s} \tag{4.28}$$

Throughout the thesis, (4.28) is referred to as the high-frequency approximation.

In Figure 4.8, the high-frequency approximation is graphically represented against the Laplace-domain displacement. The two frequency spectra have the same behaviour in the high-frequency regime, confirming (4.28). The reason why the frequency spectrum of the last node has a similar behaviour as the one in Figure 4.6 is because the initial displacement applied at the last node is very small, as can be seen in the last plot of Figure 4.2.

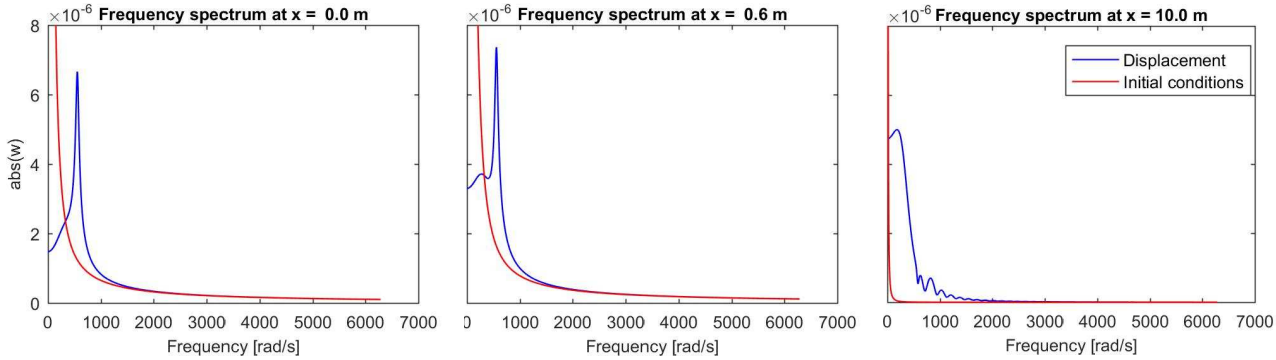

Figure 4.8 – Displacement frequency spectra for the second step of the mixed time-frequency analysis, at the first and last nodes, as well as at the position of the load (middle), for the system with trivial input initial state, compared to the initial state in the high-frequency regime

To improve the decay of the spectra, the initial displacement in the high-frequency regime, eq. (4.28), is subtracted from the frequency spectra and the inverse Laplace transform is performed separately:

$$w_{2,i}\left(x_i,t_2\right)=L^{-1}\left\{\hat{w}_{2,i}^{imp}\right\}+L^{-1}\left\{\frac{w_{2,i}\left(x_i,t_2=0\right)}{s}\right\}, \tag{4.29}$$

where $\hat{w}_{2,i}^{imp}=\hat{w}_{2,i}-\frac{w_{2,i}\left(x_i,t_2=0\right)}{s}$. The improvement, in terms of decay, of subtracting (4.28) from the original frequency spectra can be observed in Figure 4.9.

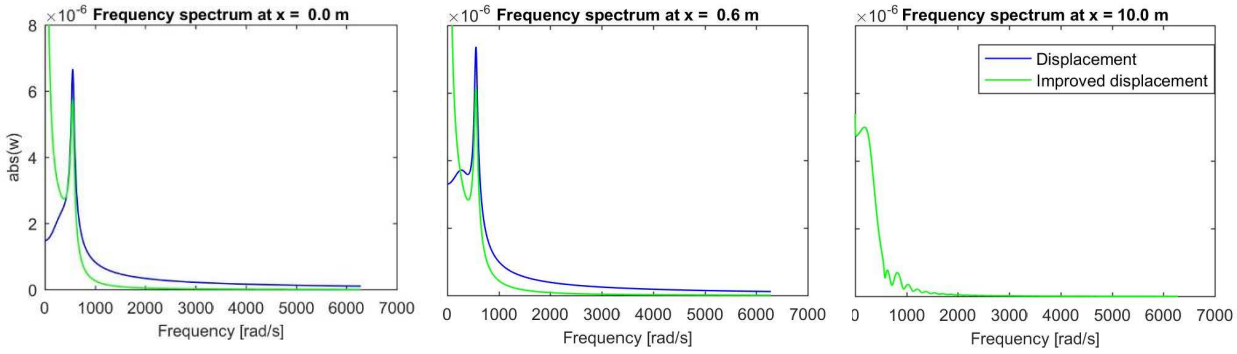

Figure 4.9 – Displacement frequency spectra for the second step of the mixed time-frequency analysis, at the first and last nodes, as well as at the position of the load (middle), for the system with trivial input initial state, compared to the improved frequency spectrum

The inverse Laplace transform of high-frequency approximation can be performed analytically, therefore (4.29) becomes:

$$w_{2,i}\left(x_i,t_2\right)=\frac{e^{\sigma t_2}}{\pi}\int_0^{\omega_{tr}}\mathrm{Re}\left\{\hat{w}_{2,i}^{imp}e^{i\omega t_2}\right\}d\omega+w_{2,i}\left(x_i,t_2=0\right)\ . \tag{4.30}$$

To obtain an even better decay of the frequency spectra of the displacement and also the velocity, where the latter is needed as initial velocity for the next system, at the next non-linear event occurrence, we also subtract the initial velocity and acceleration in the high-frequency regime. The final improved frequency spectra for the displacement, velocity and acceleration, read:

$$\hat{w}_{2,i}^{imp} = \hat{w}_{2,i} - \frac{w_{2,i}\left(x_i, t_2 = 0\right)}{s} - \frac{\dot{w}_{2,i}\left(x_i, t_2 = 0\right)}{s^2} - \frac{\ddot{w}_{2,i}\left(x_i, t_2 = 0\right)}{s^3},$$

$$\hat{v}_{2,i}^{imp} = \hat{v}_{2,i} - \frac{\dot{w}_{2,i}\left(x_i, t_2 = 0\right)}{s} - \frac{\ddot{w}_{2,i}\left(x_i, t_2 = 0\right)}{s^2},$$

$$\hat{a}_{2,i}^{imp} = \hat{a}_{2,i} - \frac{\ddot{w}_{2,i}\left(x_i, t_2 = 0\right)}{s}, \tag{4.31}$$

where $\dot{w}_{2,i}\left(x_i, t_2 = 0\right)$, $\ddot{w}_{2,i}\left(x_i, t_2 = 0\right)$ are the applied initial velocity and acceleration and $\hat{v}_{2,i}^{imp}$, $\hat{a}_{2,i}^{imp}$ represent the Laplace-domain velocity and acceleration, which read:

$$\hat{v}_{2,i} = s\hat{w}_{2,i} - w_{2,i}\left(x_i, t_2 = 0\right),\ \hat{a}_{2,i} = s^2\hat{w}_{2,i} - sw_{2,i}\left(x_i, t_2 = 0\right) - \dot{w}_{2,i}\left(x_i, t_2 = 0\right). \tag{4.32}$$

The final expressions of the time-domain displacement, velocity and acceleration are:

$$w_{2,i}\left(x_i, t_2\right) = \frac{e^{\sigma t_2}}{\pi}\int_0^{\omega_{tr}} \mathrm{Re}\left\{\hat{w}_{2,i}^{imp} e^{i\omega t_2}\right\} d\omega + w_{2,i}\left(x_i, t_2 = 0\right) + \dot{w}_{2,i}\left(x_i, t_2 = 0\right)t_2 + \ddot{w}_{2,i}\left(x_i, t_2 = 0\right)\frac{t_2^2}{2},$$

$$v_{2,i}\left(x_i, t_2\right) = \frac{e^{\sigma t_2}}{\pi}\int_0^{\omega_{tr}} \mathrm{Re}\left\{\hat{v}_{2,i}^{imp} e^{i\omega t_2}\right\} d\omega + \dot{w}_{2,i}\left(x_i, t_2 = 0\right) + \ddot{w}_{2,i}\left(x_i, t_2 = 0\right)t_2,$$

$$a_{2,i}\left(x_i, t_2\right) = \frac{e^{\sigma t_2}}{\pi}\int_0^{\omega_{tr}} \mathrm{Re}\left\{\hat{a}_{2,i}^{imp} e^{i\omega t_2}\right\} d\omega + \ddot{w}_{2,i}\left(x_i, t_2 = 0\right). \tag{4.33}$$

The subtraction of the initial displacement, velocity and acceleration in the high-frequency regime, introduces a very high peak close to zero frequency. This is due to the division by s, s^2 and s^3, which for zero frequency become σ, σ^2, σ^3, where σ usually is chosen to be a small value. This high peak is observed by zooming out the spectra in Figure 4.9, and can be visualized in Figure 4.10.

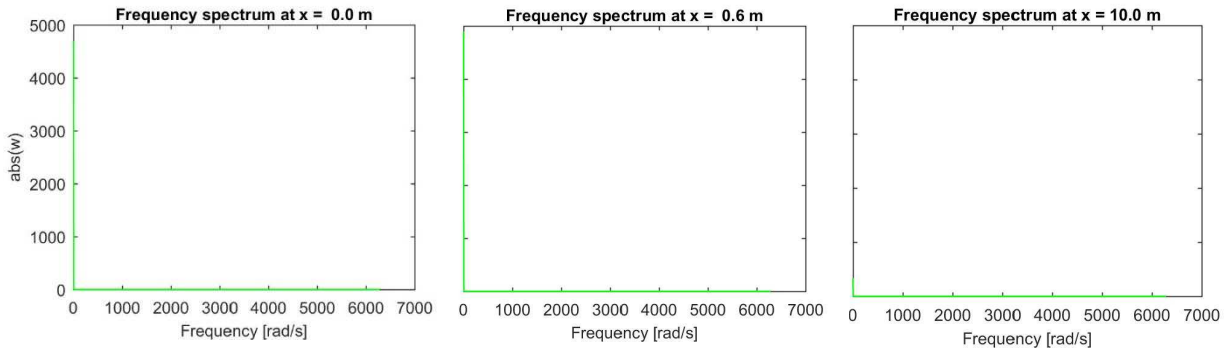

Figure 4.10 – Improved displacement frequency spectra for the second step of the mixed time-frequency analysis, at the first and last nodes, as well as at the position of the load (middle), for the system with trivial input initial state

In order to accurately integrate this high peak numerically, a very refined frequency sampling is needed close to zero frequency, which is very computationally expensive. To avoid refining the frequency sampling, the subtraction of the initial conditions in the high-frequency regime is divided in two components. For small frequencies, the original frequency spectrum is integrated numerically, while the integration of the high-frequency approximation to be subtracted, is performed analytically. For high frequencies, the improved spectrum is integrated numerically. This procedure can be better understood by the visual aid in Figure 4.11.

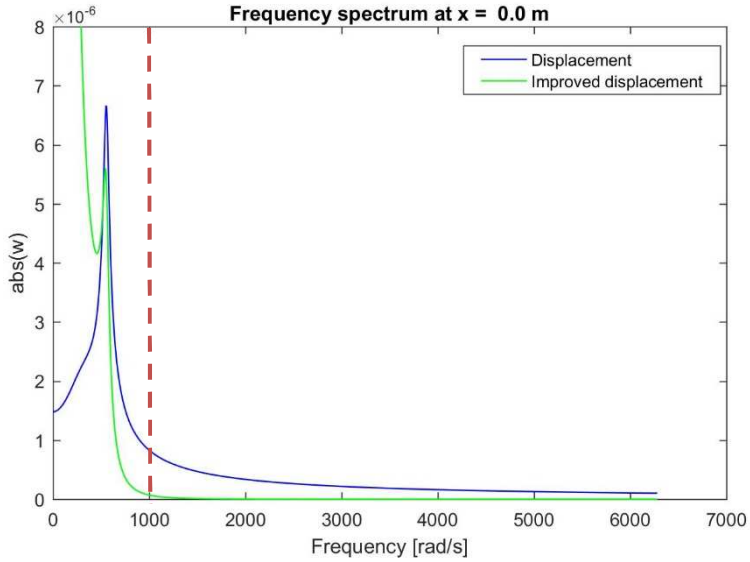

Figure 4.11 - Displacement frequency spectrum for the second step of the mixed time-frequency analysis, at the first node, for the system with trivial input initial state, compared to the improved displacement frequency spectrum

A certain frequency is chosen, ω_A, far away enough from zero frequency point such that the high peak has vanished. For the frequencies smaller than the chosen frequency ω_A, the numerical integration in (4.33) is performed based on the original frequency spectra, while the inverse Laplace transform is performed analytically for the subtracted high-frequency approximation, as follows:

$$w_{2,i}^{A}\left(x_i,t_2\right)=\frac{e^{\sigma t_2}}{\pi}\int_0^{\omega_A}\mathrm{Re}\left\{\hat{w}_{2,i}e^{i\omega t}\right\}d\omega-w_{2,i}\left(x_i,t_2=0\right)I_1-\dot{w}_{2,i}\left(x_i,t_2=0\right)I_2-\ddot{w}_{2,i}\left(x_i,t_2=0\right)I_3,$$

$$v_{2,i}^{A}\left(x_i,t_2\right)=\frac{e^{\sigma t_2}}{\pi}\int_0^{\omega_A}\mathrm{Re}\left\{\hat{v}_{2,i}e^{i\omega t}\right\}d\omega-\dot{w}_{2,i}\left(x_i,t_2=0\right)I_1-\ddot{w}_{2,i}\left(x_i,t_2=0\right)I_2,$$

$$a_{2,i}^{A}\left(x_i,t_2\right)=\frac{e^{\sigma t_2}}{\pi}\int_0^{\omega_A}\mathrm{Re}\left\{\hat{a}_{2,i}e^{i\omega t}\right\}d\omega-\ddot{w}_{2,i}\left(x_i,t_2=0\right)I_1, \qquad (4.34)$$

where $w_{2,i}^{A}$, $v_{2,i}^{A}$, $a_{2,i}^{A}$ represent the time-domain displacement, velocity and acceleration of the Laplace-domain images integrated up to ω_A and I_1, I_2, I_3 are:

$$I_1=\frac{e^{\sigma t_2}}{\pi}\int_0^{\omega_A}\mathrm{Re}\left\{\frac{e^{i\omega t}}{\sigma+i\omega}\right\}d\omega,$$

$$I_2 = \frac{e^{\sigma t_2}}{\pi}\int_0^{\omega_A} \mathrm{Re}\left\{\frac{e^{i\omega t}}{(\sigma+i\omega)^2}\right\}d\omega,$$

$$I_3 = \frac{e^{\sigma t_2}}{\pi}\int_0^{\omega_A} \mathrm{Re}\left\{\frac{e^{i\omega t}}{(\sigma+i\omega)^3}\right\}d\omega. \qquad (4.35)$$

These integrals can be performed analytically. Their expressions are not presented here for brevity, but close-form expressions of the integrals can be obtained by using Maple or similar mathematical software.

For the frequencies larger than the chosen frequency ω_a, the numerical integration in (4.33) is performed based on the improved frequency spectra, as follows:

$$w_{2,i}^B(x_i,t_2) = \frac{e^{\sigma t_2}}{\pi}\int_{\omega_A}^{\omega_{tr}} \mathrm{Re}\left\{\hat{w}_{2,i}^{imp} e^{i\omega t}\right\}d\omega, \quad v_{2,i}^B(x_i,t_2) = \frac{e^{\sigma t_2}}{\pi}\int_{\omega_A}^{\omega_{tr}} \mathrm{Re}\left\{\hat{v}_{2,i}^{imp} e^{i\omega t}\right\}d\omega,$$

$$a_{2,i}^B(x_i,t_2) = \frac{e^{\sigma t_2}}{\pi}\int_{\omega_A}^{\omega_{tr}} \mathrm{Re}\left\{\hat{a}_{2,i}^{imp} e^{i\omega t}\right\}d\omega, \qquad (4.36)$$

where $w_{2,i}^B$, $v_{2,i}^B$, $a_{2,i}^B$ represent the time-domain displacement, velocity and acceleration of the Laplace-domain images integrated from ω_A to the truncated frequency. The final time-domain expressions become:

$$w_{2,i}(x_i,t_2) = w_{2,i}^A + w_{2,i}^B + w_{2,i}(x_i,t_2=0) + \dot{w}_{2,i}(x_i,t_2=0)t_2 + \ddot{w}_{2,i}(x_i,t_2=0)\frac{t_2^2}{2},$$

$$v_{2,i}(x_i,t_2) = v_{2,i}^A + v_{2,i}^B + \dot{w}_{2,i}(x_i,t_2=0) + \ddot{w}_{2,i}(x_i,t_2=0)t_2,$$

$$a_{2,i}(x_i,t_2) = a_{2,i}^A + a_{2,i}^B + \ddot{w}_{2,i}(x_i,t_2=0). \qquad (4.37)$$

With (4.37), the decay of the frequency spectra has been significantly improved. Next, a higher order finite difference approximation of the fourth-order derivative is derived to improve the solution even further.

4.3.2. Higher order finite difference approximation

In section 3.3, the fourth-order derivative in the equation of motion has been approximated using a central difference approach using five nodes, the point where the behaviour is approximated is taken, and two nodes at each of its side. This approximation has a second-order accuracy. To improve the accuracy, the central difference for nine nodes is derived in this section. The improvement is graphically represented for the frequency spectrum of the system analyzed in the previous section.

The polynomial in (3.49) for the approximation with nine nodes reads:

$$p = a_1 w(x_0 - 4l) + a_2 w(x_0 - 3l) + a_3 w(x_0 - 2l) + a_4 w(x_0 - l) + a_5 w(x_0)$$

$$+a_6 w(x_0+l)+a_7 w(x_0+2l)+a_8 w(x_0+3l)+a_9 w(x_0+4l), \tag{4.38}$$

where $a_1, a_2, a_3, a_4, a_5, a_6, a_7, a_8, a_9$ are the unknown weighing factors and l is the dimension of the discretization. Polynomial p is rearranged, grouping the same order-derivatives together, thus obtaining:

$$p = f_1 w(x_0)+f_2 w'(x_0)+f_3 w''(x_0)+f_4 w'''(x_0)+f_5 w''''(x_0)+f_6 w'''''(x_0)$$
$$+f_7 w''''''(x_0)+f_8 w'''''''(x_0)+f_9 w''''''''(x_0), \tag{4.39}$$

where $f_1, f_2, f_3, f_4, f_5, f_6, f_7, f_8, f_9$ are functions of the unknown weighing factors. Because the fourth-order derivative is sought for, we impose functions $f_1 = f_2 = f_3 = f_4 = f_6 = f_7 = f_8 = f_9 = 0$ and $f_5 = 1$, consequently polynomial p becomes the fourth-order derivative:

$$p = w''''(x_0). \tag{4.40}$$

The system of nine algebraic equations is solved for the five unknown weighing factors, thus obtaining:

$$a_1 = a_9 = \frac{7}{240}, a_2 = a_8 = -\frac{2}{5}, a_3 = a_7 = \frac{169}{60}, a_4 = a_6 = -\frac{122}{15}, a_5 = \frac{91}{8}. \tag{4.41}$$

Replacing the determined weighing coefficients in (4.38), the approximation of the fourth-order derivative using central difference approach of 6th order accuracy has been obtained. It is important to remark here, that the central difference approximation with nine nodes cannot be used at the boundaries because there are only two boundary conditions with which four ghost nodes would have to be solved. Consequently, at the boundaries we either use the five-nodes approximation, or derive a hybrid between central and forward difference approximation, such that only we only have two ghost nodes.

To visualize the improvement obtained by using a higher-order central difference approximation, relative errors of the displacement frequency spectrum are computed. The frequency spectrum is chosen to calculate the error between the two central difference approximations because the analytical solution of the system with trivial initial state, has been obtained in the Laplace-domain, in section 3.1. Therefore, the error introduced by performing the inverse Laplace transform numerically is not interfering with the results. The absolute relative error e is defined as:

$$e = \frac{\left|\hat{w}_{FD} - \hat{w}_{an}\right|}{\left|\hat{w}_{an}\right|}, \tag{4.42}$$

where $\hat{w}_{FD}$ is the Laplace-domain displacement of the numerical model computed using one of the finite difference approximations and $\hat{w}_{an}$ is the analytical Laplace-domain displacement derived in section 3.1, eq. (3.7). The results are presented in Figure 4.12 for three dimensions of the element size l.

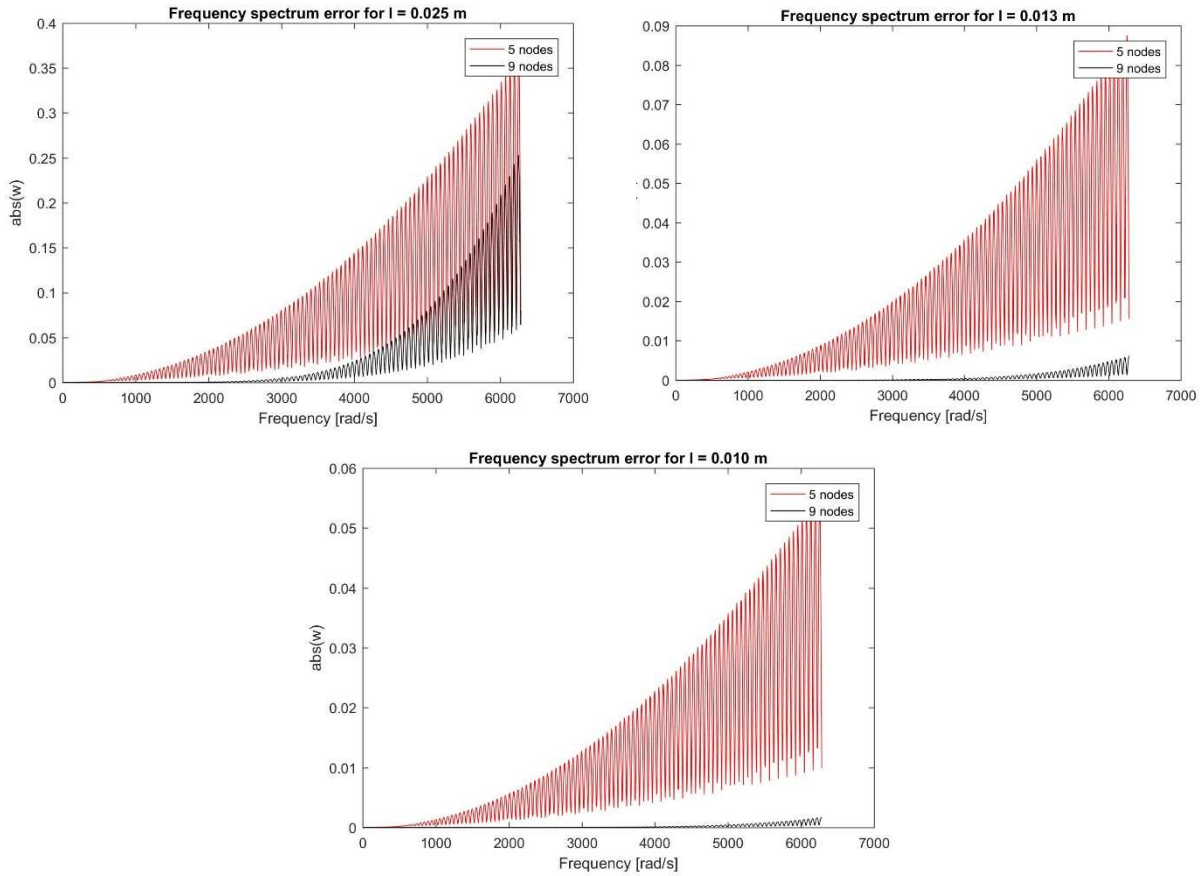

Figure 4.12 – Absolute relative error of the finite difference approximation with 5 and 9 nodes of the Laplace-domain displacement frequency spectrum for the system with trivial input initial state compared to the analytical solution

It is important to note that using a higher-order approximation does not necessarily imply that the error, for any element size l, will be smaller compared to using a lower-order approximation. The higher-order approximation means that the rate with which the solution converges to the exact solution is higher for higher-order approximations. As seen in Figure 4.12, the error reduces considerably by using a higher-order approximation.

With the improved decay of the frequency spectra discussed in section 4.3.1 and the higher-order finite difference approximation incorporated, the results are graphically represented in Figure 4.13. Once again, the mixed time-frequency solution is tested in the linear limit case, for the system with homogeneous stiffness and trivial input initial state.

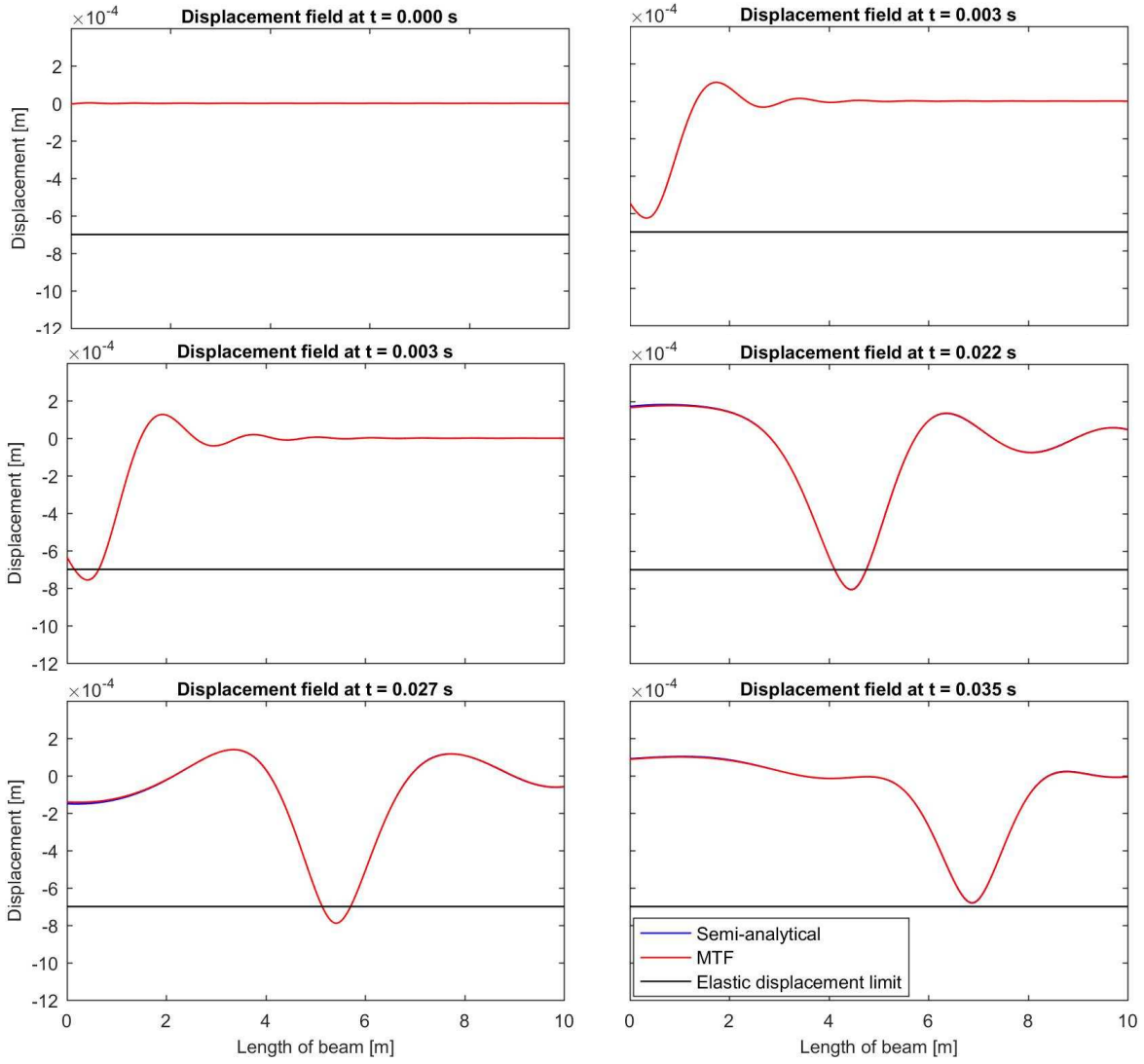

Figure 4.13 – Improved displacement field obtained by means of mixed time-frequency approach in the linear limit case of compared to the semi-analytical solution obtained in Chapter 3.1 for the system with trivial input initial state

From Figure 4.13, we can see that the solution obtained using the mixed time-frequency approach exhibits the same behaviour as the semi-analytical solution. The error has reduced considerably and can be considered negligible.

In this section, several improvements have been made to the solution obtained using the mixed time-frequency approach. Firstly, the decay in the Laplace-domain frequency spectra of the displacement and velocity have been improved by subtracting the high-frequency approximation. The steep peak introduced by the subtraction of initial state has been overcome by dividing the frequency spectra in two parts; the original Laplace-domain expressions are numerically integrated left of frequency ω_A, while the improved Laplace-domain expressions are numerically integrated right of frequency ω_A. Moreover, a higher-order approximation for the finite difference operator has been introduced. Considering these improvements, the resulting solution exhibits a negligible error when compared to

the benchmark solution. In the next section, the system with inhomogeneous and non-linear Winkler stiffness and tuned input initial state is addressed.

4.4. Finite system with inhomogeneous, non-linear Winkler foundation and tuned initial state

In the previous sections, the system with trivial initial state has been studied in order to validate the mixed time-frequency approach for strong non-linear behaviour. Although it represents a good validation for the mixed time-frequency method, it is not the system aimed at being studied. The system to be studied is the one with input initial state based on the eigenfield, referred to as the tuned initial state. In this section, the changes to the solution derived in the previous sections due to a non-trivial input initial state are discussed. Finally, the solution is validated for the linear limit case against the numerical solution derived in section 3.3.

In this thesis, the non-linear behaviour of the Winkler stiffness is local, meaning that non-linear events occur due to the transition in stiffness and do not occur in the case of homogeneous Winkler stiffness. This implies that the eigenfield is in the linear regime. Consequently, the system is in the linear regime for the first step of the mixed-time frequency analysis. Of course, this is an assumption, based on the reasoning that we do not expect significant non-linear behaviour of the railway track in the homogeneous parts of the track. Despite this, the model derived in section 4.2 with the improvements from section 4.3 could account for a non-linear input initial state, but this is beyond the scope of this thesis.

Considering that the system is in the linear regime at global $t=0$, the Laplace-domain equation of motion for the system with tuned input initial state reads:

$$\left[K_{i,j}+4\gamma^2 s^2 I_{i,j}+4\beta_{A,i}^4 I_{i,j}\right]\hat{w}_{2,j}=-\frac{F_0}{vEI}e^{-s\left(\frac{x_i}{v}\right)}+F_{IC,i}+F_{b,i}, \tag{4.43}$$

where $F_{IC,i}$ represents the input initial state and reads:

$$F_{IC,i}=4\gamma^2\left[sw\left(x_i,0\right)+\dot{w}\left(x_i,0\right)\right], \tag{4.44}$$

where $w\left(x_i,0\right),\dot{w}\left(x_i,0\right)$ are the input initial displacement and velocity based on the eigenfield, respectively; their magnitudes are found using eq. (3.9). The vector of boundary forces $F_{b,i}$ has exactly the same expression as in section 3.3, eq. (3.57) and (3.58). At this point, all quantities in (4.43) are known and the Laplace-domain displacement can be obtained. The time-domain displacement, velocity and acceleration are obtained by applying the inverse Laplace transform numerically to the improved Laplace-domain displacement, velocity and acceleration expressions, according to the previous section.

Once the time-domain displacement is obtained, the first non-linear event is sought for. The second step of the mixed time-frequency analysis is the same as presented in section 4.2, also considering the improvements from section 4.3. The only change is the non-trivial input initial state, which has to be accounted for when deriving the state of the semi-infinite domain to the left of the computational domain, eq. (4.14). The non-trivial input initial state is accounted for through the particular solution

$\hat{w}_{L,in,p}$, which was set to zero for the analysis performed in section 4.2 and in the current analysis the expression for $\hat{w}_{L,in,p}$ is given by (3.13) (only for $x < 0$).

Considering the changes discussed in section 4.3, the solution of the system with tuned initial state using the mixed time-frequency approach can be obtained. In Figure 4.14, a validation of this solution for the linear limit case is graphically represented. The parameters for the system and the Winkler stiffness profile are the same as in *case 1* presented in section 3.4. Note that w_e has been chosen to equal the maximum displacement in the eigenfield.

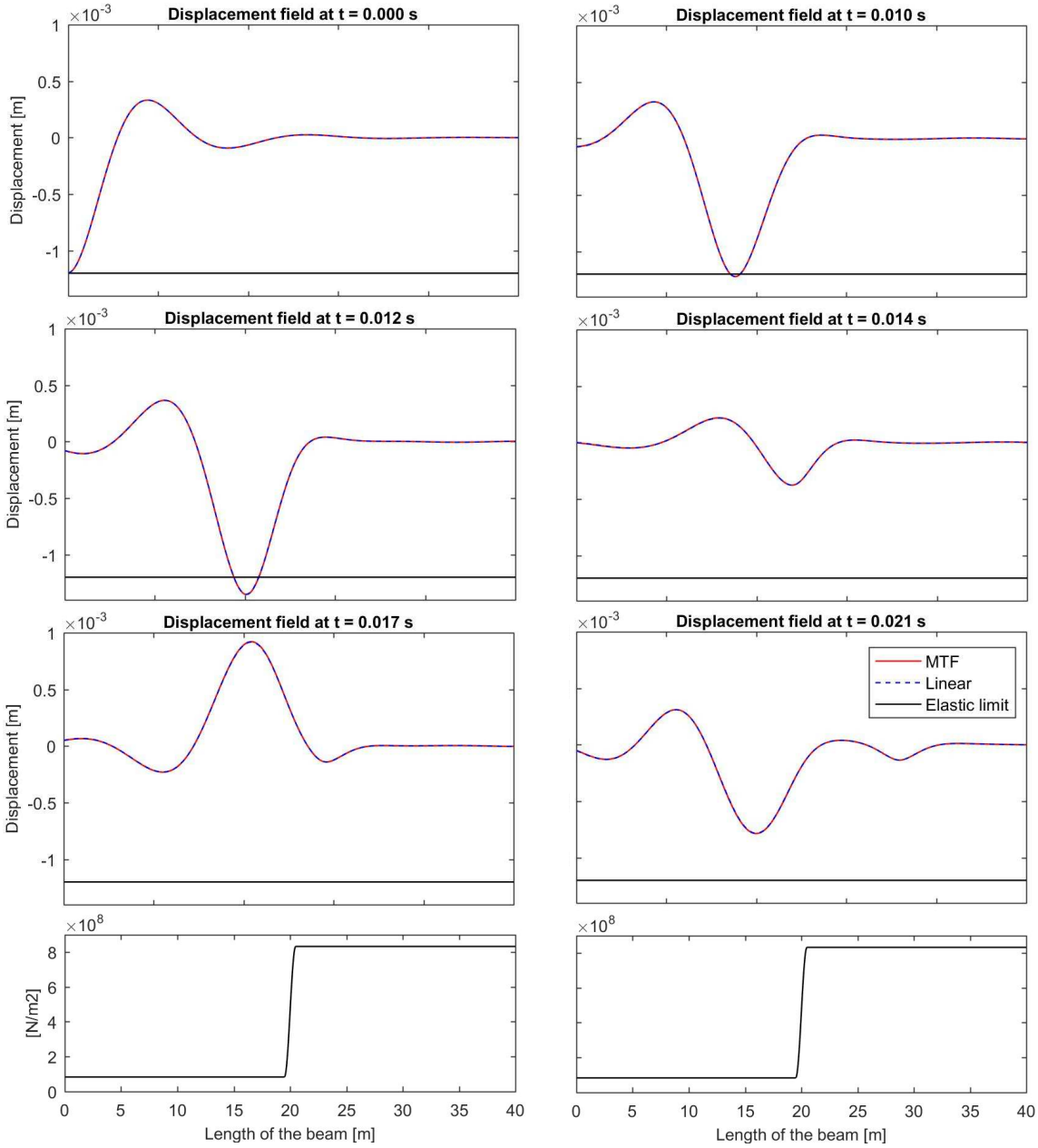

Figure 4.14 - Displacement field obtained by means of the mixed time-frequency approach compared in the limit case k_A=k_B with the solution derived in Chapter 3

In Figure 4.14, we can see that the solution obtained by means of the time-frequency approach for the linear limit case, exhibits the same behaviour as the numerical solution computed in section 3.4. Therefore, we conclude that the mixed time-frequency method has been validated. In the next section, graphical results for the true non-linear behaviour, where $k_A \neq k_B$, are presented and discussed.

4.5. Graphical results and concluding remarks of the chapter

In the previous section, the system with tuned input initial state solved by means of the mixed time-frequency method has been validated in the linear limit case. In this section, the said system's response is graphically represented for true non-linear behaviour. The non-linear behaviour of the Winkler stiffness is visualized in Figure 4.15. The linear part is described by stiffness k_A, while in the plastic regime and in loading by k_B and in unloading/reloading again by k_A.

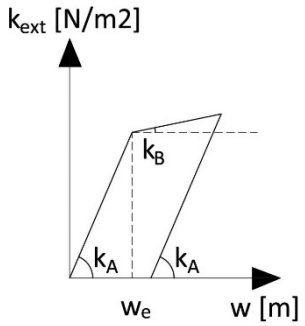

Figure 4.15 - Winkler stiffness non-linear behaviour

To analyze the influence of the non-linear behaviour in Winkler stiffness, four cases are analyzed, where the length of the transition zone and the velocity of the load is varied, as follows:

- *Case 1*: $l_{t,1} = 1$ m, $v_1 = 350$ m/s,
- *Case 2*: $l_{t,2} = 5$ m, $v_2 = 350$ m/s,
- *Case 3*: $l_{t,3} = 1$ m, $v_3 = 400$ m/s,
- *Case4*: $l_{t,4} = 5$ m, $v_4 = 400$ m/s.

The load velocity of $v = 350$ m/s represents 85% of the minimum phase velocity of the waves in the system, while $v = 400$ m/s represents 95%. The expression used for the Winkler stiffness profile in the linear regime is defined as in section 3.4. The parameters of the Winkler stiffness in the non-linear regime are chosen to be twenty times less than the ones in the linear regime. The following parameters are used for the graphical results:

- Winkler stiffness in the soft part: $k_{A1} = 8.33\times10^7$, $k_{B1} = 4.17\times10^6$ N/m^2,
- Winkler stiffness in the stiff part: $k_{A2} = 8.33\times10^8$, $k_{B2} = 4.17\times10^7$ N/m^2,
- Distributed beam and sleepers mass: $m = 268$ kg/m,
- Beam bending stiffness: $EI = 6.42\times10^6$ N/m^2,
- Constant load amplitude: $F_0 = 8\times10^4$ N.

The elastic displacement limit is chosen to represent the worst-case scenario, when the steady-state eigenfield maxima is almost reaching the elastic displacement limit. Because the eigenfield changes depending on velocity, the two elastic displacement limits, depending on velocity, are:

- $w_{e,350} = 1.2\times10^{-3}$ m,
- $w_{e,400} = 2.4\times10^{-3}$ m.

It must be mentioned that the length of the system in the first two cases is 10 m, while for the third and fourth the length is chosen to be 20 m. This is because the eigenfield in the case of load velocity 95% of the wave speed, is broader and would otherwise interfere with the transition zone at $t = 0$.

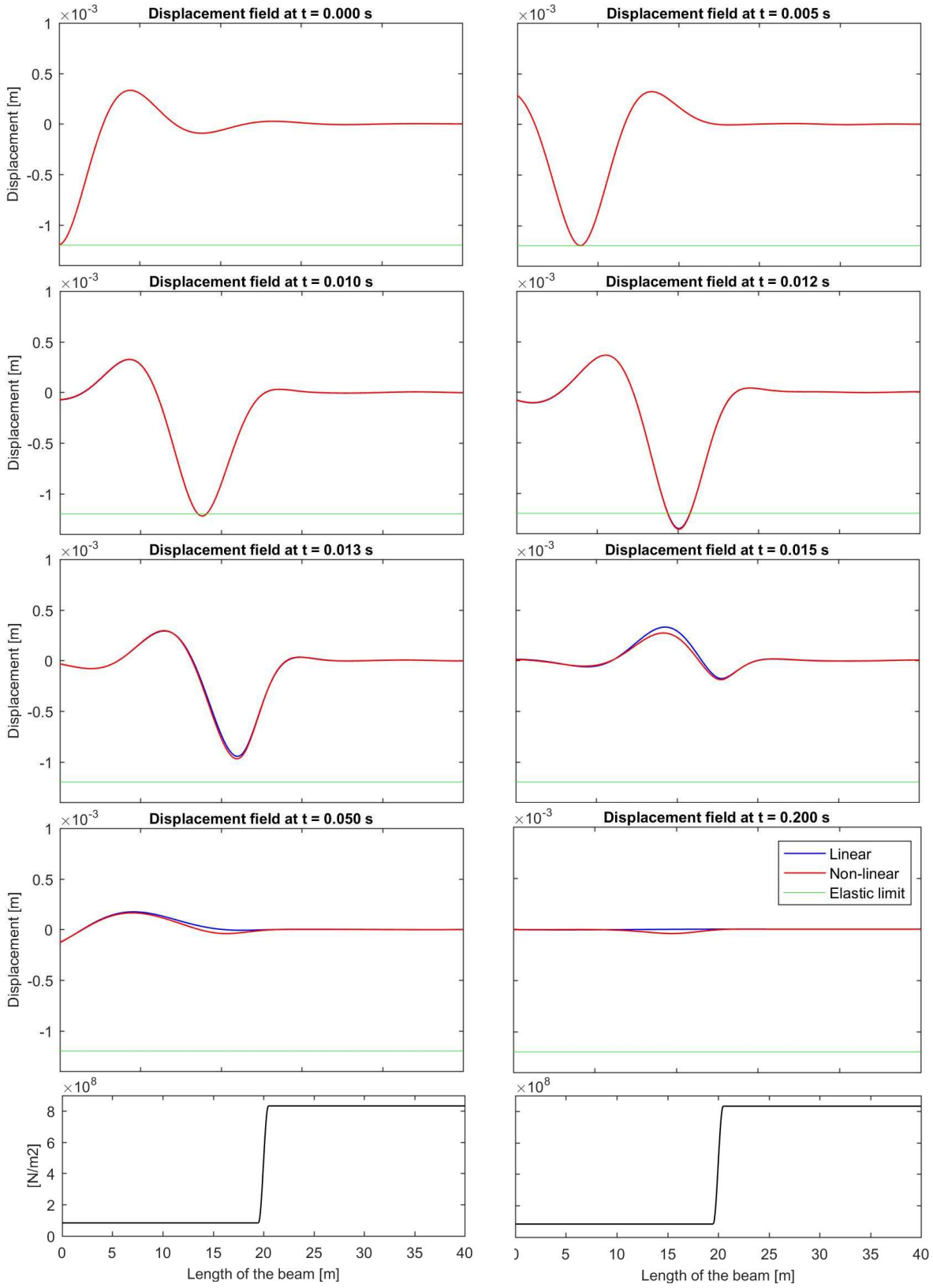

Figure 4.16 - Displacement field of the system with inhomogeneous and non-linear Winkler stiffness compared to the solution of the same system, but with linear Winkler stiffness, for Case 1

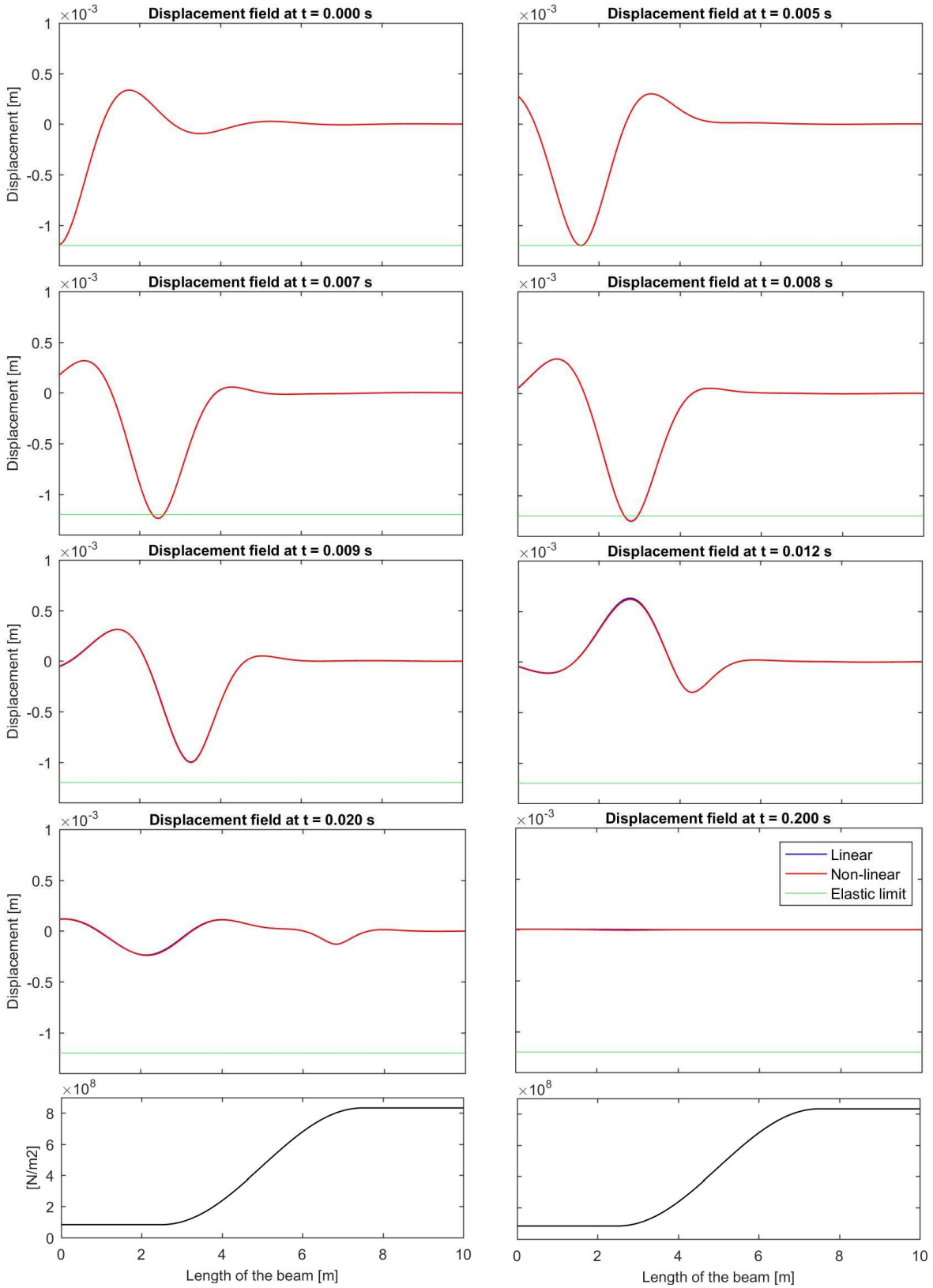

Figure 4.17 - Displacement field of the system with inhomogeneous and non-linear Winkler stiffness compared to the solution of the same system, but with linear Winkler stiffness, for Case 2

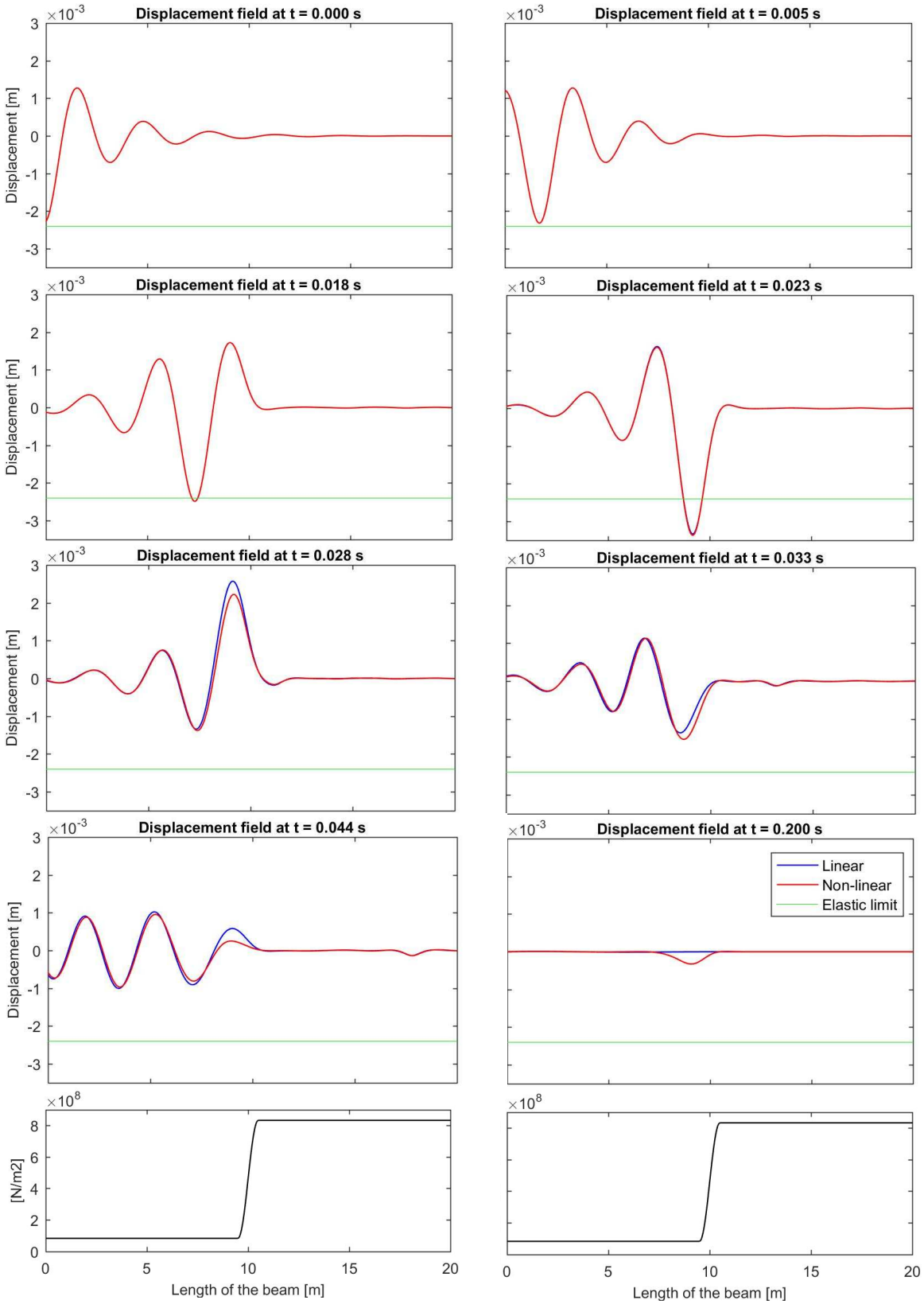

Figure 4.18 - Displacement field of the system with inhomogeneous and non-linear Winkler stiffness compared to the solution of the same system, but with linear Winkler stiffness, for Case 3

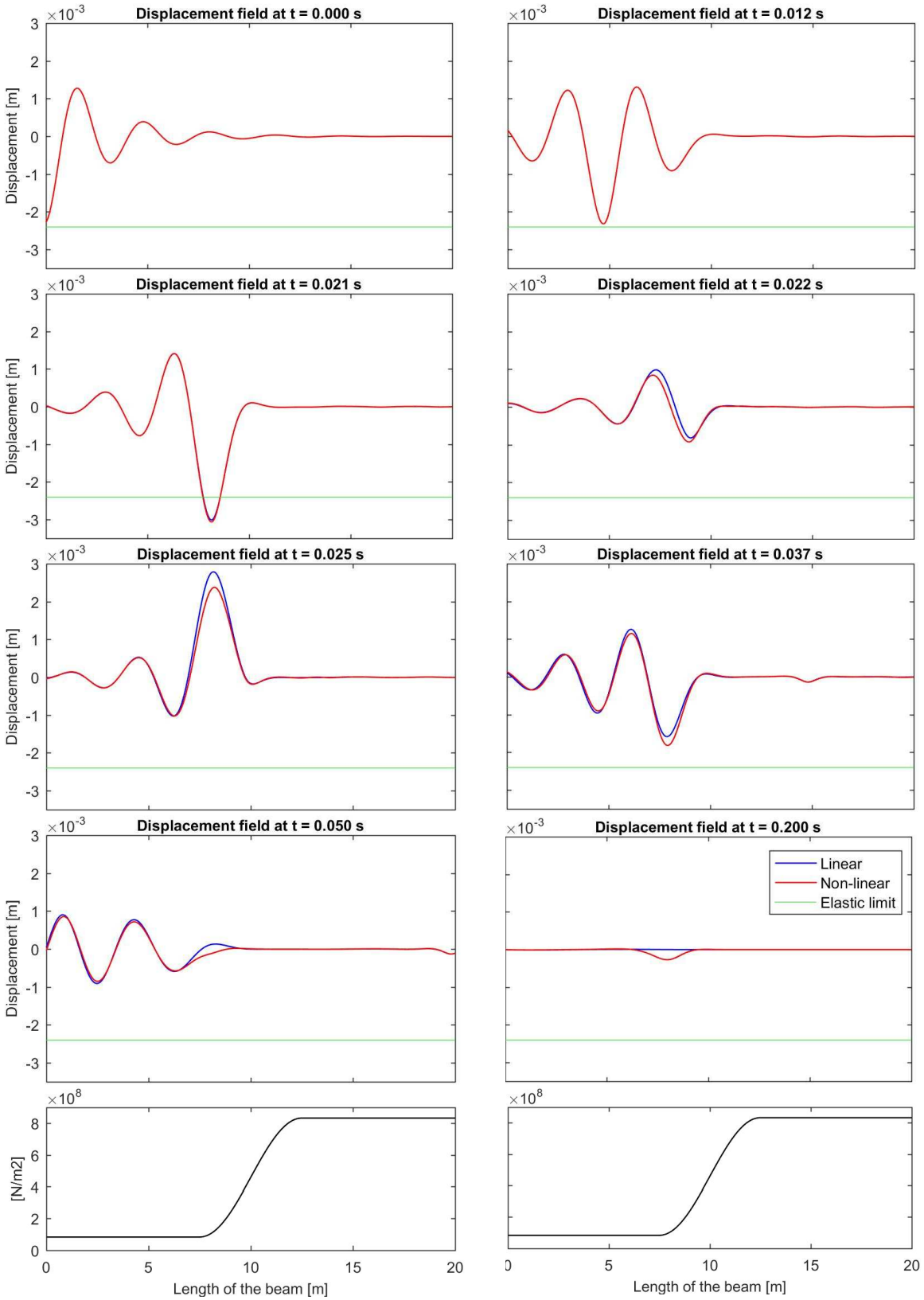

Figure 4.19 - Displacement field of the system with inhomogeneous and non-linear Winkler stiffness compared to the solution of the same system, but with linear Winkler stiffness, for Case 4

In *case 1*, depicted in Figure 4.16, the non-linear system exhibits a significant plastic deformation in front of the transition zone. The free waves propagating backwards from the transition zone constructively interfere with the eigenfield, leading to an amplification of its maxima which exceeds the elastic deformation limit.

In *case 2*, depicted in Figure 4.17, the plastic deformation exhibited by the non-linear system is diminished significantly when compared to *case 1*. This could be explained by the reduced amplitude of the reflected free waves propagating backwards from the transition zone. Although there is constructive interference, this does not lead to a significant amplification of the displacements.

In *case 3*, depicted in Figure 4.18, there is a large plastic deformation exhibited by the non-linear system. Due to the larger velocity, the eigenfield is broader. Consequently, the eigenfield interacts with the transition zone earlier in time, such that the free waves have developed more by the time the load has reached the transition zone. This leads to a stronger amplification of the displacements.

In *case 4*, depicted in Figure 4.19, there is also a large plastic deformation exhibited by the non-linear system. Although the length of the transition zone has been enlarged, the plastic deformation did not diminish significantly compared to *case 3.* It appears that in the case of the velocity of the load approaching the wave velocity, the smooth transition zone is not completely effective.

One important note is that the plastic deformation exhibited by the system should only be present in the Winkler stiffness, since the beam is not assumed to have a non-linear behaviour. Despite this, in the graphical results, the beam appears to exhibit plastic deformation. This is caused by the assumption that the two components, the beam and the Winkler stiffness are always in contact. Therefore, once the Winkler foundation exhibits plastic (i.e. permanent) deformation, it pulls the beam downward. Consequently, the plastic deformation exhibited in the graphical results is not the real plastic deformation of the foundation. This matter could be addressed by introducing another source of non-linearity, namely a loss of contact between the Winkler foundation and the beam, once the deflection of the beam is smaller, in absolute value, than the plastic deformation of the foundation.

In this chapter, the solution for the system of a finite beam resting on inhomogeneous and non-linear Winkler stiffness, subjected to a constant moving load, has been computed. To incorporate non-linear behaviour to the Winkler stiffness, the mixed time-frequency method has been used. The system is assumed to behave linearly in between non-linear events, therefore the solutions can be obtained using the Laplace transform method. The system is changed, and the time vector reset at every non-linear event occurrence. In order to obtain valid results, the frequency spectra decay has been improved as well as the finite difference approximation. This resulted in a solution which was successfully validated in the linear limit case against the semi-analytical solution derived in section 3.1. Finally, graphical results were presented in which the plastic deformation is clearly visible.

5. Conclusions

The first goal of this thesis was to obtain the solution for a system composed of an infinite beam resting on inhomogeneous Winkler foundation exhibiting a smooth transition in stiffness. With the obtained solution, the transition radiation and the influence of the length of the transition zone on it are analysed.

1) A finite length of the transition zone instead of an infinitesimal one (abrupt transition in stiffness) leads to a change in the magnitude of the response. As the transition length is increased, and consequently the stiffness profile becomes smoother, the free waves excited at the transition decrease in amplitude.
2) In addition to the amplitude change, also a shift in the phase of the excited free waves has been observed. The phase shift depends on the position of the smooth transition starting point relative to the abrupt transition point.
3) Moreover, for a very long transition zone, the overall behaviour of the excited free waves changes. The local vibrations at the transition zone have a shorter duration, leading to a significantly shorter radiated pulse, implying that the excited free waves are more localized in space.

The second goal of this thesis was to obtain the solution for a system composed of an infinite beam resting on inhomogeneous and non-linear Winkler foundation. The obtained solution was used to determine the possibility of plastic deformation introduced by the transition radiation and the parameters influencing it.

1) The plastic deformation in the transition zone is a consequence of a constructive interference of the excited free waves and the approaching eigenfield.
2) The length of the transition zone appears to have an influence on the exhibited plastic deformation. The plastic deformation reduces in magnitude as the transition length is increased. This is a direct consequence of the results obtained in relation to the first goal of the thesis. Increasing the length of the transition zone reduces the magnitude of the excited free waves, therefore leads to a less pronounced constructive interference between the excited free waves and the eigenfield, and thus to a decrease in magnitude of the plastic deformations.
3) Moreover, the plastic deformation is also influenced by the velocity of the load, relative to the wave velocity in the system. As the load velocity approaches the minimum wave velocity in the system, the eigenfield becomes not only larger in magnitude, but also broader. Consequently, the eigenfield in front of the load interacts with the transition zone earlier compared to a lower-velocity case, and the free waves develop more before the load itself reaches the transition zone. This leads to a more pronounced constructive interference, which in turn leads to larger plastic deformations.
4) Surprisingly, in the case of the load velocity close to the wave velocity in the system, enlarging the length of the transition zone does not lead to significant reduction in the plastic deformation exhibited.
5) The plastic deformation represented by the obtained solution is not a real plastic deformation in the Winkler foundation. A permanent contact between the beam and the Winkler foundation was assumed. The plastic deformation represented by the obtained solution is therefore a result of the interaction between the plasticly deformed foundation and the beam. True plastic behaviour in the Winkler foundation could be represented by the possibility of loss of contact between the beam and the foundation; this would occur if the absolute displacement of the beam

becomes smaller than the plastic deformation of the Winkler foundation. This represents a topic for further development of the derived solution.

Bibliography

[1] Wolfert A.R.M., 1999. *Wave effects in one-dimensional elastic systems interacting with moving loads.* Thesis TU-Delft, DUP Science, Delft

[2] K.N. van Dalen, 2006. *Transition radiation in two-dimensional inhomogeneous elastic systems.* Thesis TU-Delft

[3] Karel N. van Dalen, Andrei V. Metrikine, 2016. *Transition radiation in continua excited by a moving load.* XXIV ICTAM, 21-26 August 2016, Montreal, Canada

[4] Karel N. van Dalen, Apostolos Tsouvalas, Andrei V. Metrikine, Jeroen S. Hoving, 2015. *Transition radiation excited by a surface load that moves over the interface of two elastic layers.* International Journal of Solids and Structures 73–74 (2015) 99–112

[5] Jeroen S. Hoving, Andrei V. Metrikine, 2015. *A mixed time-frequency domain method to describe the dynamic behaviour of a discrete medium bounded by a linear continuum.* APM Proceedings

[6] A.V. Metrikine, A.C.W.M. Vrouwenvelder. *Dynamics of Structures* – CT4140 Lecture Notes. Delft University of Technology